

Enhanced Multicarrier Techniques for Professional Ad-Hoc and Cell-Based Communications (EMPhAtiC) Document Number D3.3 Reduction of PAPR and non linearities effects

Hmaied Shaiek, Daniel Roviras, S.S. Krishna Chaitanya Bulusu, Markku Renfors, Laurent Martinod, Milan Narandzic, Ljiljana Marijanovic, Stefan Tomic

▶ **To cite this version:**

Hmaied Shaiek, Daniel Roviras, S.S. Krishna Chaitanya Bulusu, Markku Renfors, Laurent Martinod, et al.. Enhanced Multicarrier Techniques for Professional Ad-Hoc and Cell-Based Communications (EMPhAtiC) Document Number D3.3 Reduction of PAPR and non linearities effects. [Research Report] European Commission Information Commission Technology. 2014. hal-02456390

HAL Id: hal-02456390
https://cnam.hal.science/hal-02456390

Submitted on 4 Feb 2020

HAL is a multi-disciplinary open access archive for the deposit and dissemination of scientific research documents, whether they are published or not. The documents may come from teaching and research institutions in France or abroad, or from public or private research centers.

L'archive ouverte pluridisciplinaire **HAL**, est destinée au dépôt et à la diffusion de documents scientifiques de niveau recherche, publiés ou non, émanant des établissements d'enseignement et de recherche français ou étrangers, des laboratoires publics ou privés.





Enhanced Multicarrier Techniques for Professional Ad-Hoc and Cell-Based Communications

(EMPhAtiC)

Document Number D3.3

Reduction of PAPR and non linearities effects

Contractual date of delivery to the CEC:	31/08/2014
Actual date of delivery to the CEC:	03/09/2014
Project Number and Acronym:	318362 EMPhAtiC
Editor:	CNAM
Authors:	Hmaied SHAIEK(CNAM), Daniel ROVIRAS (CNAM), Krishna BULUSU (CNAM), Markku RENFORS (TUT), Laurent MARTINOD (CASSIDIAN), Milan NARANDZIC (UNS), Ljiljana MARIJANOVIC (UNS), Stefan TOMIC (UNS).
Participants:	CNAM, CASSIDIAN ,TUT, UNS
Workpackage:	WP3
Security:	Public (PU)
Nature:	Report
Version:	2.0
Total Number of Pages:	110

Abstract:

Like other multicarrier modulation techniques, FBMC suffers from high peak-to-average power ratio (PAPR), impacting its performance in the presence of a nonlinear high power amplifier (HPA) in two ways. The first impact is an in-band distortion affecting the error rate performance of the link. The second impact is an out-of-band effect appearing as power spectral density (PSD) regrowth, making the coexistence between FBMC based broadband Professional Mobile Radio (PMR) systems with existing narrowband systems difficult to achieve. This report addresses first the theoretical analysis of in-band HPA distortions in terms of Bit Error Rate. Also, the out-of band impact of HPA nonlinearities is studied in terms of PSD regrowth prediction. Furthermore, the problem of PAPR reduction is addressed along with some HPA linearization techniques and nonlinearity compensation approaches.

Document Revision History

Version	Date	Author	Summary of main changes
0.1	26.05.2014	Daniel ROVIRAS (CNAM), Hmaied SHAIEK (CNAM), Krishna BULUSU (CNAM)	Initial structure of the document.
0.2	01.08.2014	Hmaied SHAIEK (CNAM), Daniel ROVIRAS (CNAM), Krishna BULUSU (CNAM), Markku RENFORS (TUT), Laurent MARTINOD (CASSIDIAN), Milan NARANDZIC (UNS)	First edition of the deliverable.
1.0	11.08.2014	Hmaied SHAIEK (CNAM), Daniel ROVIRAS (CNAM)	Updated version after changes suggested by Daniel ROVIRAS (CNAM). Version sent to WP3 partners for internal review.
1.1	27.08.2014	Hmaied SHAIEK (CNAM)	Updated version after internal review by WP3 partners.
2.0	01.09.2014	Hmaied SHAIEK (CNAM), Markku RENFORS (TUT)	Final version.

Table of contents

List of Figures **6**

List of Tables **9**

1 Introduction **10**
1.1 Motivation . . . 10
1.2 Objectives . . . 11

2 HPA models and characteristics **14**
2.1 Introduction . . . 14
2.2 Transmission scheme . . . 14
2.3 Memoryless HPA models . . . 16
2.3.1 Soft Envelope Limiter . . . 16
2.3.2 Rapp model . . . 16
2.3.3 Saleh model . . . 16
2.3.4 Polynomial model . . . 17
2.4 HPA models with memory . . . 18
2.5 Conclusion . . . 19

3 Impact of nonlinearities on in-band distortion **21**
3.1 Introduction . . . 21
3.2 System model . . . 21
3.2.1 OFDM and FBMC modulations in brief . . . 22
3.2.2 HPA model . . . 24
3.3 Nonlinear distortion modeling . . . 25
3.4 Analytical computation of $\boldsymbol{K}$ and $\boldsymbol{\sigma_d^2}$ . . . 26
3.4.1 Proposed method . . . 27
3.4.2 Analytical computation of $\boldsymbol{K}$ and $\boldsymbol{\sigma_d^2}$ using polynomial approximation . . . 27
3.5 Theoretical performance analysis . . . 30
3.5.1 Performance analysis in the case of an AWGN channel . . . 30
3.5.2 BER analysis in the case of a Rayleigh channel . . . 31
3.6 Simulation results . . . 32
3.6.1 BER analysis in the case of an AWGN channel . . . 32
3.6.2 BER analysis in the case of a Rayleigh channel . . . 33
3.7 Conclusion . . . 35

4 Impact of nonlinearities on out-of-band distortion **37**
4.1 Introduction . . . 37
4.2 Theoretical study for spectral regrowth using cumulants . . . 37
4.2.1 Introduction of cumulants . . . 37
4.2.2 Cumulants definition . . . 37
4.2.3 The cumulant/moment relation . . . 38
4.2.4 Cumulants and set-partitions . . . 38
4.2.5 Properties of cumulants . . . 40
4.2.6 Polynomial approximation of HPA Characteristics . . . 41
4.2.7 HPA modeling and spectral regrowth prediction . . . 42

4.2.8 Simulation results for PSD prediction . . . 43
4.3 Evaluation of uniform and non-uniform FBMC in presence of HPA nonlionearities 45
4.3.1 Evaluated uniform and non-uniform FLO and TLO multi-carrier waveforms 47
4.3.2 Spectral efficiency with HPA . . . 47
4.4 Conclusion . . . 51

5 PAPR reduction techniques 53
5.1 Introduction . . . 53
5.2 State of the art on PAPR reduction techniques . . . 53
5.2.1 Early applications . . . 53
5.2.2 Methods suggested for OFDM . . . 54
5.2.3 Different methods of PAPR reduction for OFDM . . . 54
5.2.4 Recent methods suggested for FBMC systems . . . 58
5.3 Overview of FBMC system . . . 58
5.3.1 FBMC signal structure . . . 58
5.3.2 Power profile of FBMC signals . . . 59
5.4 Comparison of the signal structures . . . 61
5.5 Overlapping SLM techniques for FBMC . . . 61
5.5.1 Classical SLM . . . 61
5.5.2 Dispersive SLM . . . 61
5.6 Trellis-based SLM . . . 66
5.6.1 Need for a Trellis-based method . . . 66
5.6.2 Description of the Trellis-based SLM algorithm . . . 67
5.6.3 Simulation results . . . 70
5.6.4 Impact of variation of T_o duration . . . 70
5.7 PAPR characteristics and reduction in FC-FB based transmitters . . . 71
5.7.1 PAPR characteristics of SC waveforms with very small roll-off . . . 72
5.7.2 Feasibility of PAPR reduction methods in FC-FB based transmitters . . . 73
5.8 Conclusion . . . 75

6 NL compensation and HPA linearization 77
6.1 State of the art of linearization techniques . . . 77
6.1.1 Linearization methods using modified HPA architectures . . . 77
6.1.2 Linearization methods using classical HPA architectures . . . 77
6.1.3 Predistortion of NL HPA . . . 78
6.1.4 Predistortion of NL HPA using a NL system . . . 79
6.2 Predistortion of FBMC signals using neural Networks . . . 80
6.2.1 Basis of neural network predistortion . . . 81
6.2.2 Neural network MLP predistortion for FBMC . . . 83
6.3 Linearized HPA performance limits . . . 86
6.4 Envelope tracking based HPA linearization . . . 86
6.4.1 Sensitivity to bandwidth limitations of DC-to-DC converter technology 90
6.4.2 Conclusion . . . 92
6.5 Measurements and performances on real HPA hardware . . . 92
6.5.1 Introduction . . . 92
6.5.2 Considered FMT scheme . . . 93
6.5.3 Waveform descriptions . . . 94
6.5.4 Test bench . . . 95

6.5.5 Theoretical spectrums 95
6.5.6 Measurements results 96

7 Conclusion **99**

8 References **101**

List of Figures

1-1 HPA nonlinear behavior. 10
1-2 Linearized HPA and input signal with low PAPR. 12

2-1 The transmission system model with NL HPA. 14
2-2 Linearized HPA and input signal with low PAPR. 15
2-3 AM/AM characteristics of Rapp HPA model. 17
2-4 AM/AM and AM/PM characteristics of Saleh HPA model. 18
2-5 Hammerstein model for a HPA with memory. 19
2-6 AM/AM and AM/PM characteristics of a HPA with memory. 20

3-1 The transmission system model with FBMC and OFDM modulations. 21
3-2 OFDM and FBMC symbol mapping on subcarriers. **(a)** OFDM and **(b)** FBMC. 23
3-3 BER vs $\boldsymbol{Eb/N0}$ for OFDM and FBMC system. SEL, $A_{sat} = 1$, 64 subcarriers, 16QAM, and AWGN channel. 33
3-4 BER vs $\boldsymbol{Eb/N0}$ for OFDM and FBMC system. Saleh HPA model, 64 subcarriers, 16QAM, $\varphi_0 = 0$, and AWGN channel. 34
3-5 BER vs $\boldsymbol{Eb/N0}$ for OFDM and FBMC system. Saleh HPA model, 64 subcarriers, 16QAM, $\varphi_0 = \pi/6$, and AWGN channel. 34
3-6 BER vs $\boldsymbol{Eb/N0}$ for OFDM and FBMC system. Saleh HPA model, 64 subcarriers, 16QAM, $\varphi_0 = \pi/3$, IBO $= 6$ dB, and Rayleigh channel. 35

4-1 Illustration of *additive partition* of 3. 40
4-2 AM/AM distortion - Saleh Model and its polynomial fitting of orders 3, 7 , 11 and 15. 43
4-3 AM/PM distortion - Saleh Model and its polynomial fitting of orders 3, 7 , 11 and 15. 44
4-4 PSD Prediction with IBO=1dB. 44
4-5 PSD Prediction with IBO=3dB. 45
4-6 PSD Prediction with IBO=1dB (3 different active Sub-bands). 46
4-7 FLO uniform arrangement spectra (a) and corresponding (low-pass) time-domain representations (b), FLO Nu-FBMC arrangement with symmetrical spectra (c) and corresponding (low-pass) time-domain representations (d) - all without oversamling. 48
4-8 FLO Nu-FBMC arrangement with asymmetrical spectra (a) and corresponding time-domain representations (b) - all without oversampling. 49
4-9 TLO uniform-FBMC arrangement (a) and his corresponding time-domain representation (b), TLO Nu-FBMC arrangement (c) and his corresponding time-domain representation (d), (without oversampling). 50
4-10 (a) Comparison of conventional OFDM, uniform FLO FBMC and uniform TLO FBMC, and (b) comparison of symmetrical Nu-FLO FBMC, asymmetrical Nu-FLO FBMC and Nu-TLO FBMC in context of HPA and mask fitting. 51
4-11 Comparison of conventional OFDM and uniform FLO FBMC for the maximum fitting of the PSD mask. 52

5-1 Impulse response for PHYDYAS and rectangular filters. 60
5-2 Illustration of mean-power overlapping among FBMC symbols. 60
5-3 Block diagram of DSLM for FBMC systems. 62

5-4 CCDF of PAPR plot for 10^5 FBMC symbols with PAPR calculated over $[0, T]$, $[T, 3T]$ and $[0, 4T]$ with $U = 4$ to illustrate the impact of variation of T_o duration on the DSLM scheme. . . . 64
5-5 CCDF of PAPR plot for 10^5 FBMC symbols with PAPR calculated over $[0, 4T]$ with $U = \{2, 4, 8\}$ to illustrate the impact of size of U on the DSLM scheme in comparison with SLM scheme for OFDM. . . . 65
5-6 CCDF of PAPR plot for 10^5 FBMC symbols with PAPR calculated over $[0, 4T]$ with $U = 4$ and $N = \{64, 128\}$ to illustrate the impact of FFT size on the DSLM scheme. . . . 65
5-7 Illustration of the trellis diagram between the two '*nodes*' where each '*node*' has U different '*states*'. . . . 68
5-8 Power Profile of two FBMC symbols in the duration of $[T, 4T]$ w.r.t the current symbol. . . . 69
5-9 CCDF of PAPR plot for 10^5 FBMC symbols with PAPR calculated over $[T, 4T)$ with $U = 2, 4, 8$ to illustrate the impact of size of U on the TSLM scheme in comparison with SLM scheme for OFDM. . . . 71
5-10 CCDF of PAPR plot for 10^5 FBMC symbols with PAPR calculated over $[T, 4T)$ with $U = 2, 4, 8$ to illustrate the comparison of the TSLM scheme with the earlier proposed DSLM scheme. . . . 71
5-11 CCDF of PAPR plot for 5000 FBMC symbols with PAPR calculated over different T_o with $U = 2$ to illustrate the impact of variation of T_o duration on the DSLM scheme. . . . 72
5-12 Example of an extended channel filter weight mask. . . . 73
5-13 PAPR characteristics of OFDM based and FB based SC-waveforms with different bandwidths and roll-off factors. Upper: QPSK modulation. Lower: 64QAM modulation. . . . 74
5-14 PAPR distribution with and without tone reservation in a FBMC case with 1.4 MHz LTE-like parameters for QPSK and 64QAM modulations. . . . 75

6-1 Principle of the predistorsion of a HPA. . . . 78
6-2 Ideal predistorsion result. . . . 79
6-3 Architecture of a predistortion working in baseband. . . . 80
6-4 Principle of a baseband predistorsion. . . . 80
6-5 Direct adaptation of the predistorsion function $g(.)$. . . . 81
6-6 Indirect adaptation of the predistorsion function $g(.)$. . . . 81
6-7 (a) Single Neuron, (b) Multi Layer Perceptron. . . . 82
6-8 Multi Layer Perceptron for predistorsion. . . . 83
6-9 Modified NN-MLP architecture for FBMC predistorsion. . . . 84
6-10 Performance of the first architecture based one a single NN-MLP. . . . 85
6-11 Performance of the second architecture based on two NN-MLPs for modulus and phase. . . . 85
6-12 Spectral regrowth for FB-SC waveform with QPSK and 64QAM modulations, different bandwidths and roll-off factors using Rapp (p=2.25) and SEL models for HPA. . . . 87
6-13 Spectral regrowth with 1.4 MHz LTE-like FBMC waveform with QPSK and 64QAM modulations and different back-off values using SEL HPA model with or without TR based PAPR mitigation. . . . 88

6-14 Spectral regrowth with 1.4 MHz LTE-like FBMC waveform with QPSK and 64QAM modulations and different back-off values using Rapp HPA model (p=2.25) with or without TR based PAPR mitigation. 89
6-15 The NL HPA model controlled by normalized signal envelope. 89
6-16 Performance comparison for HPA controlled by signal envelope: (a) CP-OFDM, uniform-FLO/TLO FBMC configurations, and (b) symmetrical Nu-FLO FBMC, asymmetrical Nu-FLO FBMC and Nu-TLO FBMC configurations for the maximum fitting of the PSD mask. 90
6-17 The NL HPA model controlled by filtered normalized signal envelope. 90
6-18 Transmit signal spectrum cutoff for uniform configuration (a), and non-uniform configuration (b) with oversampling factor 5:1. 91
6-19 Comparison of uniform FLO FBMC, TLO FBMC and CP-OFDM in context of HPA and mask fitting with transmit signal spectrum cutoff; a) $1/2$ spectrum cutoff, b) $1/4$ spectrum cutoff c) $1/8$ spectrum cutoff, with oversampling factor $= 5$. 91
6-20 Comparison of non-uniform FLO FBMC, TLO FBMC and CP-OFDM in context of HPA and mask fitting with transmit signal spectrum cutoff; a) $1/2$ spectrum cutoff, b) $1/4$ spectrum cutoff c) $1/8$ spectrum cutoff. 92
6-21 Theoretical PSDs of the three considered waveforms. OFDM in black, first FMT waveform in red and second FMT waveform in blue. 95
6-22 First waveform measured PSDs. At HPA base station output in blue and at $R\&S\ SMU200$ output in black. 96
6-23 Second waveform measured PSDs. At HPA base station output in blue and at $R\&S\ SMU200$ output in black. 97
6-24 Third waveform measured PSDs. At HPA base station output in blue and at $R\&S\ SMU200$ output in black. 98

List of Tables

3-1 Transmultiplexer impulse response 24
3-2 Comparison between estimated values of K and $\boldsymbol{\sigma_d^2}$ for both nonlinearly amplified OFDM and FBMC signals 26
3-3 Comparison between numerical and theoretical values of $\boldsymbol{K}$ and $\boldsymbol{\sigma_d^2}$ 29
3-4 Impact of the polynomial order approximation on the estimated values of K and $\boldsymbol{\sigma_d^2}$ 30

6-1 Specified parameters 94

1. Introduction

1.1 Motivation

Multicarriers systems are suffering from a major drawback related to their high Peak to Average Power Ratio (PAPR). The PAPR measures the variation of the instantaneous power compared to the mean power of the transmitted multicarrier signal. Low values of PAPR are synonymous with a transmitted signal with a power always very close to its mean power while high PAPR values indicate that the instantaneous power can be very high compared to the mean. Multicarrier signals exhibit a high PAPR because of the central limit theorem. In fact, the transmitted signal is a sum of independent signals (the different carriers) with same probability density function. When the number of subcarriers is sufficiently large (larger than few tens, for example), central limit theorem can be applied and the probability density function of real and imaginary parts of the multicarrier signal follows a Gaussian law giving high values of the PAPR.

The distribution of the transmitted power is not very important as far as linear systems are used in the transmission chain. Unfortunately, some elements of the chain are nonlinear (NL). In particular, the High Power Amplifier (HPA) has a NL behavior.

HPA at the emitter side can be quasi linear for a certain part of the input powers, P_{in}, (from 0 to P_1, see figure 1-1) and NL for input powers larger than P_1. Furthermore, the output power, P_{out}, of a HPA is limited to a saturation power P_{sat} (figure 1-1).

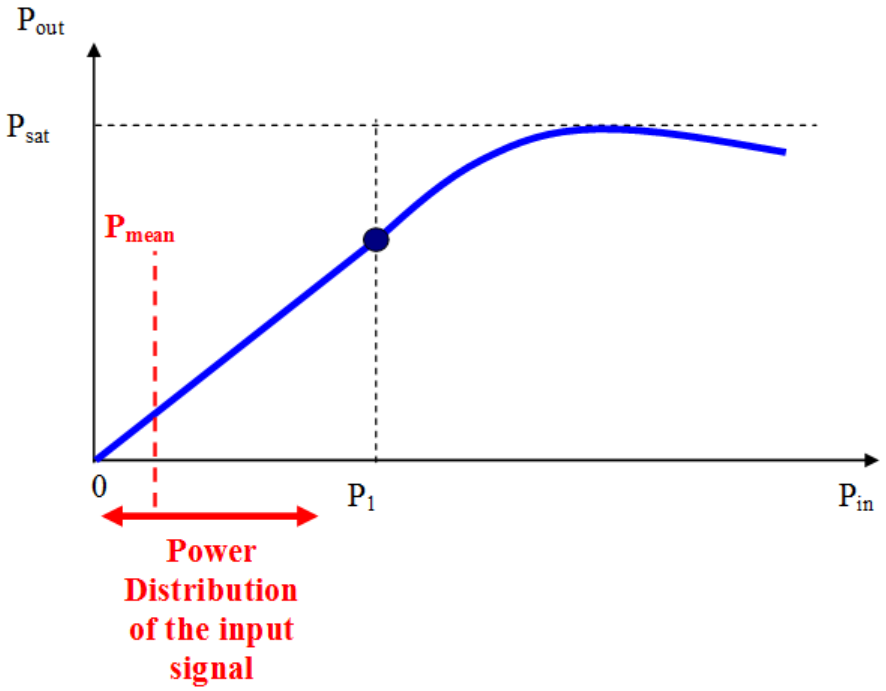


Figure 1-1: HPA nonlinear behavior.

If the input power is always lower than P_1, the HPA is operated in its quasi linear region and the high PAPR of the multicarrier signal will not have any influence on the quality of the transmission. This is illustrated in figure 1-1 by an input signal with a mean power equal to P_{mean} and a certain distribution of the input power around P_{mean}. Nevertheless, this situation has a high cost in terms of energy efficiency: operating a HPA with a very low mean input

power gives a low mean output power compared to P_{sat}. Especially for mobile applications with batteries it is thus necessary to increase the power efficiency. Real HPA communications systems will then be operated as close as possible to the saturation P_{sat} in order to increase the power efficiency. By doing that, two negative effects will appear:

- if the HPA is operated in its NL region, the output signal spectrum will be broadened compared to the input one,
- distortions will occur in the transmitted signal causing transmission errors.

Filter bank based multicarrier (FBMC[1]) systems have, like classical OFDM multicarrier signals, a high PAPR. For FBMC signals, spectral broadening is perhaps a more important drawback compared to OFDM. The later has a decreasing spectrum following the sinc function (sinus cardinal function) because of the rectangular shaping filter. On the contrary, FBMC signals exhibit a very strong decrease in the frequency domain due to their shaping filters. If NL HPA are used, the advantage of FBMC compared to OFDM related to the frequency localization can be highly diminished. It is thus of prime importance with FBMC to fight against NL amplification effects.

Concerning distortions induced by the NL HPA, it is also important to limit and correct them. Looking at figure 1-1, we can view several axes of progression concerning the NL effects of the HPA:

- we can increase the HPA linear area using HPA linearization. This is equivalent to increase P_1 towards P_{sat} (see illustration on figure 1-2),
- we can decrease the distribution of high values of the instantaneous power of the transmitted signal. This is equivalent to lowering the PAPR of the transmitted multicarrier signal (see illustration in figure 1-2),
- we can also correct NL distortion at the receiver side.

Increasing the HPA linearity together with PAPR minimization permits to increase power efficiency by increasing the mean power of the input signal, P_{mean}, very close to P_{sat}. If the HPA is perfectly linearized and if the PAPR is reduced to $0dB$ (instantaneous power always very close to P_{mean}), the power efficiency can be very close to one. Furthermore, if the input signal is always in the linear region of the HPA, the spectral regrowth will be limited.

1.2 Objectives

The objectives of D3.3 are the study of the impairments related to the NL HPA and various improvements for fighting against these NL distortions. Concerning the impairments we have in-band NL distortion together with out-of-band spectral regrowth.

1. In the first part of the document we will study the effect of NL HPA related to the in-band distortion. In this part we will investigate the performance of FBMC transmissions when a NL HPA is used. Theoretical and experimental results will be presented with very good agreement between theory and simulations.

[1]In this document, the acronym FBMC is generally used for the FBMC/OQAM waveform.

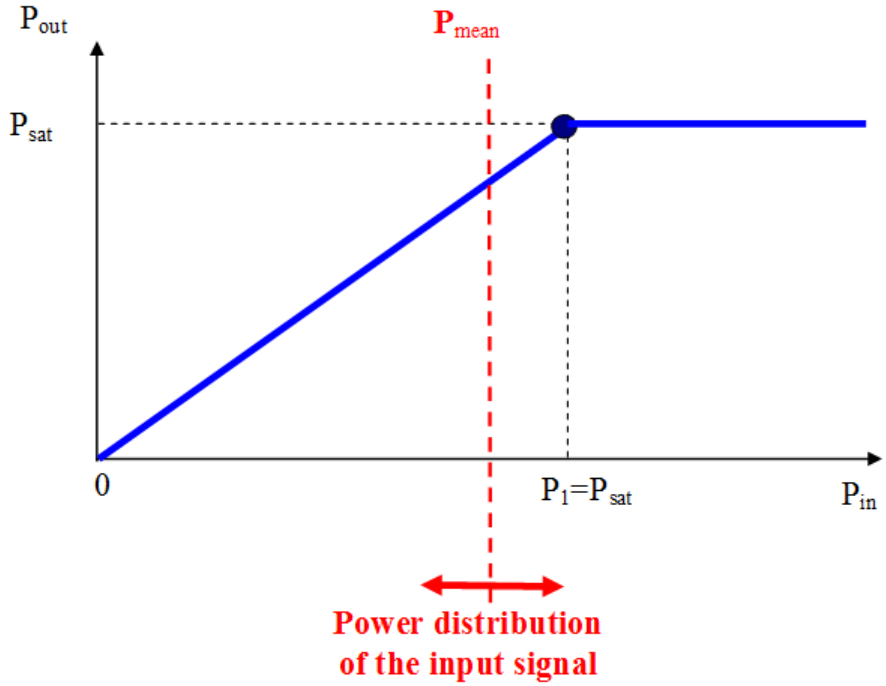


Figure 1-2: Linearized HPA and input signal with low PAPR.

2. In the second part of the document, the out-of-band spectral regrowth will be studied. A theoretical study using cumulants will be presented in order to compute theoretically spectral regrowth with NL HPA. The spectral regrowth will be also studied when using uniform and non-uniform carrier spacings with time-frequency dual waveforms and asymmetrical spectral shaping of FBMC subchannel signals.

   Concerning the improvements of the NL link we consider PAPR reduction techniques and transmitter or receiver corrections.

3. The third part of the document will talk about PAPR reduction methods for FBMC signals. These methods are inspired by PAPR reduction methods used for OFDM signals and adapted to the particular case of FBMC signals. The main difference between FBMC and OFDM lies in the fact that the FBMC filter impulse response is several symbol intervals, while in OFDM the length is just one symbol. Furthermore, as a low-PAPR alternative, the characteristics of filter bank based single-carrier (FB-SC) waveforms with small roll-off are also investigated, and compared with OFDM based SC-FDMA.

4. For transmitter correction we will mainly investigate HPA linearization. Two HPA linearization techniques are elaborated. The first technique is a predistortion based on neural network techniques. Here also, the specificity of FBMC must be taken into account for the predistorter architecture. The second linearization technique is based on envelope tracking. With this technique, the voltage saturation level (A_{sat}) of NL HPA model is controlled by normalized signal envelope.

The rest of the document is organized as follows. In chapter 2 we will present NL HPA together with classical HPA models. Chapter 3 will be devoted to in band distortions and associated performance in terms of BER while chapter 4 will present out-of-band spectral

regrowth studies. Chapter 5 presents PAPR reduction techniques for FBMC. In chapter 6, linearization of the HPA using predistorsion techniques is studied together with corrections of the NL impairments at the receiver side.

2. HPA models and characteristics

2.1 Introduction

In this chapter we will introduce the transmission scheme and describe the main characteristics of the HPA in terms of amplitude distortion, phase distortion and memory effects. Some HPA models, commonly used in the literature, will be also described.

2.2 Transmission scheme

Let's consider a multicarrier transceiver with NL HPA as shown in figure 2-1.

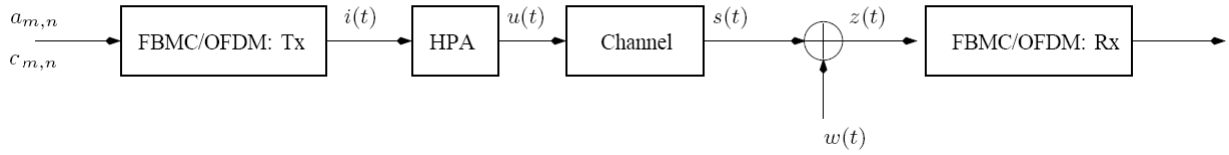


Figure 2-1: The transmission system model with NL HPA.

In figure 2-1, the M-array Quadrature Amplitude Modulated (MQAM) or Offset Quadrature Amplitude Modulated (OQAM) symbols ($a_{m,n}$ or $c_{m,n}$) are modulated by a Multi-Carrier Modulation (MCM) and amplified before transmission over a given channel. The NL HPA is commonly described by its input/output or transfer function characteristics. The amplitude to amplitude (AM/AM) and amplitude to phase (AM/PM) characteristics indicate the relationship between, respectively, the modulus and the phase variation of the output signal as functions of the modulus of the input signal.

The signal at the input of HPA has a complex envelope $i(t)$. This signal can be written as

$$i(t) = \rho(t)e^{j\varphi(t)} \tag{2.1}$$

where

- $\rho(t)$ is the input signal modulus, and
- $\varphi(t)$ is the input signal phase.

If the HPA is linear, the signal at its output can be written as

$$u(t) = Gi(t) \tag{2.2}$$

where $G = |G|e^{j\phi_0}$ is a complex scalar which is constant with respect to $\rho(t)$.

In practice the HPA cannot be considered as a linear device, i.e, $|G|$ and ϕ_0 constant with respect to $\rho(t)$. Then, as a general formulation, the amplified signal $u(t)$ can be written as

$$u(t) = F_a(\rho(t))\exp(jF_p(\rho(t)))\exp(j\varphi(t)) \tag{2.3}$$

where

- $F_a(\rho(t))$ is the AM/AM characteristic of the HPA,

- $F_p(\rho(t))$ is the AM/PM characteristic of the HPA.

We can rewrite equation 2.3 as following

$$u(t) = S(\rho(t)) \exp(j\varphi(t)) \tag{2.4}$$

where $S(\rho(t)) = F_a(\rho(t)) \exp(jF_p(\rho(t)))$ is the complex soft envelope of the amplified signal $u(t)$.

The AM/AM and AM/PM characteristics cause distortions on the constellation scheme and spectral regrowth, degrading then the system performance. In practice, in order to avoid or at least to reduce the effects of nonlinearities, the HPA is operated at a given Input Back-Off (IBO) from its $1dB$ compression point [1]. The $1dB$ compression point refers to the input power level where the transfer characteristics of the amplifier have dropped by $1\ dB$ from the ideal linear characteristics. An illustration of the $1dB$ compression point is given in figure 2-2.

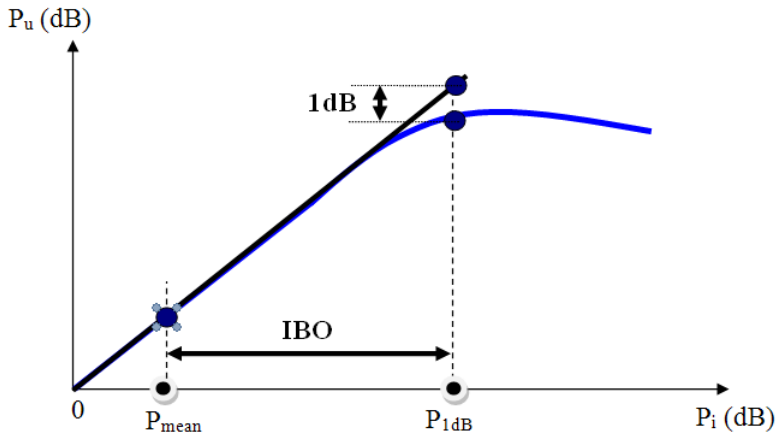


Figure 2-2: Linearized HPA and input signal with low PAPR.

In the log scale, the IBO is defined as follows:

$$\text{IBO} = 10 \log_{10} \left(\frac{P_{\text{1dB}}}{P_{mean}} \right) \tag{2.5}$$

where P_{1dB} is the input power at the $1dB$ compression point and P_{mean} is the mean input signal power.

Similarly we can define the Output Back-Off (OBO) as the ratio between the output power corresponding to $1dB$ compression point and the mean power at the output of the HPA.

$$\text{OBO} = 10 \log_{10} \left(\frac{F_a(\sqrt{P_{1dB}})^2}{P_u} \right) \tag{2.6}$$

where P_u is the mean power of the signal at the output of the NL device.

For purpose of theoretical studies, it's necessary, for a given HPA, to propose a mathematical or physical model to reproduce or approximate its NL effects in amplitude (AM/AM) and phase (AM/PM). In the literature, two main families of HPA models can be found: the memoryless HPA models and the HPA models with memory.

2.3 Memoryless HPA models

The output of a memoryless HPA is a function of the input at a given time instant or after a fixed time delay. Any change in the input occurs instantaneously at the output. In frequency domain the zero-memory nonlinearity implies that the transfer characteristics are frequency independent. Lets introduce some memoryless HPA models that will be used later in this report.

2.3.1 Soft Envelope Limiter

The Soft Envelope Limiter (SEL) is used for modeling a HPA with a perfect predistortion system. The global transfer function of the predistortion followed by the HPA is thus a limiter which can be described by the following AM/AM and AM/PM functions [2]:

$$\begin{aligned} F_a(\rho(t)) &= \begin{cases} \rho(t), \rho(t) \leq A_{\text{sat}} \\ A_{\text{sat}}, \rho(t) > A_{\text{sat}} \end{cases} \\ F_p(\rho(t)) &= 0 \end{aligned} \tag{2.7}$$

where A_{sat} is the HPA input saturation level.

2.3.2 Rapp model

This model, commonly used for modeling the Solid State Power Amplifiers (SSPA), was presented in [3] and exhibits only AM/AM conversion. It can be expressed as

$$\begin{aligned} F_a(\rho(t)) &= \frac{\rho(t)}{(1+(\frac{\rho(t)}{A_{\text{sat}}})^{2p})^{\frac{1}{2p}}} \\ F_p(\rho(t)) &= 0 \end{aligned} \tag{2.8}$$

where p is a smoothness factor that controls the transition from the linear region to the saturation region, $(p > 0)$. This HPA model assumes a linear performance for low amplitudes of the input signal. Then, a transition towards a constant saturated output is observed. When $p \to \infty$, the Rapp model converges towards the SEL. In figure 2-3, we plot the AM/AM characteristics of the Rapp model for two values of the smoothness factor p.

In the following of this report, we will refer to this HPA model with the acronym SSPA.

2.3.3 Saleh model

Saleh's model is generally used for modeling Travelling Wave Tube Amplifiers (TWTA) [4]. This HPA model has been mainly used in several works dealing with the impact of nonlinearities in OFDM systems [5, 6]. According to this model, the AM/AM and AM/PM conversion characteristics can be expressed as follows:

$$\begin{aligned} F_a(\rho) &= \frac{\alpha_a \rho(t)}{1 + \beta_a \rho(t)^2} \\ F_p(\rho) &= \frac{\alpha_p \rho(t)^2}{1 + \beta_p \rho(t)^2} \end{aligned} \tag{2.9}$$

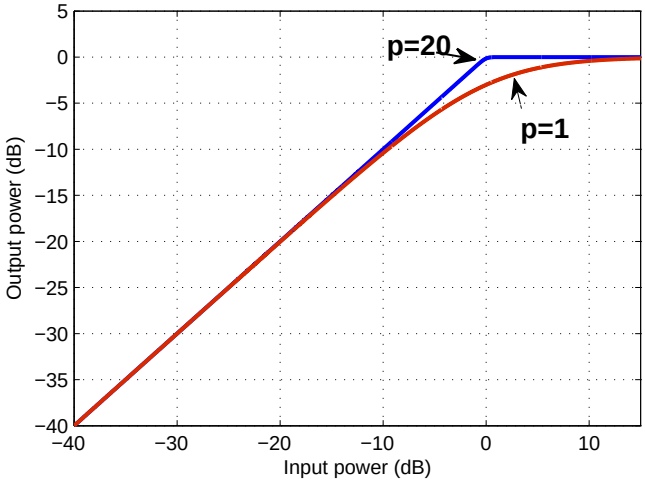


Figure 2-3: AM/AM characteristics of Rapp HPA model.

where α_a and β_a are the parameters to decide the NL amplitude distortion level, and α_p and β_p are phase displacements In figure 2.3, we plot the AM/AM and AM/PM characteristics of the Saleh model for different values of α_a, β_a, α_p and β_p.

In the literature we also found the following equations 2.10 for the modelling the AM/AM and AM/PM conversion characteristics of TWTA.

$$F_a(\rho) = A_{sat}^2 \frac{\rho(t)}{\rho(t)^2 + A_{sat}^2} \qquad (2.10)$$
$$F_p(\rho) = \varphi_0 \frac{\rho(t)^2}{\rho(t)^2 + A_{sat}^2}$$

where φ_0 controls the maximum phase distortion introduced by this HPA model. In the following of this report, we will refer to this model as TWTA model.

Its clear that both equations 2.9 and 2.10 allow the modeling of HPA exhibiting both NL amplitude and phase distortion.

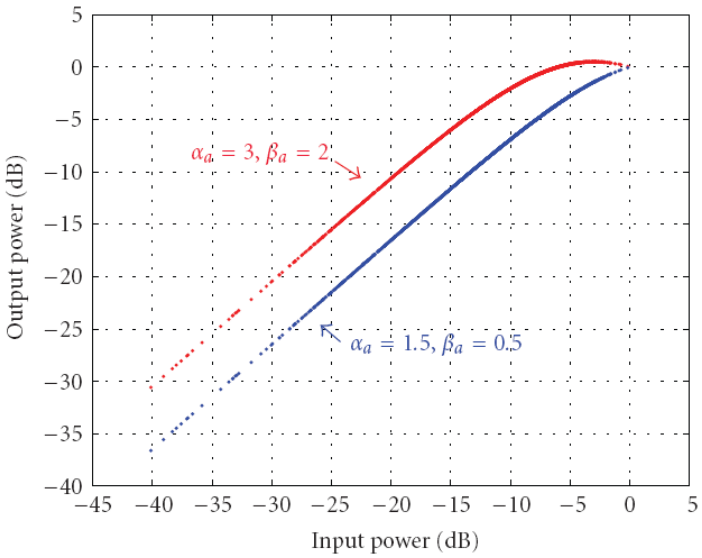
2.3.4 Polynomial model

For purpose of theoretical analysis of NL HPA effects, it can be suitable to assume or approximate the transfer function of the HPA with a polynomial model. In this case the signal $u(t)$ at the output of the NL device can be written

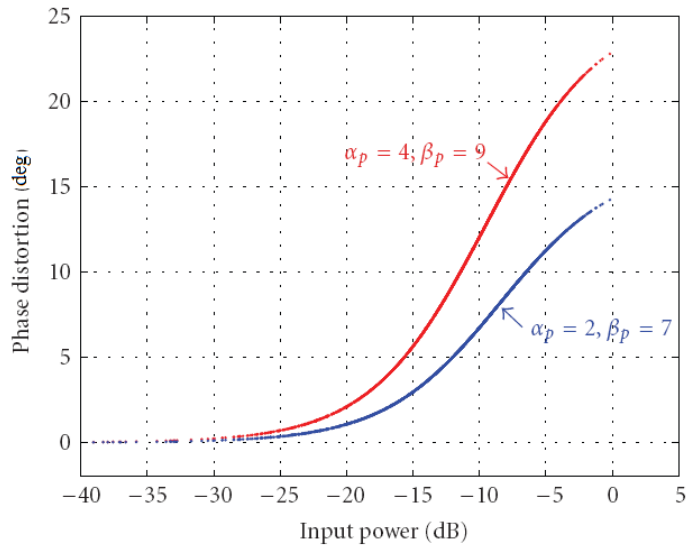
$$u(t) = \sum_{l=1}^{L} a_l i(t) \left|i(t)\right|^{l-1} \qquad (2.11)$$

where

- L is the polynomial order, and
- a_l are the complex coefficients of the polynomial approximation.



(a) AM/AM characteristics.



(b) AM/PM characteristics.

Figure 2-4: AM/AM and AM/PM characteristics of Saleh HPA model.

In some works related to the study of spectral regrowth for OFDM systems [7], the polynomial models used, exhibit only odd coefficients for fitting the AM/AM and AM/PM curves. Note that in Zhou's work [8], such HPA model is adopted because only odd order nonlinearities contribute to spectral broadening.

2.4 HPA models with memory

For wideband signals, which are typically based on multicarrier modulation, the frequency dependency of the HPA characteristics becomes important. A distortion effect called memory effect appears in the power response of the amplifier.

In HPA with memory, the output at time t_o depends on the input signal at time t_o but also on the input signal before time t_o. Furthermore, both the gain and phase distortion may be frequency-dependent. A detailed discussion of nonlinearities with and without memory can be found in [9]. As a model of the HPA with memory, it is considered to be a Hammerstein system which can be represented by a memoryless HPA followed by a linear filter (see figure 2-5)) [6].

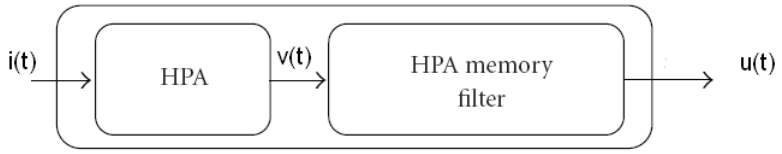


Figure 2-5: Hammerstein model for a HPA with memory.

The signal $v(t)$ is the classical memoryless amplified signal equal to $S(\rho(t))\exp(j\varphi(t))$. The signal $u(t)$ at the output of the HPA bloc is

$$u(t) = v(t) * f(t) \tag{2.12}$$

where $*$ stands for the convolution product and $f(t)$ is the impulse response of the HPA memory filter.

The baseband behavior of a power amplifier with memory can also be described by polynomials which discrete time model is described by the following equation

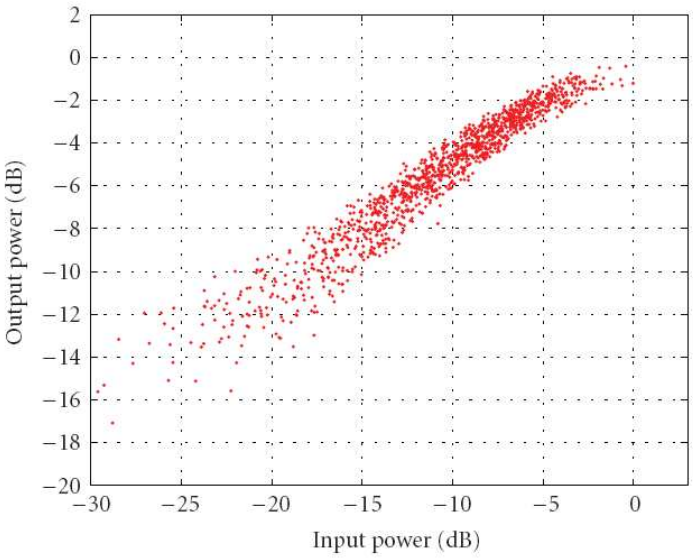
$$u(n) = \sum_{l=1}^{L}\sum_{k=1}^{K} a_{l,k} i(n-k)\,|i(n-k)|^{l-1} \tag{2.13}$$

where L is the order of the polynomial model and K is the memory length. Figure 2.6 shows the AM/AM and AM/PM characteristics of an amplifier with memory effects.

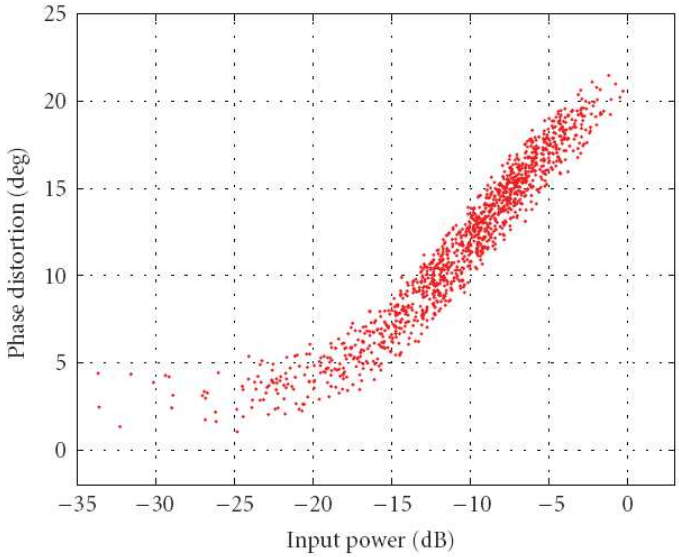
We can see that the AM/AM and AM/PM characteristics of figure 2.6 show a dispersive behavior as compared to the memoryless case. The dispersion of these characteristics is directly related to the order of the memory filter.

2.5 Conclusion

In this chapter, we have introduced some HPA characteristics and classifications in terms of amplitude distortion, phase distortion and memory effects. We underline that in this report, only memoryless HPA models will be considered. However, some parts of our studies can be easily expandable to HPA models with memory.



(a) AM/AM characteristic.



(b) AM/PM characteristic.

Figure 2-6: AM/AM and AM/PM characteristics of a HPA with memory.

3. Impact of nonlinearities on in-band distortion

3.1 Introduction

As multicarrier techniques, FBMC and OFDM exhibit large PAPR [10, 11, 12], i.e., large fluctuations in their signal envelope, making them more sensitive to Nonlinear distortion (NLD) caused by the HPA.

In this chapter we will study the Bit Error Rate (BER) performance in the presence of memoryless NL HPA for both FBMC system as well as classical OFDM one. This study is carried out using additive white Gaussian noise (AWGN) and Rayleigh fading channel models.

A theoretical characterization of NLD effects on OFDM systems has been proposed in [13], where the authors focused on the impact of the NL amplitude distortions induced by three HPA models: the SEL, the SSPA, and the TWTA. In this paper, the authors, proposed a theoretical characterization of the NLD parameters. We note that, except for the SEL HPA model, the investigation presented in [13] gives only semi-analytical results which could not be easily extended to real HPA with measured characteristics. Other contributions [14, 15] used the results presented in [13] to study the effect of HPA on Multiple-Input Multiple-Output (MIMO) transmit diversity systems.

Our aim is to evaluate the impact of the in-band distortions on OFDM and FBMC modulations when a memoryless NL HPA is used. In another way, the approach presented in this chapter extends the results of [13] to any modeled or measured memoryless HPA. The polynomial fitting of the amplitude-amplitude modulation (AM/AM) and amplitude-phase modulation (AM/PM) conversion characteristics allows complete theoretical characterization of the NL distortion parameters for both multicarrier modulation schemes.

We will investigate the performance of FBMC and OFDM in the case of a perfect phase correction at the receiver side (this means principally that channel identification is perfectly done at the receiver). Analytical closed-form expressions of the BER will be established based on polynomial decomposition of the HPA NL characteristics. The method proposed hereafter can be applied for any memoryless HPA model and even for real measured ones.

3.2 System model

Let's consider a FBMC and OFDM transceiver with memoryless NL HPA as shown in Figure 3-1. We investigate the impact of NLD on BER performance in the case of AWGN and fading Rayleigh channels. We underline that all results can be generalized to frequency-selective channel. In the following, we will recall briefly the architecture of the OFDM and FBMC systems.

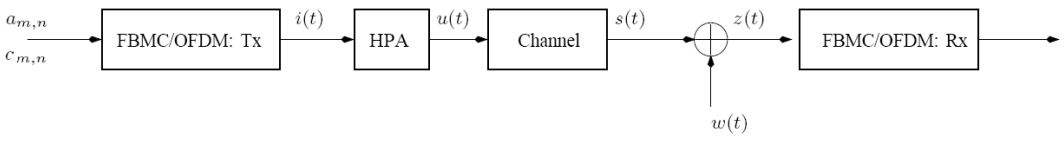


Figure 3-1: The transmission system model with FBMC and OFDM modulations.

3.2.1 OFDM and FBMC modulations in brief

3.2.1.1 OFDM

In OFDM system, bits are mapped to constellation symbols where the modulation and demodulation are, respectively, implemented by the Inverse Fast Fourier Transform (IFFT) and the Fast Fourier Transform (FFT). The time-domain representation of an OFDM symbol calculated with N IFFT point is given by

$$i(t) = \sum_{n=-\infty}^{+\infty} \sum_{m=0}^{N-1} c_{m,n} f(t - nT) e^{j\frac{2\pi}{T}mt} \tag{3.1}$$

where

- N is the number of subcarriers,
- T is the OFDM symbol period,
- $c_{m,n}$ is a complex-valued symbol transmitted on the mth subcarrier and at the instant nT, and
- $f(t)$ is a rectangular time window, defined by

$$f(t) = \begin{cases} \frac{1}{\sqrt{T}} & t \in [0, T] \\ 0 & \text{elsewhere} \end{cases}.$$

Considering high values of N and according to the central limit theorem [16], the IFFT block transforms a set of independent complex random variables to a set of complex Gaussian random ones.

In a distortion-free noiseless channel, the received information is given by the following equation

$$\begin{aligned} y_{m_0,n_0} &= \langle i(t), f(t - n_0T) e^{j\frac{2\pi}{T}m_0t} \rangle \\ &= \int_{-\infty}^{+\infty} i(t) f(t - n_0T) e^{-j\frac{2\pi}{T}m_0t} dt \\ &= \sum_{n=-\infty}^{+\infty} \sum_{m=0}^{N-1} \int_{-\infty}^{+\infty} c_{m,n} f(t - nT) f(t - n_0T) e^{j\frac{2\pi}{T}(m-m_0)t} dt \\ &= c_{m_0,n_0} \end{aligned} \tag{3.2}$$

where $\langle ., . \rangle$ stands for the inner product.

3.2.1.2 FBMC

The considered FBMC system is transmitting Offset Quadrature Amplitude Modulation (OQAM) symbols [17, 18], where the in-phase and the quadrature components are time staggered by half a symbol period, $T/2$. Moreover, for two adjacent subcarriers, if we consider that the time delay $T/2$ is introduced into the imaginary part of the QAM symbols on adjacent subcarriers, then it is introduced into the real part of the symbols on the other one as shown on figure 3-2.

Accordingly, the baseband continuous-time model of the FBMC transmitted signal can be defined as follows [17]:

$$i(t) = \sum_{n=-\infty}^{+\infty} \sum_{m=0}^{N-1} a_{m,n} h(t - nT/2) e^{j\frac{2\pi}{T}mt} e^{j\varphi_{m,n}} \tag{3.3}$$

where

- $a_{m,n}$ is a real symbol transmitted on the m^{th} subcarrier and at the instant nT,
- $h(t)$ is the prototype filter impulse response, and
- $\varphi_{m,n}$ is the phase term which is given by

$$\varphi_{m,n} = \frac{\pi}{2}(m+n) - \pi mn$$

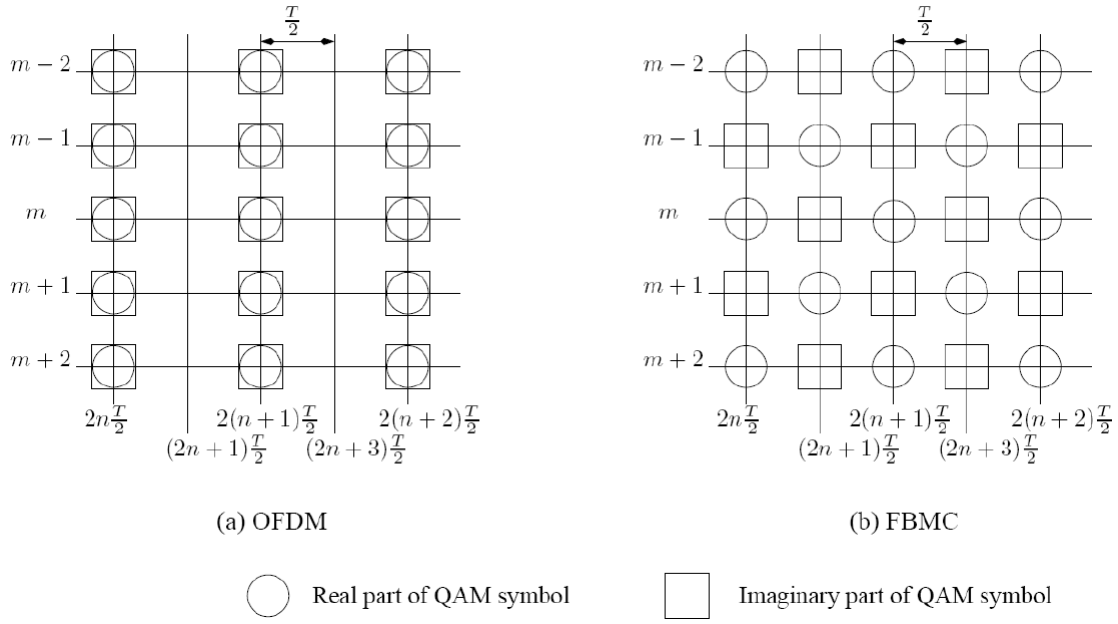


Figure 3-2: OFDM and FBMC symbol mapping on subcarriers. **(a)** OFDM and **(b)** FBMC.

Let $\gamma_{m,n}(t)$ be a time and frequency shifted version of $h(t)$

$$\gamma_{m,n}(t) = h(t - nT/2) e^{j\frac{2\pi}{T}mt} e^{j\varphi_{m,n}} \tag{3.4}$$

Then, we can rewrite equation 3.3 as follows:

$$i(t) = \sum_{n=-\infty}^{+\infty} \sum_{m=0}^{N-1} a_{m,n} \gamma_{m,n}(t) \tag{3.5}$$

In a distortion-free noiseless channel, the demodulated signal y_{m_0,n_0} at time instant n_0 and subcarrier m_0 is given by

$$\begin{aligned} y_{m_0,n_0} &= \langle i(t), \gamma_{m_0,n_0}(t) \rangle = \int_{-\infty}^{+\infty} i(t)\gamma^*_{m_0,n_0}(t)dt \\ &= \sum_{n=-\infty}^{+\infty} \sum_{m=0}^{N-1} a_{m,n} \int_{-\infty}^{+\infty} \gamma_{m,n}(t)\gamma^*_{m_0,n_0}(t)dt \\ &= a_{m_0,n_0} + \sum_n \sum_m \sum_{(m,n)\neq(m_0,n_0)} \int_{-\infty}^{+\infty} \gamma_{m,n}(t)\gamma^*_{m_0,n_0}(t)dt \end{aligned} \tag{3.6}$$

where $\gamma^*_{m_0,n_0}(t)$ is the complex conjugate of $\gamma_{m_0,n_0}(t)$

According to [19], the prototype filter is designed such that the intrinsic interference term is orthogonal to the useful symbol, i.e., it is purely imaginary.

$$ju_{m_0,n_0} = \sum_n \sum_m \sum_{(m,n)\neq(m_0,n_0)} \underbrace{\int_{-\infty}^{+\infty} \gamma_{m,n}(t)\gamma^*_{m_0,n_0}(t)dt}_{\Psi_{\Delta m,\Delta n}} \tag{3.7}$$

Considering the PHYDYAS prototype filter proposed in [19], the coefficients $\Psi_{\Delta m,\Delta n}$ are given in table 3-1. Consequently, a nearly perfect reconstruction of the transmitted real symbols $a_{m,n}$ is obtained by taking the real part (OQAM decision) of the demodulated signal y_{m_0,n_0}.

	n_0-3	n_0-2	n_0-1	n_0	n_0+1	n_0+2	n_0+3
m_0-1	$0.043j$	-0.125	$-0.206j$	0.239	$0.206j$	-0.125	$-0.043j$
m_0	-0.067	0	0.564	1	0.564	0	-0.067
m_0+1	$-0.043j$	-0.125	$0.206j$	0.239	$-0.206j$	-0.125	$0.043j$

Table 3-1: Transmultiplexer impulse response

3.2.2 HPA model

A HPA model or a real measured one can be entirely described by its input/output or transfer function characteristics. The AM/AM and AM/PM characteristics indicate the relationship between, respectively, the modulus and the phase variation of the output signal as functions of the modulus of the input one.

The amplified signal $u(t)$ can be written as

$$\begin{aligned} u(t) &= F_a(\rho(t)) \exp(jF_p(\rho(t))) \exp(j\varphi(t)) \\ &= S(\rho(t)) \exp(j\varphi(t)) \end{aligned} \tag{3.8}$$

where

- $\rho(t)$is the input signal modulus,
- $\varphi(t)$ is the input signal phase,

- $F_a(\rho(t))$ is the AM/AM characteristic of the HPA,
- $F_p(\rho(t))$ is the AM/PM characteristic of the HPA, and
- $S(\rho(t)) = F_a(\rho(t))\exp(jF_p(\rho(t)))$ is the complex soft envelop of the amplified signal $u(t)$.

Then, the signal $z(t)$ at the input of the demodulator can be written as

$$z(t) = h_c(t) * u(t) + w(t) \tag{3.9}$$

where

- $h_c(t)$ is the channel impulse response,
- $w(t)$ is a zero mean white Gaussian noise, and
- $*$ stands for the convolution product.

In our analysis, we will consider the memoryless HPA models introduced in section 2.3.

3.3 Nonlinear distortion modeling

When considering a large number of subcarriers N, the input signal $i(t)$ is assumed to be a zero mean, complex Gaussian random process. According to the Bussgang theorem [2, 20, 21], the NL HPA output $u(t)$ is related to the input $i(t)$ by the following equation:

$$u(t) = K(t)i(t) + d(t) \tag{3.10}$$

where

- $d(t)$ is a zero mean noise, which is uncorrelated with $i(t)$.
- $K(t)$ is a complex gain with modulus $|K(t)|$ and phase $\phi_K(t)$.

For a high number of subcarriers N, the mean of the complex Gaussian random process $i(t)$ tends to zero. In this case, $K(t)$ can be expanded as a Fourier series

$$K(t) = \sum_{l=-\infty}^{+\infty} k_l e^{j2\pi lt/T} \tag{3.11}$$

where k_i is the Fourier coefficient given by

$$k_l = \int_{-T/2}^{T/2} K(t)e^{-j2\pi lt/T}. \tag{3.12}$$

The signal at the output of the HPA can be written as

$$u(t) = \sum_{l=-\infty}^{+\infty} i(t)k_l e^{j2\pi lt/T} + d(t). \tag{3.13}$$

For both OFDM and FBMC modulations, it is announced in [13] that $k_l = 0$ for $l > 0$. We can write then the signal at the output of the HPA:

$$u(t) = k_0 i(t) + d(t) = Ki(t) + d(t) \tag{3.14}$$

For simplicity sake, we will discard, in the following equations, the time variable t, from ρ and φ. According to [13], K can be computed analytically by

$$K = \frac{1}{2}\mathbb{E}\left[\frac{\partial S(\rho)}{\partial \rho} + \frac{S(\rho)}{\rho}\right] \tag{3.15}$$

where $\mathbb{E}$ is the expectation operator. We recall that $S(\rho) = F_a(\rho)\exp(jF_p(\rho))$ is the complex soft envelop of the amplified signal $u(t)$.

The variance σ_d^2 of the NL distortion $d(t)$ is given by the following equation:

$$\sigma_d^2 = \mathbb{E}(|d(t)|^2) = \mathbb{E}\left(|S(\rho)|^2\right) - |K|^2\,\mathbb{E}(\rho^2). \tag{3.16}$$

In table 3-2, we compare the NLD parameter values given by equations 3.15 and 3.16 for both OFDM and FBMC by considering Saleh's HPA model with $\varphi_0 = \pi/6$ and $A_{\text{sat}} = 1$ in equation (2.10). The estimation of the parameters K and σ_d^2 is made with 10^6 4QAM symbols using several values of subcarriers N. The comparison is made for two values of IBO of 4 and 8 dB.

	OFDM		**FBMC**	
$\boldsymbol{N}$	$\boldsymbol{K}$	$\boldsymbol{\sigma_d^2}$	$\boldsymbol{K}$	$\boldsymbol{\sigma_d^2}$
IBO = 4 dB				
4	$0.5796 + 0.1137j$	1.6392×10^{-2}	$0.5792 + 0.1137j$	1.6272×10^{-2}
64	$0.5912 + 0.1107j$	1.1338×10^{-2}	$0.5918 + 0.1107j$	1.1339×10^{-2}
1024	$0.5916 + 0.1106j$	1.1339×10^{-2}	$0.5923 + 0.1104j$	1.1339×10^{-2}
IBO = 8 dB				
4	$0.7662 + 0.0868j$	7.0879×10^{-3}	$0.7677 + 0.0858j$	6.9633×10^{-3}
64	$0.7728 + 0.0830j$	2.4249×10^{-3}	$0.7728 + 0.0831j$	2.4256×10^{-3}
1024	$0.7727 + 0.0830j$	2.4256×10^{-3}	$0.7728 + 0.0830j$	2.4258×10^{-3}

Table 3-2: Comparison between estimated values of $K$and $\boldsymbol{\sigma_d^2}$ for both nonlinearly amplified OFDM and FBMC signals

The results illustrated in table 3-2 show that for a sufficiently high number of subcarriers N, the OFDM and FBMC modulated signals, which are considered as Gaussian signals (according to the central limit theorem [16]), can be modeled by the same NLD parameters K and σ_d^2 when they are passed through a given NL HPA.

3.4 Analytical computation of K and σ_d^2

The analytical computation of the NLD parameters K and σ_d^2 depends on the complexity of the expression of $S(\rho)$. Indeed and based on equations 3.15 and 3.16, the authors in [13] computed analytically K and σ_d^2 in the case of the SEL HPA model. In this case, K and σ_d^2 are expressed as

$$K = (1 - e^{-\frac{A_{\text{sat}}^2}{\sigma^2}}) + \frac{1}{2}\sqrt{\pi\frac{A_{\text{sat}}^2}{\sigma^2}}\text{erfc}\left(\sqrt{\frac{A_{\text{sat}}^2}{\sigma^2}}\right) \tag{3.17}$$

$$\sigma_d^2 = \sigma^2(1 - e^{-\frac{A_{\text{sat}}^2}{\sigma^2}} - K^2). \tag{3.18}$$

Nevertheless, for more complicated expressions of $S(\rho)$, such as (2.8) and (2.10) (SSPA and TWTA models), the derivation of analytical expressions for the parameters K and σ_d^2 is intractable. In [13], no closed-form expression for K and σ_d^2 is given for SSPA and TWTA HPA models. In order to simplify the computation and obtain analytical expressions for K and σ_d^2 for any HPA model, we propose a polynomial approximation of $S(\rho)$. By doing this, we will be able to analytically compute the NLD parameters of equations 3.15 and 3.16 for any HPA conversion characteristics after polynomial fitting.

3.4.1 Proposed method

Our approach aims to approximate the HPA conversion characteristics by a polynomial model [22], which can be written as

$$u(t) = \sum_{l=1}^{L} a_l i(t) \left|i(t)\right|^{l-1} \tag{3.19}$$

where

- L is the polynomial order, and
- a_l are the complex coefficients of the polynomial approximation.

In classical polynomial models existing in literature, only odd coefficients are generally used for fitting the AM/AM curve [7]. In order to better fit the complex soft envelope $S(\rho)$ of the amplified signal, we have chosen to use a full rank order polynomial with odd and even coefficients. By using the polynomial approximation of equation 3.19, the new HPA output is given by

$$\begin{aligned} u(t) &= e^{j\varphi} \sum_{l=1}^{L} a_l \rho^l \\ &= e^{j\varphi} S(\rho) \end{aligned} \tag{3.20}$$

where the new expression of $S(\rho)$ is equal to

$$S(\rho) = \sum_{l=1}^{L} a_l \rho^l \tag{3.21}$$

The complex valued polynomial coefficients a_l, $l = 1..L$ can be easily obtained by using a classical least squares method [8].

3.4.2 Analytical computation of K and σ_d^2 using polynomial approximation

Using the polynomial approximation of $S(\rho)$, we simplify the computation of K and σ_d^2 given by equations 3.15 and 3.16. This will be achieved by the computation of the expectation of a power of Rayleigh random variable, $\mathbb{E}[\rho^l]$, where, $l = 1.....2L$. Equation 3.15 can be rewritten as

$$K = \frac{1}{2} \sum_{l=1}^{L} (l+1) a_l \mathbb{E}\left[\rho^{l-1}\right]. \tag{3.22}$$

The variance σ_d^2 of the NLD $d(t)$ given in equation 3.16 becomes

$$\sigma_d^2 = \sum_{l=1}^{L} |a_l|^2 \, \mathbb{E}\left[\rho^{2l}\right] + 2 \sum_{n,l=1,n\neq l}^{L} \Re[a_n a_l] \mathbb{E}\left[\rho^{n+l}\right] - |K|^2 \, \mathbb{E}\left[\rho^2\right] \tag{3.23}$$

where $\Re[.]$ stands for the real part.

The above theoretical expressions of K and σ_d^2 involve the computation of the expectation of ρ^n (n is a positive integer). This expectation is equivalent to calculate the n^{th} derivation of the Moment Generating Function (MGF).

We can write $\mathbb{E}[\rho^l]$ as

$$\mathbb{E}[\rho^l] = \left.\frac{\partial^l M(t)}{\partial t^l}\right|_{t=0} \tag{3.24}$$

where

- l is a positive integer, and
- $M(t)$ is the MGF given by

$$M(t) = e^{\rho t}. \tag{3.25}$$

A generic expression for the computation of $\mathbb{E}[\rho^l]$ is given in [8]. It is expressed as follows:

- For odd values of l, we have

$$\begin{aligned} \mathbb{E}\left[\rho^l\right] &= \left.\frac{\partial^l M(t)}{\partial t^l}\right|_{t=0} \\ &= \sqrt{\frac{\pi}{2}} \sigma^l \prod_{i=0}^{\frac{l-1}{2}} (2i+1). \end{aligned} \tag{3.26}$$

- For even values of l, we have

$$\begin{aligned} \mathbb{E}\left[\rho^l\right] &= \left.\frac{\partial^l M(t)}{\partial t^l}\right|_{t=0} \\ &= (\sqrt{2}\sigma)^l (\frac{l}{2})! \end{aligned} \tag{3.27}$$

where ! stands for the factorial operator.

Using equations 3.22, 3.26, and 3.27, we have finally for the NL parameter K

$$\begin{aligned} K = &\sqrt{\frac{\pi}{8}} \sum_{l=1, l \text{ odd}}^{L} (l+1) a_l \sigma^l \prod_{i=0}^{\frac{l-1}{2}} (2i+1) \\ &+ \frac{1}{2} \sum_{l=2, l \text{ even}}^{L} (l+1) a_l (\sqrt{2}\sigma)^l (\frac{l}{2})! \end{aligned} \tag{3.28}$$

For the variance σ_d^2 of the NL noise $d(t)$, we obtain the following expression:

$$\begin{aligned} \sigma_d^2 = &\sum_{l=1}^{L} |a_l|^2 \, 2^l \sigma^{2l} l! - 2 \, |K|^2 \, \sigma^2 \\ &+ \sqrt{\frac{4\pi}{2}} \sum_{n,l=1, n\neq l, (n+l) \text{ odd}}^{L} \Re[a_n a_l] \sigma^{n+l} \prod_{i=0}^{\frac{n+l-1}{2}} (2i+1) \\ &+ 2 \sum_{n,l=1, n\neq l, (n+l) \text{ even}}^{L} \Re[a_n a_l] (\sqrt{2}\sigma)^{n+l} (\frac{n+l}{2})! \end{aligned} \tag{3.29}$$

We should note that both K and σ_d^2 are function of the signal IBO. Indeed, the variance σ of the signal at the input of the HPA can be written as

$$\sigma = \frac{A_{\text{sat}}}{\sqrt{10^{IBO/10}}}. \tag{3.30}$$

3.4.2.1 Validation of the analytical expressions of K and σ_d^2

In order to validate our analytical analysis of K and σ_d^2 (equations 3.28 and 3.29), at first, we will compute by simulation the values of K and σ_d^2 obtained, respectively, by equations 3.15 and 3.16 for a given HPA model (SSPA or TWTA). After approximation of each HPA model with the polynomial model of order $L = 10$, the parameters K and σ_d^2 can be theoretically computed based on equations 3.28 and 3.29. Table 3-3 compares the simulated and theoretically computed values for different HPA models and different scenarios. The results are given for 10^6 4QAM symbols modulated over 64 subcarriers. For the TWTA model, we have $A_{\text{sat}} = 1$, and for the SSPA one, p is fixed to 1.

		Simulation		**Theoretical**	
IBO (dB)	φ_0	K **(eq 3.15)**	σ_d^2 **(eq 3.16)**	K **(eq 3.28)**	σ_d^2 **(eq 3.29)**
SSPA					
4	-	0.7699	4.4759×10^{-3}	0.7690	4.4431×10^{-3}
6	-	0.8307	1.8950×10^{-3}	0.8297	1.8722×10^{-3}
8	-	0.8798	7.0742×10^{-4}	0.8785	7.0583×10^{-4}
Saleh					
4	0	0.6042	1.0330×10^{-2}	0.6036	1.0317×10^{-2}
6	0	0.6976	4.9589×10^{-3}	0.6969	4.9654×10^{-3}
8	0	0.7784	2.1228×10^{-3}	0.7775	2.1030×10^{-3}
4	$\pi/6$	$0.5917 + 0.1106j$	1.1339×10^{-2}	$0.5904 + 0.1068j$	1.1271×10^{-2}
6	$\pi/6$	$0.6887 + 0.0995j$	5.5901×10^{-3}	$0.6870 + 0.0948j$	5.5812×10^{-3}
8	$\pi/6$	$0.7727 + 0.0830j$	2.4194×10^{-3}	$0.7727 + 0.0830j$	2.4345×10^{-3}

Table 3-3: Comparison between numerical and theoretical values of K and σ_d^2

According to table 3-3, we observe, with a polynomial approximation of order $L = 10$, a very good agreement between simulation and theoretical results for both K and σ_d^2. As confirmed by the error criterion, there is a good accuracy of the analytical expressions proposed for the computation of K and σ_d^2 with respect to the computation based on equations 3.15 and 3.16.

3.4.2.2 Influence of polynomial approximation order

In table 3-4, we compare the NLD parameter values given by equations 3.28 and 3.29 with an FBMC modulated signal and for different values of the polynomial approximation order L (equation 3.19). In this table, we consider a Saleh HPA model with $\varphi_0 = \pi/6$, $A_{\text{sat}} = 1$, and $\text{IBO} = 8$ dB.

Results illustrated in table 3-4 show that for a sufficiently high order of the polynomial approximation L, the theoretically estimated values of K and σ_d^2 based on equations 3.28 and

L	K	σ_d^2
5	$0.7976 + 0.1570j$	3.1941×10^{-3}
7	$0.8248 + 0.0713j$	3.8676×10^{-3}
10	$0.7728 + 0.0830j$	2.4345×10^{-3}
15	$0.7728 + 0.0830j$	2.4345×10^{-3}
20	$0.7728 + 0.0830j$	2.4345×10^{-3}
30	$0.7728 + 0.0830j$	2.4345×10^{-3}
100	$0.7728 + 0.0830j$	2.4345×10^{-3}
Saleh model	$0.7728 + 0.0830j$	2.4345×10^{-3}

Table 3-4: Impact of the polynomial order approximation on the estimated values of K and σ_d^2

3.29 are stable and correspond to the numerically simulated ones (equations 3.15 and 3.16). It must also be noted that the polynomial order L can be chosen very high without additional complexity. Indeed, as soon as coefficients a_l are computed for a given HPA (using a classical least squares method), the computation of K and σ_d^2 is straightforward using equations 3.28 and 3.29.

3.5 Theoretical performance analysis

The received signal after HPA and channel filtering can be expressed, after substituting $u(t)$ in Equation 3.9 by the expression of Equation 3.10, as

$$z(t) = i(t) * [Kh_c(t)] + d(t) * h_c(t) + w(t). \tag{3.31}$$

Looking at equation 3.31, it is clear that the effect of the NL factor K will be taken into account during frequency equalization at the receiver side ($h_c(t)$ and K will be estimated jointly). We will carry in Section 3.5.1 a theoretical analysis of the BER in an AWGN channel after correction of the phase rotation related to the factor K. Section 3.5.2 is dedicated to the BER analysis of OFDM and FBMC modulations in the case of a flat fading Rayleigh channel.

3.5.1 Performance analysis in the case of an AWGN channel

In the case where we assume a perfect estimation of the NLD parameter K, after compensation for this factor, at the receiver side, we can rewrite the signal at the input of OFDM and FBMC Rx as

$$z(t) = i(t) + (d(t) + w(t))\frac{1}{K}. \tag{3.32}$$

For an M-array QAM, the BER after compensation for the factor K can be written as follows [23]

$$\mathrm{BER}_{\mathrm{MQAM}}^{\mathrm{AWGN,\ K\ corrected\ for}} = \frac{2(\sqrt{M}-1)}{\sqrt{M}\log_2(M)}\mathrm{erfc}\left(\sqrt{\left(\frac{3\log_2(M)E_{bavg}}{2(M-1)N_0}\right)}\right) \tag{3.33}$$

where

- M is the alphabet of the modulation,
- E_{bavg} is the average energy per bit normalized to 1, and
- $N_0/2$ is the power spectral density of the additive noise.

From equation 3.32, it can be clearly seen that the power spectral density N_0, after correction of the NL factor K, is given by

$$N_0 = \frac{(\sigma_w^2 + \sigma_d^2)}{|K|^2} 2T. \tag{3.34}$$

where

- σ_w^2 is the variance of the AWGN,
- σ_d^2 is the variance of the NL distortion $d(t)$, and
- T is the symbol duration.

We can finally rewrite equation 3.33 as follows:

$$\mathrm{BER}_{\mathrm{MQAM}}^{\mathrm{AWGN,\,K\,corrected\,for}} = \frac{2(\sqrt{M}-1)}{\sqrt{M}\log_2(M)} \mathrm{erfc}\left(\sqrt{\left(\frac{3\log_2(M)|K|^2}{4(M-1)T(\sigma_w^2+\sigma_d^2)}\right)}\right). \tag{3.35}$$

When the NL parameter K is not compensated for at receiver side, the FBMC system is shown to be more sensitive to phase distortions than the OFDM one [24]. The sensitivity of the FBMC system to phase distortion is directly related to the intrinsic interference term introduced by this modulation. This sensitivity cannot be seen as a limitation to FBMC modulation, since the phase error is practically taken into account during the channel estimation/equalization process.

3.5.2 BER analysis in the case of a Rayleigh channel

We assume a slowly varying flat fading Rayleigh channel with a coherence time larger than the symbol duration. The Rayleigh fading amplitude α follows the probability density function (pdf)

$$p_\alpha(\alpha) = \frac{\alpha}{\Omega} e^{(-\alpha^2/\Omega)} \tag{3.36}$$

where $\Omega = \mathbb{E}[\alpha^2]$ is the average fading power.

Also, its power α^2 is an exponentially distributed random variable with a pdf expressed as

$$p_{\alpha^2}(\alpha) = \frac{1}{\Omega} e^{(-\alpha/\Omega)}. \tag{3.37}$$

The nonlinearly amplified signal in a Rayleigh fading channel, with coherent detection, is given by equation 3.31. It is expressed as

$$\frac{h_c^*}{|h_c|^2 K} z(t) = i(t) + \frac{d(t)}{K} + \frac{h_c^*}{|h_c|^2 K} w(t). \tag{3.38}$$

Then, the instantaneous Signal-to-Noise Ratio (SNR) at the receiver can be expressed as

$$\gamma = \gamma_c \frac{\alpha^2}{\alpha^2 {\sigma_d}^2 + {\sigma_w}^2} \tag{3.39}$$

where $\gamma_c = |K|^2 E_b$ and E_b is the energy per bit.

Derivation of the pdf of γ

lemma Let $X = \alpha^2$ be an exponentially distributed random variable, then the SNR can be described as

$$\gamma = \gamma_c \frac{X}{X{\sigma_d}^2 + {\sigma_w}^2} = h(X). \tag{3.40}$$

$h(X)$ is strictly increasing continuously differentiable function with inverse $X = g(\gamma)$. Then, $\gamma = h(X)$ is continuous with probability density function $p_\gamma(\gamma)$ given by [25]

$$p_\gamma(\gamma) = p_X(g(\gamma))g'(\gamma) \tag{3.41}$$

where $g(\gamma) = {\sigma_w}^2\gamma/(\gamma_c - {\sigma_d}^2\gamma)$.

Then,

$$p_\gamma(\gamma) \quad = \begin{cases} \frac{{\sigma_w}^2\gamma_c}{\Omega(\gamma_c - {\sigma_d}^2\gamma)^2} e^{-\frac{{\sigma_w}^2\gamma}{\Omega(\gamma_c - {\sigma_d}^2\gamma)}}, & \text{if } 0 \le \gamma < \frac{\gamma_c}{{\sigma_d}^2} \\ 0 & \text{otherwise} \end{cases} . \tag{3.42}$$

The average BER can be calculated by averaging BER for instantaneous SNR over the distribution given in equation 3.42. For such MQAM modulation, the BER can be found using

$$\mathrm{BER} = \int_0^{\frac{\gamma_c}{{\sigma_d}^2}} \mathrm{BER}(\gamma) p_\gamma(\gamma) d\gamma. \tag{3.43}$$

Substituting the pdf $p_\gamma(\gamma)$ of equation 3.42 in the integral of equation 3.43 gives

$$\begin{aligned} \mathrm{BER}_{\mathrm{MQAM}}^{\mathrm{Rayleigh}} = & \int_0^{\frac{\gamma_c}{{\sigma_d}^2}} \frac{2(\sqrt{M}-1)}{\sqrt{M}\log_2(M)} \\ & \times \mathrm{erfc}\left(\sqrt{\left(\frac{3\log_2(M)\gamma}{(M-1)}\right)}\right) \frac{{\sigma_w}^2\gamma_c}{\Omega(\gamma_c - {\sigma_d}^2\gamma)^2} e^{-\frac{{\sigma_w}^2\gamma}{\Omega(\gamma_c - {\sigma_d}^2\gamma)}} d\gamma. \end{aligned} \tag{3.44}$$

3.6 Simulation results

In this section, we present numerical results illustrating the impact of memoryless HPA non-linearity on the performance of FBMC and OFDM systems under AWGN and Rayleigh fading channels. In this work, we have considered FBMC and OFDM systems with $N = 64$ subcarriers transmitting MQAM modulated symbols.

The BER is computed by averaging on 5×10^7 randomly generated FBMC and OFDM symbols. We will investigate the cases where transmission is achieved through AWGN and Rayleigh fading channels. For both OFDM and FBMC systems, we have considered three scenarios. In the first one, a SEL HPA model is used. In the second scenario, a Saleh HPA model with only AM/AM distortion is considered. In the last scenario, a Saleh HPA model is used, exhibiting both AM/AM and AM/PM distortions. In all the simulations, the curve referred by 'linear' in the legend corresponds to the case when the power amplifier is perfectly linear.

3.6.1 BER analysis in the case of an AWGN channel

Using equation 3.35, we first compare theoretical and simulation results for both OFDM and FBMC in the case of 16QAM modulated symbols and transmitted over an AWGN channel.

For the results, we assume a perfect compensation for the NLD parameter K. In figure 3-3, we present the results obtained in the presence of the SEL amplifier for both OFDM and FBMC systems. From this figure, we can notice that both OFDM and FBMC show the same performance. Additionally, there is an excellent match between theoretical results and those obtained by simulation.

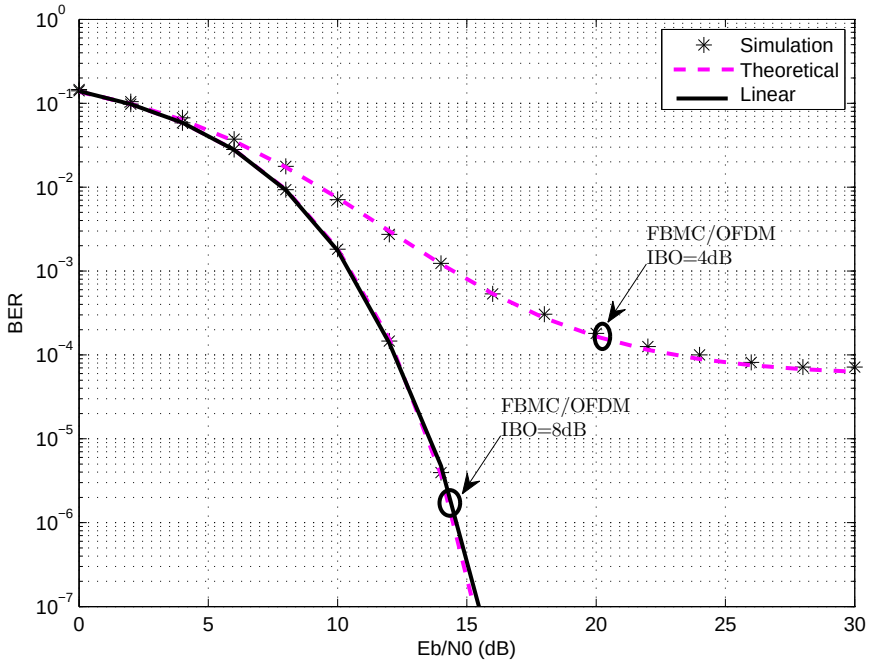


Figure 3-3: BER vs $\boldsymbol{Eb/N0}$ for OFDM and FBMC system. SEL, $A_{sat} = 1$, 64 subcarriers, 16QAM, and AWGN channel.

In figures 3-4 and 3-5, the performance of OFDM and FBMC systems in the presence of Saleh's HPA model with both AM/AM and AM/PM distortions is plotted. In these results, we compensate for the estimated NLD parameter K at the receiver side. Figure 3-4 shows the OFDM and FBMC performance in the case where only an AM/AM distortion is induced by the HPA. In figure 3-5, a Saleh HPA with $A_{\text{sat}} = 1$ and $\varphi_0 = \pi/6$ is used. For both figures, the theoretical results are obtained by polynomial approximation of order 10 for the Saleh model. When there is only amplitude distortion, the case of figure 3-4, both modulation schemes show the same performances which is also in accordance with the results shown in figure 3-3. When both amplitude and phase distortion are introduced by the HPA, the case of figure 3-5 and after correction for the phase error, both OFDM and FBMC modulations show also the same performance. We confirm by this result that a perfect compensation for the parameter K at the receiver side makes the FBMC system as efficient as the OFDM one in terms of BER. This is the case in practice since the phase rotation induced by the NL parameter K is taken into account by dedicated channel estimation and equalization algorithms.

3.6.2 BER analysis in the case of a Rayleigh channel

To further illustrate the effect of nonlinearity in the case of Rayleigh channel, the BER performance of FBMC, taking the 16QAM modulation scheme and Saleh's HPA model with an IBO

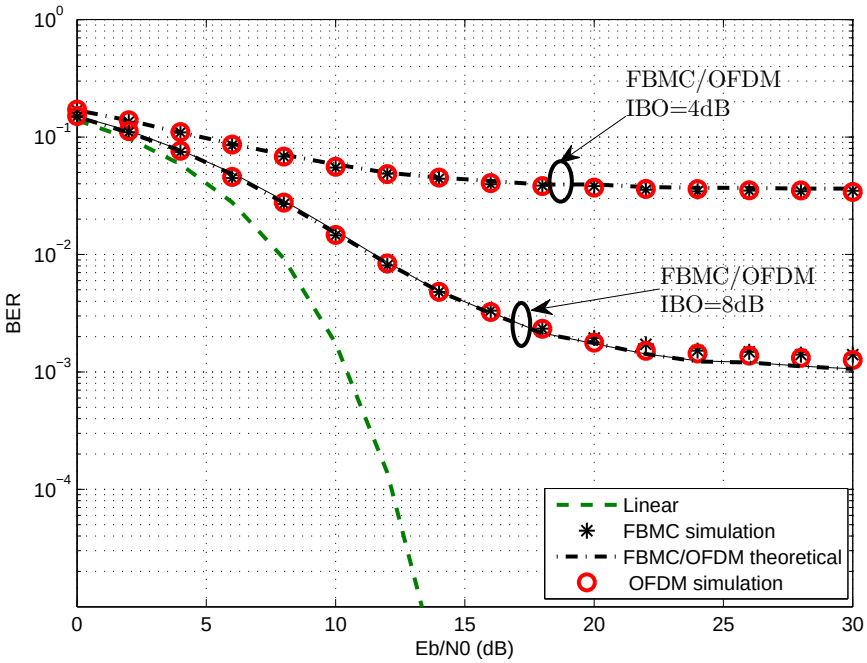


Figure 3-4: BER vs $\boldsymbol{Eb/N0}$ for OFDM and FBMC system. Saleh HPA model, 64 subcarriers, 16QAM, $\varphi_0 = 0$, and AWGN channel.

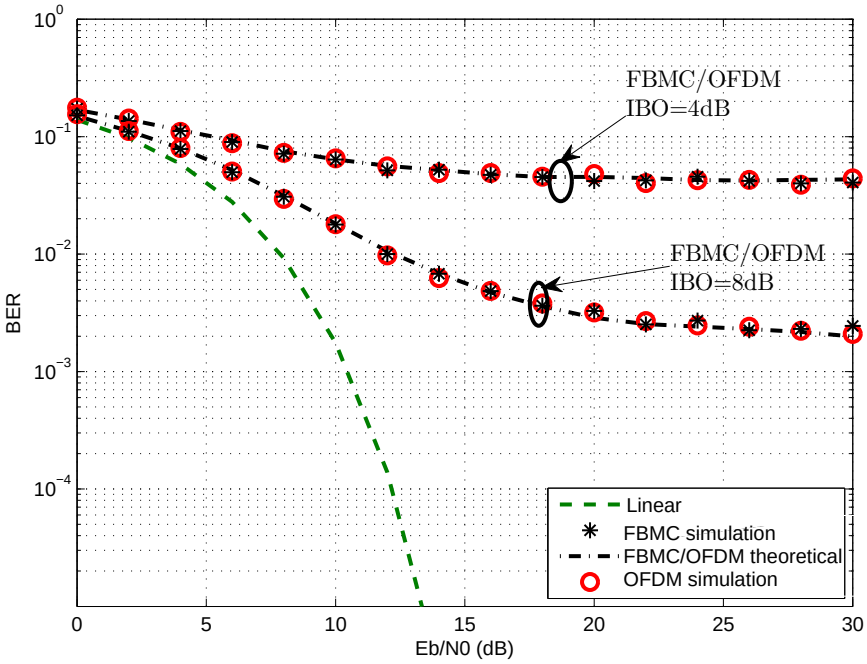


Figure 3-5: BER vs $\boldsymbol{Eb/N0}$ for OFDM and FBMC system. Saleh HPA model, 64 subcarriers, 16QAM, $\varphi_0 = \pi/6$, and AWGN channel.

of $6dB$, is shown in figure 3-6. The Rayleigh channel was assumed to be a slowly varying flat fading one at a rate slower than the symbol duration T.

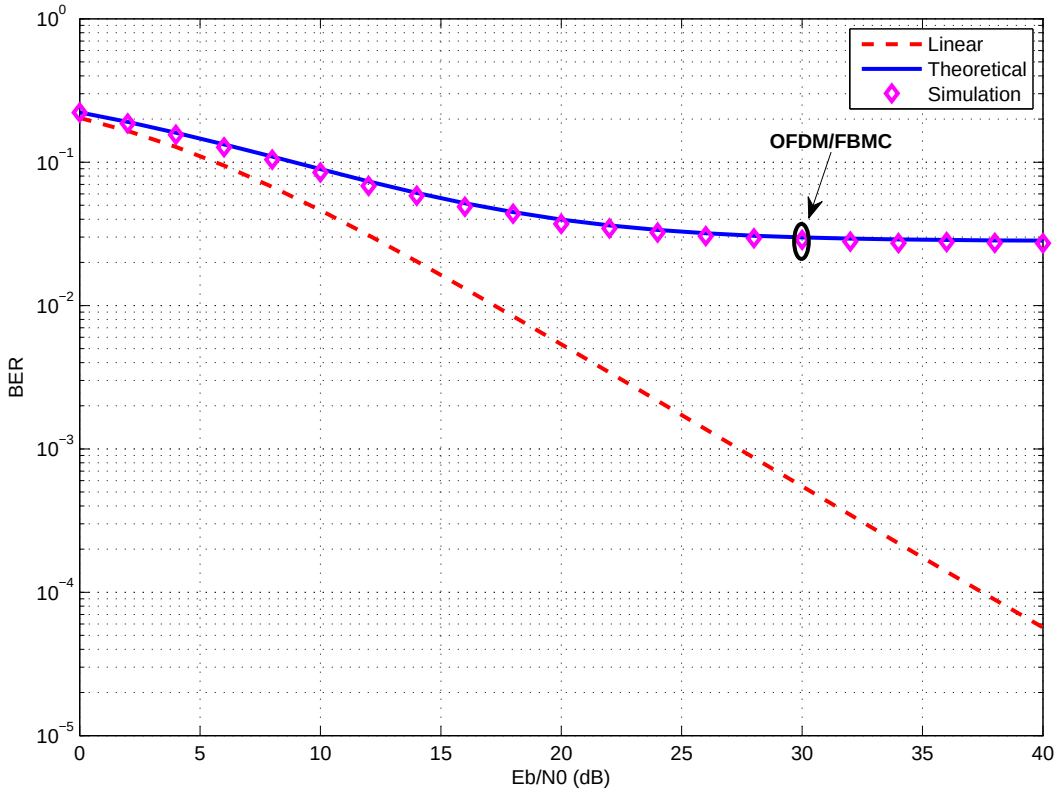


Figure 3-6: BER vs $\boldsymbol{Eb/N0}$ for OFDM and FBMC system. Saleh HPA model, 64 subcarriers, 16QAM, $\varphi_0 = \pi/3$, IBO $= 6$ dB, and Rayleigh channel.

Based on equation 3.44 and simulation results shown in figure 3-6, we note that the BER, for relatively low E_b/N_0 (i.e., $E_b/\sigma_w^2 < 2$ dB), is very close to the BER performance of the Rayleigh channel with a linear HPA. This phenomenon is due to the fact that the residual degradation of the BER, which is caused by the NL HPA, is negligible compared to the AWGN interference (i.e., $\sigma_d \ll \sigma_w$). Indeed, the SNR, given by equation 3.42, has the same distribution as the Rayleigh one. At high values of E_b/N_0 (i.e., $E_b/\sigma_w^2 > 30$ dB), σ_w is negligible and the SNR tends to a constant ($\gamma \to \frac{E_b}{\sigma_d^2}$), leading then to a constant BER, as shown by figure 3-6.

3.7 Conclusion

In this chapter, we have studied the impact of in-band NL distortions caused by memoryless HPA on both OFDM and FBMC systems. This study is valid for any measured or modeled memoryless HPA, exhibiting AM/AM, AM/PM and for any multicarrier modulated signal provided that this signal is Gaussian. A theoretical approach was proposed to evaluate the BER performance for both OFDM and FBMC systems. This approach is based on modeling the in-band NL distortion with a complex gain and an uncorrelated additive Gaussian noise, given by Bussgang's theorem. The theoretical determination of the NLD parameters is related to the HPA model used. For simple HPA models, the analytical expressions for the NLD parameters can be easily established. However, for more complicated HPA models exhibiting amplitude and phase distortions, the task is more complicated. The idea proposed here is based on polynomial approximation of any HPA

model at sufficient order. This makes possible the theoretical analysis for any measured or modeled HPA.

This study can be easily expandable to HPA models with memory. Indeed, in this case, one could apply the memory filter of the Hammerstein HPA model (section 2.4) in order to compute analytically the NL parameters at the output of that filter. These parameters can then be used in order to compute the BER of both OFDM and FBMC systems in presence of NL HPA models showing memory effects.

When the NL parameter K is compensated for at receiver side, OFDM and FBMC show the same performances in terms of BER. Simulations and theoretical results are shown to be in agreement for various IBO values.

4. Impact of nonlinearities on out-of-band distortion

4.1 Introduction

FBMC has extremely concentrated frequency localization unlike OFDM. For instance, prototype functions with extremely concentrated frequency localization can be designed such that the out-of-band emissions become negligible. FBMC systems does not need Cyclic Prefix (CP). In addition to that, phase noise and frequency offset does not significantly affect its performance [26]. However like any other multi-carrier technique, FBMC suffers from high PAPR because of which there comes a need to opt for PAPR reduction techniques. The good frequency localization property is compromised when realistic radio-frequency impairments are taken into account; as shown in [27]. Indeed, the spectral regrowth of FBMC and OFDM is very similar when the HPA distorts the transmitted waveform. HPAs are important element in communication systems and are inherently NL. There are two popular methods for spectral regrowth analysis, where we can derive a closed-form expression for the auto-covariance function of the HPA output, whose Fourier Transform (FT) yields the output Power Spectral Density (PSD). The first method is based on cumulants [28] and the later one is based on Price's theorem [29]. However since the latter involves integral calculus, it may sometime involve difficulty in determining the integration constant which will impact the closed-form expression derivation. Analysis of the NL spectral regrowth in FBMC systems for cognitive radio context using Price theorem has already been done in [30], where only AM/AM distortion has been taken into consideration. In a scenario where AM/PM distortion is to be taken into account, it becomes complicated to predict the PSD using the Price theorem. Due to these two reasons, the cumulant-based method seems to be more adequate for PSD prediction.

In this report, the HPA is considered to be memoryless. Once the HPA model is known i.e. its AM/AM and AM/PM distortion characteristics are available (known model or measurements) then we can do polynomial approximation for those characteristics. In order to derive a closed-form expression based on cumulants, we need the coefficients of the polynomial. The model for HPA used in this chapter is based on Saleh's model [4]. However, the study remains valid for any other HPA model. Already, the spectral regrowth prediction for OFDM systems based on cumulants was done by G. T. Zhou [31] and the work done in this chapter is an extension to FBMC systems. It's also important to underline that this study can be expandable to HPA models showing memory effects such as those introduced in section 2.4.

4.2 Theoretical study for spectral regrowth using cumulants

4.2.1 Introduction of cumulants

Cumulants are used generally for derivation of closed-form expressions. Because of their interesting properties they are used as an alternative to the moments of the distribution. Cumulants were first introduced by Thorvald N. Thiele, who called them as $semi\text{-}invariants$ [32]. They were first called $cumulants$ in a paper by Ronald Fisher and John Wishart [33].

4.2.2 Cumulants definition

The n^{th} order cumulant c_n of a random variable $x(t)$ is defined as

$$c_n = \frac{\partial^n}{\partial t^n} g(t)\bigg|_{t=0} \tag{4.1}$$

where $g(t)$ is called as cumulant generating function given by

$$g(t) = log(\mathbb{E}(e^{tx(t)})) = \sum_{n=1}^{\infty} c_n \frac{t^n}{n!} \tag{4.2}$$

where $\mathbb{E}(.)$ is the expectation operator. The cumulant-generating function $g(t)$ is the logarithm of the moment-generating function (MGF) $\mathbb{E}(e^{tx(t)})$.

4.2.3 The cumulant/moment relation

Cumulants are related to moments by the following recursion formula:

$$c_n = \mathbb{E}(x(t)^n) - \binom{n-1}{m-1}.c_m.\mathbb{E}(x(t)^{n-m}) \tag{4.3}$$
$$\binom{n}{m} = \frac{n!}{(n-m)!.m!} \ , \ n \geq m$$

where $\mathbb{E}(x(t)^n)$ is the n^{th} classical moment (*raw moment*). The above relation implies that c_n is a n^{th} degree polynomial containing the first n raw moments. As as example, we can write:

$$c_1 = \mathbb{E}(x(t)) \tag{4.4}$$
$$c_2 = \mathbb{E}(x(t)^2) - [\mathbb{E}(x(t))]^2 \tag{4.5}$$
$$c_3 = \mathbb{E}(x(t)^3) - \mathbb{E}(x(t)^2)\mathbb{E}(x(t)) + 2[\mathbb{E}(x(t))]^3 \tag{4.6}$$

The classical moments can also be expressed in terms of cumulants as shown below,

$$\mathbb{E}(x(t)) \ = c_1 \tag{4.7}$$
$$\mathbb{E}(x(t)^2) = c_2 + c_1^2 \tag{4.8}$$
$$\mathbb{E}(x(t)^3) = c_3 + c_2 c_1 - c_1^3 \tag{4.9}$$

4.2.4 Cumulants and set-partitions

It is evident from (4.7), (4.8) and (4.9), that $\mathbb{E}(x(t)^n)$ is a linear combination of products of c_m's where $n \geq m$ and $n, m \in \mathbb{R}$ as given below

$$\mathbb{E}(x(t)^n) = \sum_{\pi} \prod_{B \in \pi} c_{|B|} \tag{4.10}$$

where

- π runs through the list of all partitions of a set of size n,
- "$B \in \pi$" means B is one of the "blocks" into which the set is partitioned; and,
- $|B|$ is the size of the set B.

The polynomial (4.10) has striking *combinatorial interpretation*, since the coefficients in these polynomials count for certain *partition of sets* and are precisely same as the coefficients in the polynomial of Faa di Bruno's formula [34].

Based on partition of sets, for any order moment, we can write expression in terms of cumulants. A set with n elements can be partitioned in B_n ways. where B_n is the n^{th} Bell number. Bell numbers satisfy a recurrence relation involving binomial coefficients.

$$B_{n+1} = \sum_{k=0}^{n} \binom{n}{k} B_n \tag{4.11}$$

where, $B_0 = B_1 = 1$ and first few Bell numbers are 1,1,3,5,15,152,....

In order to find polynomial expression for 3^{rd} order moment as per (4.10), we find different ways. One can partition a set of 3 elements. We represent each way as a list of partitioned sets. 3 elements can be partitioned into three partition sets such as, one sub-set of 3 elements (i.e. no partition at all or $|\pi| = 1$) or two sub-sets of 1 and 2 elements each (i.e. one partition or $|\pi| = 2$) or three distinct sub-sets of 1 element each (i.e. three partitions or $|\pi| = 3$). The number of elements in each sub-set will be the order of the cumulant and such cumulant formed from each sub-set in the list should be multiplied (e.g. in a partition list of two sub-sets of 1 and 2 elements each, we write as $3c_1c_3$. The factor 3 is the number of occurrence of such a partition list with $|\pi| = 2$). For example, let us consider A, B and C are three identical random variables in a sample space $\mathcal{S}$. So, they are the elements in the set $\mathcal{S}$. Then the possible *additive partition* of these 3 random variables is shown below,

$|\pi| = 1 \ \rightarrow [ABC] \Rightarrow 1 \times c_3$ one possible occurance
$|\pi| = 2 \ \rightarrow [A, BC],\ [AB, C]$ and $[AC, B] \Rightarrow 3 \times c_1c_2$ three possible occurances
$|\pi| = 3 \ \rightarrow [A, B, C] \Rightarrow 1 \times c_1^3$ one occurance

The **joint cumulant** of several random variables $X_1, X_2, ..., X_n$ can be defined, based on (4.2), in terms of raw moments as,

$$c(X_1, X_2, ..., X_n) = \sum_{\pi} (|\pi| - 1)!(-1)^{|\pi|-1} \prod_{B \in \pi} \left[\mathbb{E}\Big(\prod_{i \in B} X_i \Big) \right] \tag{4.12}$$

For example, let us consider X, Y and Z are three random variables in a sample space. Then the possible *additive partition* of these 3 random variables are illustrated in the Fig. 4-1 as given below,

$|\pi| = 1 \ \rightarrow [XYZ]$
$|\pi| = 2 \ \rightarrow [X, YZ],\ [XY, Z]$ and $[XZ, Y]$
$|\pi| = 3 \ \rightarrow [X, Y, Z]$

So, the joint cumulant for 3 random variables is given as

$$c(X, Y, Z) = \mathbb{E}(XYZ) - \mathbb{E}(XY)\mathbb{E}(Z) - \mathbb{E}(XZ)\mathbb{E}(Y) - \mathbb{E}(YZ)\mathbb{E}(X) + 2\mathbb{E}(X)\mathbb{E}(Y)\mathbb{E}(Z) \tag{4.13}$$

The joint cumulant of just one random variable is its *expected value* and that of two random variables is their *covariance*. If some of the random variables are independent of all of the others, then any cumulant involving two (or more) independent random variables is zero. If all

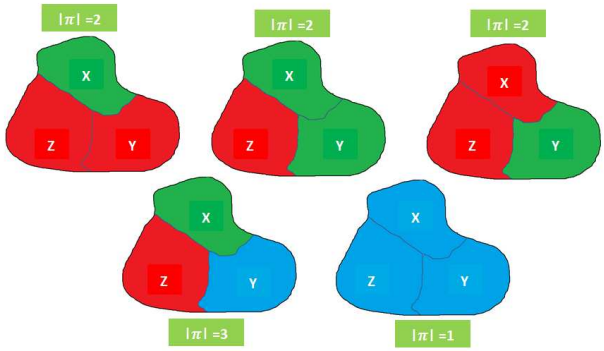


Figure 4-1: Illustration of *additive partition* of 3.

n random variables are the same, then the joint cumulant is the n^{th} order cumulant.

If $x(t)$ is a random process then we denote its k^{th} order cumulant as

$$c_{kx}(\boldsymbol{\tau}) = cum\{x(t), x(t+\tau_1), ...x(t+\tau_{k-1})\} \tag{4.14}$$

where $\boldsymbol{\tau} = (\tau_1, \tau_2, ..., \tau_{k-1})$.

4.2.5 Properties of cumulants

The cumulant generating function $g(t)$, if it exists, is *infinitely differentiable* and *convex*, and passes through the origin. The cumulant-generating function $g(t)$ exists if and only if the tails of the distribution are majorized by an *exponential decay*. Some properties of the cumulants are given below [33],

Invariance and equivalence: For a random variable X, the first cumulant is shift-equivariant and all of the others are shift-invariant,

$$c_n(X+a) = \begin{cases} c_n(X) + a & n = 1 \ \{\textit{shift-equivariant}\} \\ c_n(X) & n \geq 2 \ \{\textit{shift-invariant}\} \end{cases} \tag{4.15}$$

Because of the above property, the cumulants were initially named as *semi-invariants*.

Homogeneity: The n^{th} cumulant of a random variable X is homogeneous of degree n

$$c_n(aX) = a^n c_n(X) \tag{4.16}$$

where a is a real constant.

Additivity: If X and Y are two independent random variables then their n^{th} cumulants accumulate,

$$c_n(X+Y) = c_n(X) + c_n(Y) \tag{4.17}$$

The above property is the reason for name *cumulants*.

4.2.5.1 Special cases

Gaussian case: If $x(t)$ is a Gaussian random variable with mean μ and variance σ^2, then

$$c_{1x}(0) = \mu, c_{2x}(0) = \sigma^2 - \mu^2 \; and \; c_{kx}(0) = 0 \; for \; k \geq 3$$

i.i.d case: If $x(t)$ is an i.i.d. process then its k^{th} order cumulant is given by

$$c_{kx}(\boldsymbol{\tau}) = c_{kx}(0).\delta(\boldsymbol{\tau}), \forall k, \forall \boldsymbol{\tau}$$

where δ is the Kronecker delta.

Symmetrical case: If $x(t)$ has a symmetrical distribution with a zero-mean then

$$c_{kx}(\boldsymbol{\tau}) = 0, \forall k \text{ odd}, \forall \boldsymbol{\tau}$$

4.2.6 Polynomial approximation of HPA Characteristics

We recall that $i(t)$ and $u(t)$ are the base-band equivalent for the HPA input and output signals respectively (figure 3-1). For any measured or modeled HPA, we can approximate its input output conversion characteristics by a NL polynomial as

$$\begin{aligned} u(t) &= \sum_{k=0}^{M} a_{2k+1}[i(t)]^{k+1}[i^*(t)]^k \\ &= i(t)\sum_{k=0}^{M} a_{2k+1}|i(t)|^{2k} \\ &= \left[\sum_{k=0}^{M} a_{2k+1}|i(t)|^{2k+1}\right] e^{j\varphi(t))} \end{aligned} \tag{4.18}$$

where,

- $2M+1$ is the order of the polynomial model,
- a_{2k+1} are the complex coefficients of the polynomial model, and,
- $\varphi(t)$ is the phase of the input signal.

In (4.18), only the odd order harmonics are taken into account by the polynomial fitting process [35]. In [36], this approximation was compared to full ranking polynomial and the conclusion is that both approaches give the same performance in terms of base-band modeling of HPA nonlinearity. In this report we performed polynomial approximation based on least-squares algorithm.

4.2.6.1 Spectral prediction using polynomial approximation

For high number of sub-carriers, we can assume the FBMC signal to a Gaussian process as evident from Central limit theorem. If $x(t)$ is zero-mean, Gaussian and i.i.d the auto-covariance

function of the HPA output $y(t)$ same as its auto-correlation function which can be written as

$$\begin{aligned}
&c_{2u}(\tau) = cum\{u(t), u^*(t+\tau)\}\rangle \\
&= \mathbb{E}\{u(t)u^*(t+\tau)\} \\
&= \sum_{k=0}^{M}\sum_{l=0}^{M} a_{2k+1}.a^*_{2l+1}.\mathbb{E}\{[i(t)]^{k+1}[i^*(t)]^k[i^*(t+\tau)]^{l+1}[i(t+\tau)]^l\} \\
&= \sum_{k=0}^{M} |a_{2k+1}|^2.cum\{[i(t)]^{k+1}[i^*(t)]^k, [i^*(t+\tau)]^{k+1}[i(t+\tau)]^k\} \\
&+ \sum_{\substack{k,l=0 \\ k\neq l}}^{M} a_{2k+1}.a^*_{2l+1}.cum\{[i(t)]^{k+1}[i^*(t)]^k, [i^*(t+\tau)]^{l+1}[i(t+\tau)]^l\} \\
&= \sum_{k=0}^{M} |a_{2k+1}|^2.c_{(2k+1)(2k+1)}(\tau) + \sum_{\substack{k,l=0 \\ k\neq l}}^{M} a_{2k+1}.a^*_{2l+1}.c_{(2k+1)(2l+1)}(\tau)
\end{aligned} \tag{4.19}$$

In this work, we consider the cumulants as the higher-order generalization of covariance functions and are used as a tool to derive closed-form expression for $c_{2u}(\tau)$. According to [31], the auto-correlation function for a $(2M+1)^{th}$ polynomial order nonlinearity is given as

$$c_{2u}(\tau) = \sum_{m=0}^{M} \beta_{2m+1}|c_{2i}(\tau)|^{2m}c_{2i}(\tau) \tag{4.20}$$

where the constant coefficient β_{2m+1} is given as

$$\beta_{2m+1} = \frac{1}{m+1}\left|\sum_{k=m}^{M} a_{2k+1}\binom{k}{m}(k+1)![c_{2i}(0)]^{2m}\right|^2 \tag{4.21}$$

The Fourier transform of $c_{2u}(\tau)$ yields the PSD of the amplified signal $S_u(f)$ and is given by

$$S_u(f) = \int_{-\infty}^{+\infty} c_{2u}(\tau)e^{-j2\pi f\tau}d\tau \tag{4.22}$$

Once we are able to model the HPA (i.e. obtain the AM/AM and AM/PM distortion measurements) then we can pre-calculate the complex coefficients a_{2k+1} from polynomial approximation. The input auto-correlation function $c_{2i}(\tau)$ can be calculated based on analytical PSD of an FBMC signal from the equation (5.22). This facilitates us to predict the spectral regrowth of an amplified FBMC signal.

4.2.7 HPA modeling and spectral regrowth prediction

4.2.7.1 Modeling of the HPA

In section 2.2, equation 2.4, we had written the amplified signal as

$$u(t) = S(\rho(t))\exp(j\varphi(t)) \tag{4.23}$$

where, $S(\rho(t)) = F_a(\rho(t))\exp(jF_p(\rho(t)))$ is the complex soft envelop of $u(t)$. $F_a(\rho(t))$ and $F_p(\rho(t))$ are the AM/AM and the AM/PM distortion characteristics of the HPA respectively. Once these characteristics are known, we can do polynomial approximation of $S(\rho(t))$.

In this work, the AM/AM and AM/PM characteristics are based on polynomial fitting of Saleh's HPA model. It is worth noting that PSD computation using cumulants can be applied to any model of HPA. The AM/AM and AM/PM characteristics of Saleh's HPA model is given by [4] The AM/AM and AM/PM characteristics of Saleh's HPA model (equation 2.10), with $\varphi_o = \pi/3$ and A_{sat}, are given in figure 4-2 and figure 4-3. In these figures, we also plot the distortion characteristics obtained after polynomial fitting with polynomials of order 3, 7, 11 and 15 respectively.

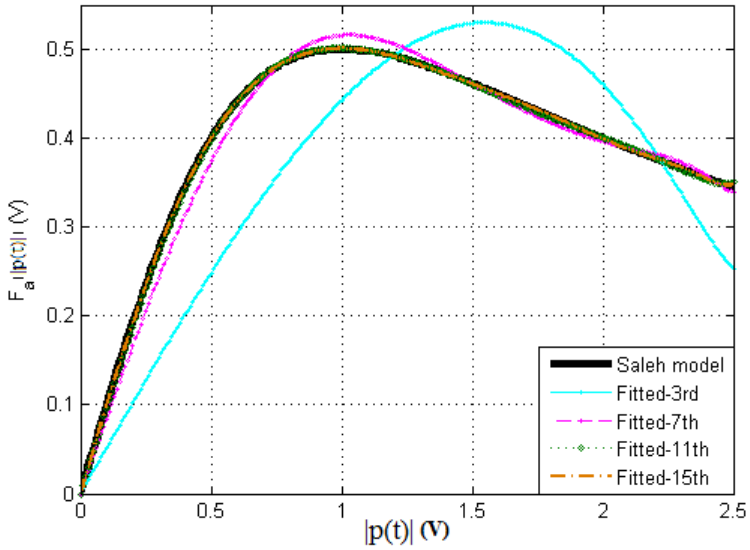


Figure 4-2: AM/AM distortion - Saleh Model and its polynomial fitting of orders 3, 7 , 11 and 15.

4.2.8 Simulation results for PSD prediction

Simulation is done for 1000 FBMC symbols with 128 total Sub-carriers. PHYDYAS prototype filter was used. Nonlinearity polynomial orders chosen were 3, 7, 11 and 15 with different IBO values. We recall that IBO of HPA is defined as the ratio between the 1dB compression point input-referred power and the input signal average power.

In the legends of the PSD plots, 'Input' is the FBMC signal input PSD, 'Output-Simu' is the simulated PSD based on HPA model, 'Output-Poly-3rd', 'Output-Poly-7th', 'Output-Poly-11th' and 'Output-Poly-15th' are the simulated output PSDs based on polynomial approximation with 3^{rd}, 7^{th}, 11^{th} and 15^{th} order nonlinearity respectively (i.e. the HPA model is the polynomial approximated model and the spectral regrowth is the simulated corresponding PSD). Similarly, 'Output-Cumul-3rd', 'Output-Cumul-7th', 'Output-Cumul-11th' and 'Output-Cumul-15th' are the analytical PSDs calculated using cumulants for respective polynomial approximations for different orders of nonlinearity. Figure 4-4 and figure 4-5 present the simulations results done with IBO values 1 and 3dB having 10 active sub-carriers each. We can observe that with IBO

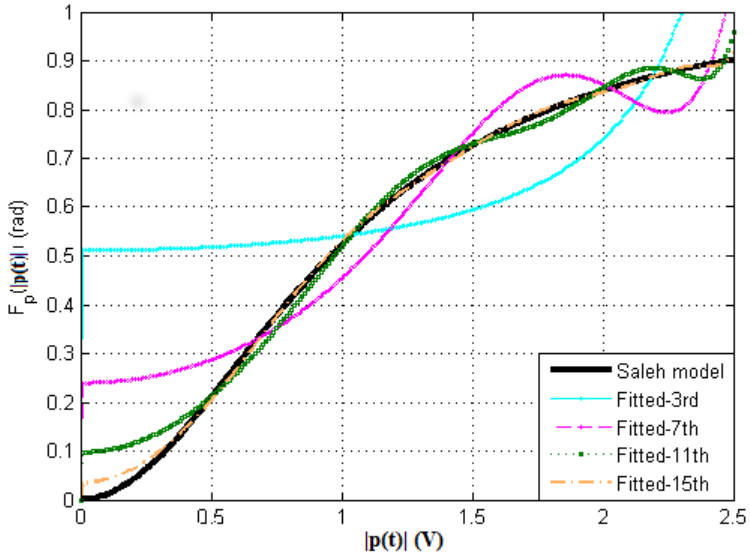


Figure 4-3: AM/PM distortion - Saleh Model and its polynomial fitting of orders 3, 7 , 11 and 15.

of 3dB the 11^{th} order polynomial gives result very close to simulated PSD, while for IBO of 1dB it is necessary to take the 15^{th} order polynomial fitting to have a similar performancebehaviour.

We have shown the simulation results for PSD prediction when 3 users share neighboring

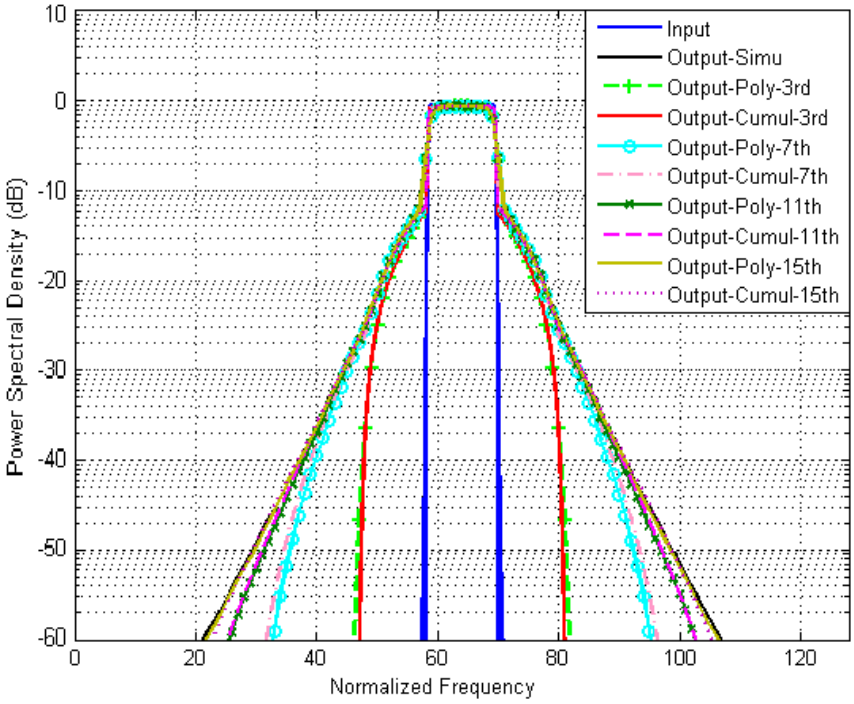


Figure 4-4: PSD Prediction with IBO=1dB.

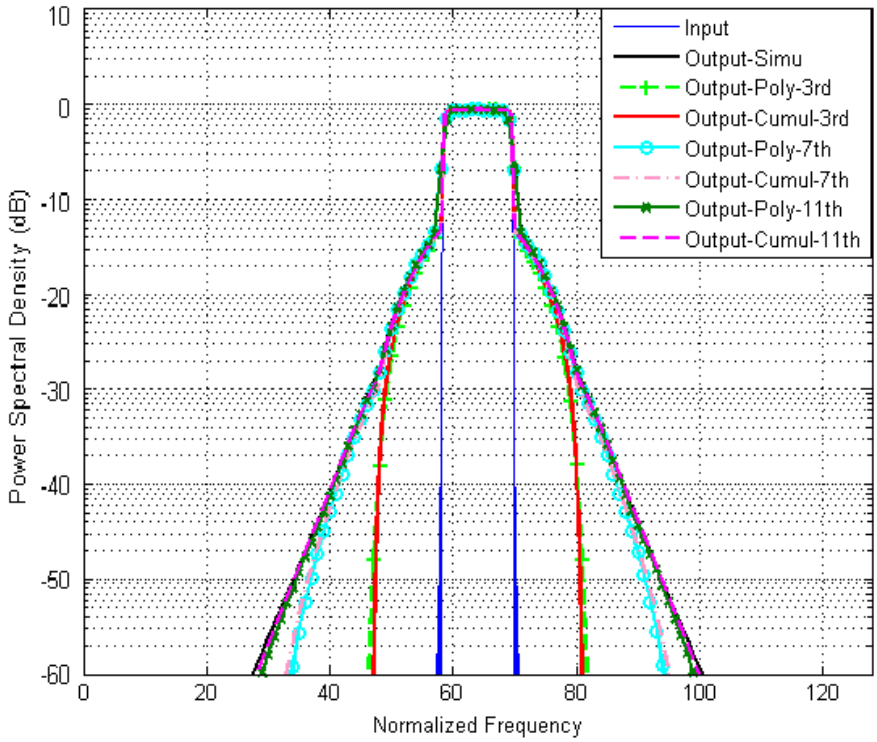


Figure 4-5: PSD Prediction with IBO=3dB.

sub-carriers in figure. 4-6. This scenario is of interest in a CR context when multiple primary users can occupy the spectrum. In this case, we will consider three users operating on closely spaced sub-bands. The three signals are amplified at an IBO of 1dB. The details of active sub-bands for the three users are given below,

- User 1: 30^{th} to 40^{th} sub-carrier,
- User 2: 45^{th} to 50^{th} sub-carrier,
- User 2: 52^{nd} to 57^{th} sub-carrier,

In this scenario, we can notice that despite operating the HPA at an IBO=1dB, the prediction of the PSD is well achieved up to -20dB, -25dB and -33dB with polynomial fittings of orders 3^{rd}, 7^{th} and 11^{th} respectively. The reason for choosing thinner sub-bands for the three users is because that when the band of active sub-carriers tends to be thinner, we need higher-order polynomial fitting to predict the output PSD accurately.

4.3 Evaluation of uniform and non-uniform FBMC in presence of HPA nonlionearities

Starting from the time-frequency duality between standard OFDM formats and Time-Limited Orthogonal) (TLO multi-carrier formats), in D2.1 we introduced uniform (even-and odd-spaced) FBMC-FLO (Frequency-Limited Orthogonal) and FBMC-TLO configurations. The FLO and the TLO respectively denote the FBMC options with the frequency-domain (commonly known

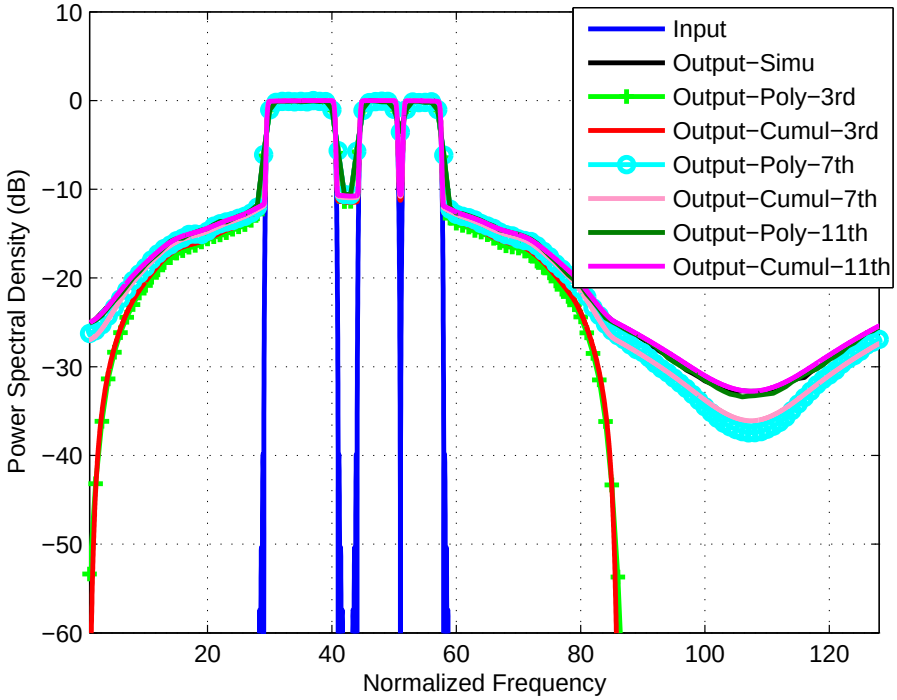


Figure 4-6: PSD Prediction with IBO=1dB (3 different active Sub-bands).

form) and the time-domain limited signaling elements in subchannels. Besides the advantages of the I/Q staggered multi-carrier formats over the conventional CP-OFDM one regarding the CP-related spectral efficiency reduction and the robustness to co-channel interference of the former (D3.2), they allow use of relatively small number of subchannels to span a particular transmission channel bandwidth, reducing by that - and by additional shortening of the referent impulse response (as in the TLO case) - the PAPR to attain a reduced impact of NL amplification to out-of-band spectral leakage. We then used these as a basis for extension towards non-equal bandwidth and non-uniformly frequency-domain positioned subchannels - Nu-FBMC-FLO and the Nu-FBMC-TLO configurations, in order to harmonize the advantages of using wider subchannels in terms of reduction of PAPR and the increase of spectral efficiency in situations when predetermined PSD masks have to be obeyed. Besides, to primarily allow for multiplexing of unequally wide subchannels FBMC waveforms belonging to different users without the need for introduction of the frequency guard-bands in the Down-Link (DL) direction of transmission, we also came up with the use of the asymmetrical roll-off factors (in frequency-domain), which partly also contribute to somewhat reduced lengths of the related subchannels impulse response, and thus to a reduced adjacent channels/users interference. In this section we provide computer simulation-based comparative evaluation of these multi-carrier formats with the conventional OFDM modulation under presence of HPA modeled by Rapp output-to-input relationship [3]. The comparison criterion is the attainable spectral efficiency while still fitting the 1.4 MHz LTE Up-Link (UL) power spectral density (PSD) mask. The power efficiency will be accounted for through conventional IBO.

4.3.1 Evaluated uniform and non-uniform FLO and TLO multi-carrier waveforms

In the following we provide base-band time and frequency domain description of the multicarrier waveforms to be evaluated. The goal is to set the reference for the designations in the PSD figures and the measure of basic spectral efficiency. It will also serve as guidance regarding the number of subchannels used and their mutual relationships. The OFDM signal is not represented in these illustrations, and it is only characterized by maximal number of subchannels (128) and the number of active subchannels.

The plots shown in figure 4-7 illustrate the spectral arrangement of subchannels in the cases of uniform FBMC configuration and symmetrical non-uniform (Nu) FBMC configuration for FLO format and their corresponding time-domain representations. The uniform configuration shown in figure 4-7-a) is given for 100% roll-off factor. Roll-off factors of subchannels in non-uniform symmetrical arrangement are 100%, 50%, 25%, 25%, 12.5% and 6.25%, respectively starting from the narrowest (the rightmost) subchannel to central (DC) subchannel, as shown in figure 4-7-c).

Figure 4-8 illustrates the spectral arrangement of subchannels for the asymmetrical non-uniform FBMC configuration and the corresponding time-domain impulse response representation. In the case of asymmetrical arrangement the subchannels are characterized with two roll-off factors. The chosen notation $x\%$-$y\%$ denotes roll-off factor of right edge of subchannel - roll-off factor of left edge of subchannel. The used roll-off factors for subchannels in asymmetrical arrangement are $100\% - 100\%$, $100\% - 50\%$, $50\% - 25\%$, $25\% - 25\%$, $25\% - 12.5\%$, $12.5\% - 12.5\%$ respectively starting from the narrowest (the rightmost) subchannel to central (DC) subchannel figure 4-8-a).

In figure 4-9-a) and figure 4-9-b) are depicted the spectrum representation and corresponding referent impulse response in the case of uniform FBMC arrangement for TLO format. The TLO format represents the frequency-time dual form of the FLO format [37]. The uniform FBMC arrangement for TLO format is formed by positioning subchannels at the same central frequencies as for FLO format, also for 100% roll-off factor (defined in time-domain). For the non-uniform TLO formats the aggregation is performed at corresponding (time-domain) referent impulse responses. Their frequency-domain representations are then subsequently produced and appropriately positioned as in the case of the Nu-FBMC counterpart. Spectrum of the even non-uniform TLO FBMC arrangement and his corresponding time-domain representation, are shown in figure 4-9-c) and figure 4-9-d). Notice that the central frequencies are same as in the case of FLO Nu-FBMC arrangements depicted in figure 4-7-c) and figure 4-8-a). Roll-off factors defined in time-domain, are 100%, 50%, 25%, 25%, 12.5% and 6.25% respectively, starting from the narrowest (black) subchannel to the widest (cyan) subchannel (figure 4-9-d)).

4.3.2 Spectral efficiency with HPA

The Rapp HPA model [3] has been used in evaluation of PSD mask fitting and related spectral efficiencies (not accounting for the impact of CP in the LTE case).

Figure 4-10-a) shows comparison between conventional OFDM, uniform FLO and uniform TLO configurations in the context of sensitivity to the NL HPA amplification. The same comparison is given in the figure 4-10-b) for Nu symmetrical FLO, Nu asymmetrical FLO and Nu TLO configurations. In order to satisfy Emphatic framework for demonstrator we used LTE UE 1.4 MHz mask [38]. The Rapp HPA model with parameter $p = 2.5$ is used to model NL distortions. For all simulated cases oversampling factor 5:1 is used.

In figure 4-10-a), PSDs are given for undistorted and distorted OFDM with 72 active out of 128 subchannels (56.25% of spectral efficiency, including four pilots), uniform FLO FBMC

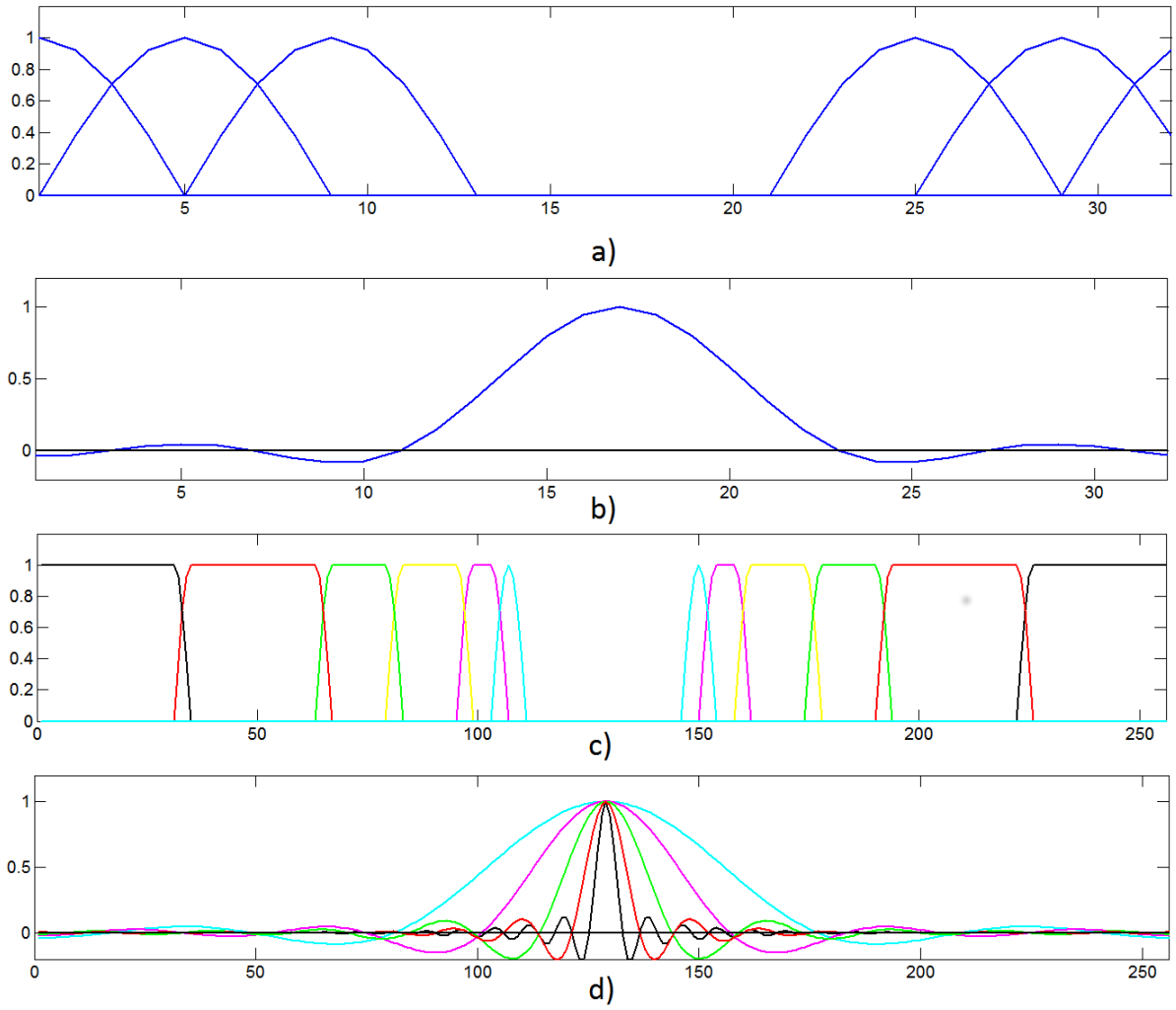


Figure 4-7: FLO uniform arrangement spectra (a) and corresponding (low-pass) time-domain representations (b), FLO Nu-FBMC arrangement with symmetrical spectra (c) and corresponding (low-pass) time-domain representations (d) - all without oversamling.

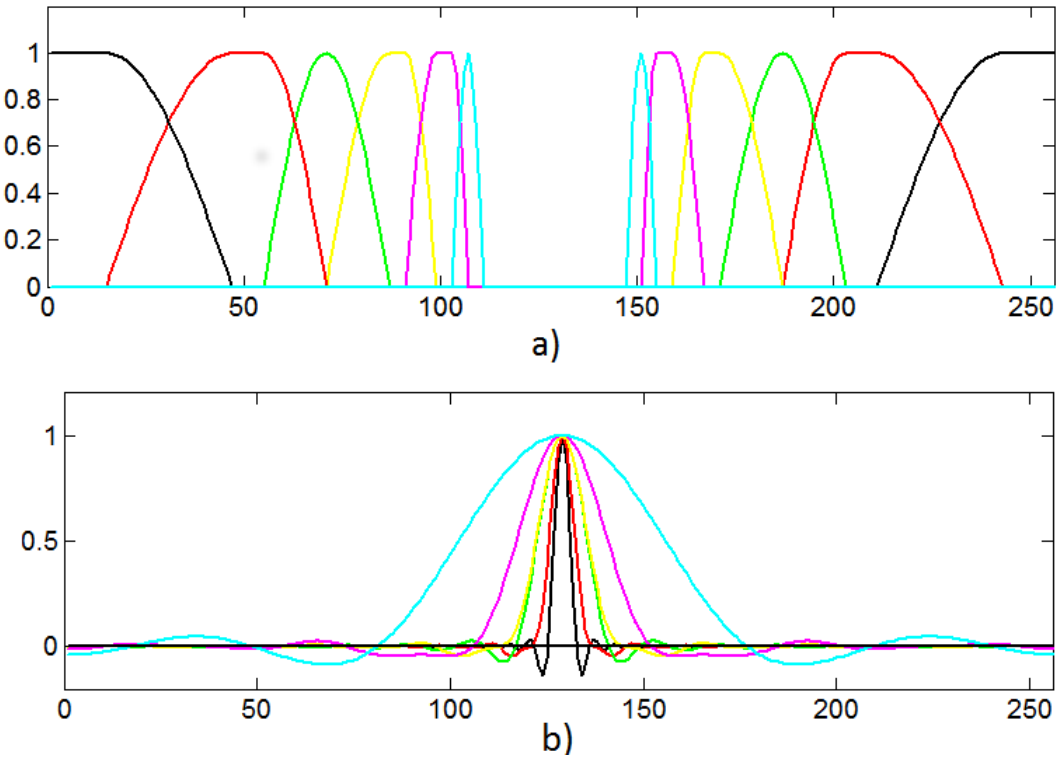


Figure 4-8: FLO Nu-FBMC arrangement with asymmetrical spectra (a) and corresponding time-domain representations (b) - all without oversampling.

with 5 out of 8 subchannels, and uniform TLO FBMC, also with 5 out of 8 subchannels, which corresponds to spectrum usage of 62.5%. Corresponding Nu-FBMC arrangements are depicted in figure 4-7-a) and figure 4-9-a), respectively.

All Nu configurations are formed by aggregation of 54 out of 64 uniformly-spaced subchannels (84.4% of spectral efficiency) which gives 11 Nu subchannels (both subchannels at negative and positive frequencies). Corresponding Nu-FBMC arrangements are depicted in figure 4-7-c), figure 4-8-a) and figure 4-9-c), respectively and their PSDs are given in the figure 4-10-b). The ability of Nu arrangements for significantly improved spectral efficiency in presence of the HPA induced NLs has been demonstrated by this and that was the motivation for its development within D3.1.

From figure 4-10-a) it can be seen that the uniform FLO configuration provides slightly less out-of-band leakage in comparison with OFDM and therefore causes less interference allowing better utilization of gaps in the spectrum. The uniform TLO configuration has similar behavior as OFDM in the beginning out-of-band range. With this configuration TLO also fits to mask and has slightly worse out-of-band leakage than FLO. However, the uniformly-spaced FBMC configurations provide better PSD mask fitting although they have approximatively 6.25% better spectral efficiency than OFDM.

From figure 4-10-b) it can be seen that the Nu FBMC configurations have better spectral and PSD mask fitting features than the corresponding uniform FBMC configurations (from which they were derived). At the same time non-uniform configurations provide the higher spectral efficiency of 84.4%. Also, it can be seen that the asymmetrical FBMC FLO configuration is just slightly better than the symmetrical one in the context of reducing spectral spread-out.

From the figure 4-10-a) it can be noticed that HPA model allows aggregation of more

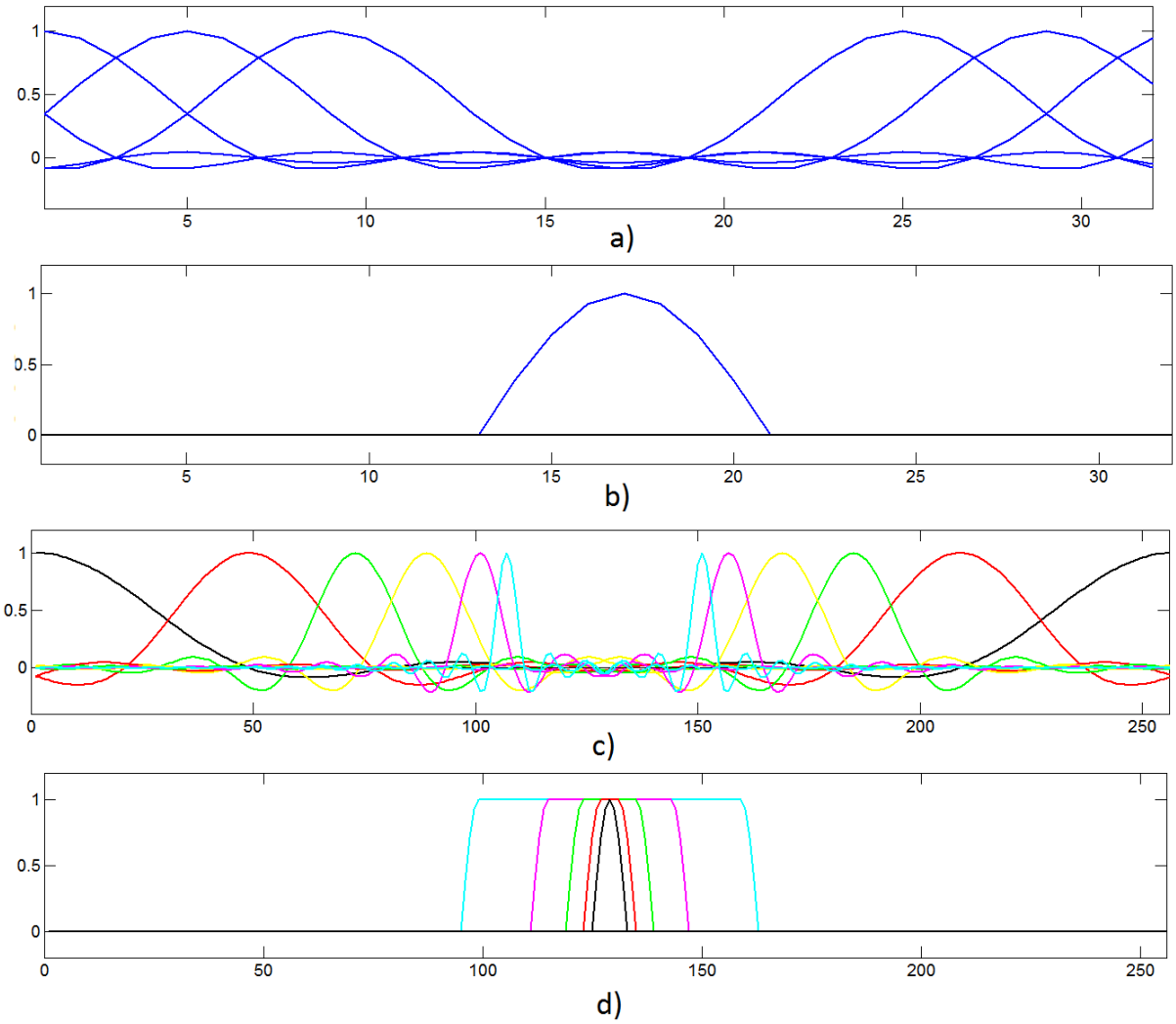


Figure 4-9: TLO uniform-FBMC arrangement (a) and his corresponding time-domain representation (b), TLO Nu-FBMC arrangement (c) and his corresponding time-domain representation (d), (without oversampling).

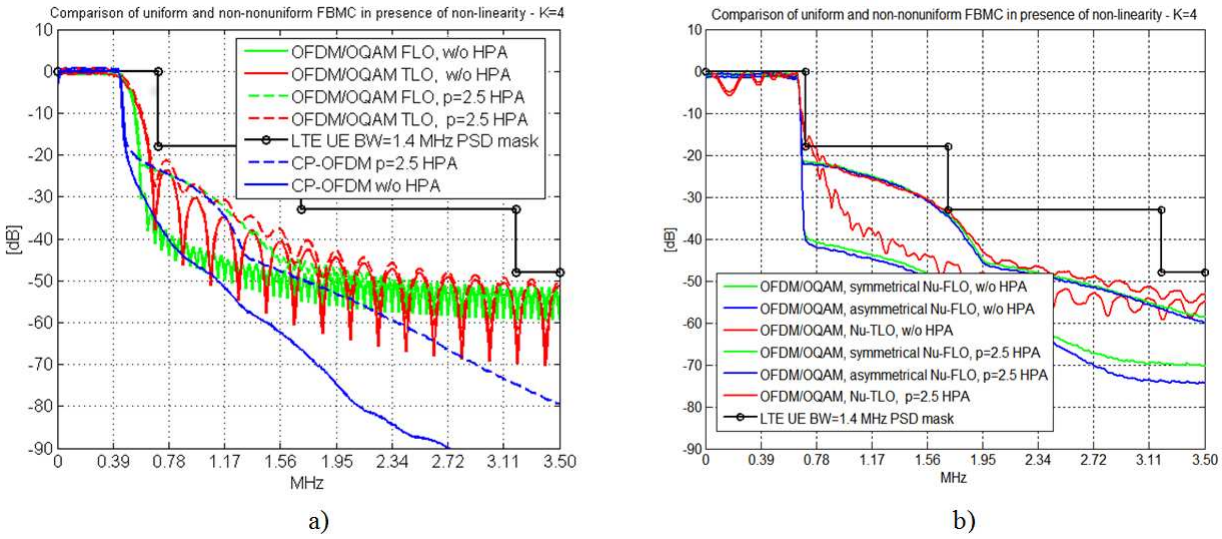


Figure 4-10: (a) Comparison of conventional OFDM, uniform FLO FBMC and uniform TLO FBMC, and (b) comparison of symmetrical Nu-FLO FBMC, asymmetrical Nu-FLO FBMC and Nu-TLO FBMC in context of HPA and mask fitting.

subchannels for OFDM (although standard defines 72 active out of 128 subchannels) as well as in the case uniform-spaced FLO configuration. Thus, figure 4-11 compares OFDM and uniformly-spaced FLO configuration in configuration that provides the maximum fitting of used LTE mask. For that purpose OFDM uses 100 active out of 128 subchannels (78.1% of spectral efficiency), and the uniform FLO FBMC arrangement uses 6 active out of 8 (75% of spectral efficiency).

From figure 4-11 it can be seen that FLO FBMC has less out-of-band leakage, especially in the beginning of out-of-band interval. In compared configurations, however, the spectrum utilization for OFDM is higher for 3.1% than for uniform FLO FBMC.

4.4 Conclusion

When a multi-carrier signal is amplified using a NL HPA, then it leads to spectral regrowth. Prediction of PSD in such scenario is dealt in this chapter. For the prediction of the PSD, a generalized moments formalism called cumulants was used. Cumulants are used instead of moments, as we can derive closed form expressions with much ease. With cumulants, we can compute the auto-covariance function of the amplified signal, the Fourier transform leads to the PSD including potential spectral regrowth depending on IBO. Moreover, cumulants are used for analytical computation of auto-covariance function. For this computation, a polynomial modeling of the HPA characteristics is needed. This modeling should be done at sufficiently adequate polynomial order in order fit well the conversion characteristics. When IBO is low then a high-order polynomial approximation is needed in order to predict the PSD regrowth more accurately. We underline that the prediction of the spectral regrowth is of great interest in a cognitive radio context such as that of co-existence between PMR and LTE technologies. Another task carried in this chapter was the evaluation of spectral efficiency of various multi-carrier waveforms. This evaluation has, to certain extent, demonstrated the advantage of non-uniform over uniform FBMC formats and over conventional OFDM, when it comes to

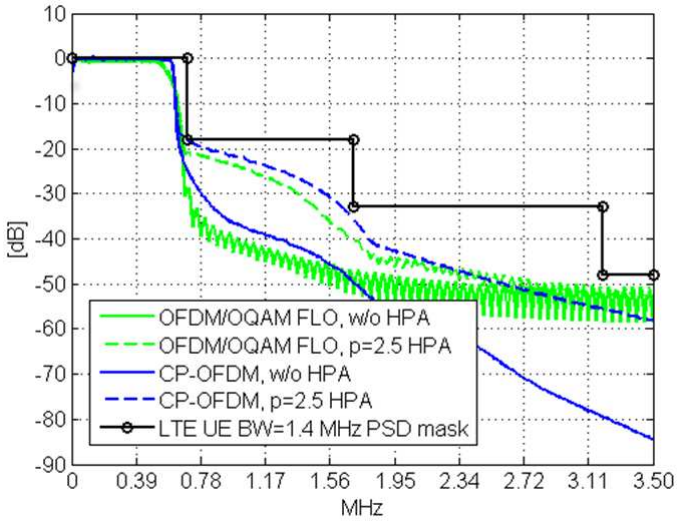


Figure 4-11: Comparison of conventional OFDM and uniform FLO FBMC for the maximum fitting of the PSD mask.

avoidance of adjacent channel interference between the up-link transmissions. This is, of course, contingent on the correctness of both the selected HPA model.

5. PAPR reduction techniques

5.1 Introduction

Being a multi-carrier technique, the FBMC system suffers from high PAPR and its frequency localization property is no longer valid in real communication systems consisting of NL HPAs leading to spectral regrowth thereby hampering much of its attractive appeal to be the ideal candidate for 5^{th} Generation (5G) Radio Access Technology (RAT) [27]. This is the imperative reason to look for better PAPR reduction techniques, so that the impact of HPA NL is dampened. The PAPR is a random variable that is an appurtenant parameter in measuring the sensitivity of a NL HPA when a non-constant envelop input need to be transmitted. Every multi-carrier modulation system have high PAPR which poses a severe challenge to the RF design of HPAs. In order to obviate distortion, the HPA is made to operate in it's linear region which means that the signal peaks should be within this region. This can be achieved by reducing the mean power of the input signal and is termed as IBO. We recall that the IBO of a HPA is defined as the ratio between the 1dB compression point input-referred power and the input signal average power. *Back-off* dampens the power efficiency of a HPA. With this constraint, a real communication system design needs a HPA that has got longer linear region. Higher IBO results on energy wastage [39]. In order to fend off this, we ought to opt for PAPR reduction techniques. The PAPR of the continuous-time base-band signal $s(t)$ transmitted during a symbol period T is defined by [40],

$$PAPR_{s(t)} = \frac{\max_{0\leq t\leq T} |s(t)|^2}{\frac{1}{T}\int_0^T |s(t)|^2.dt} \tag{5.1}$$

Generally, most of the existing PAPR reduction techniques can be implemented on discrete-time signals only despite our concern being a continuous-time FBMC signal. If we sample the signal with Nyquist rate then we may miss some peaks; so we need to perform over-sampling. Beyond an oversampling factor $L = 4$, we cannot improve further in approximating the PAPR of the continuous-time signal [41].

The Complementary Cumulative Density Function (CCDF) of PAPR is a useful parameter to analyze the PAPR which is defined as the probability that the PAPR of the discrete-time signal exceeds beyond a given threshold that is denoted by γ and thereby it can be evaluated as $Pr\{PAPR_{s[n]} \geq \gamma\}$.

5.2 State of the art on PAPR reduction techniques

5.2.1 Early applications

Originally, the need for PAPR reduction came into prevalence in some applications such as Radar (Radio Detection and Ranging) and Speech Synthesis. The Radar systems are limited by peak power, similar to that of communication systems. Likewise, the performance in speech synthesis applications is bound by peak power, since high peak signals lead to a hard sounding computer voice [42]. This characteristic is nocuous in simulating human speech. It is interesting to know that the human body has also dealt with the PAPR reduction issue in a sense that in a given audible spectrum, the human speech is not as high peaked as it could be.

5.2.2 Methods suggested for OFDM

In multi-carrier based communication systems, the PAPR reduction remains to be one of the most crucial issues that need to be solved effectively with a reasonable complexity. The severity of this issue can be seen from the 3^{rd} Generation Partnership Project (3GPP) specification for 4^{th} Generation (4G) Long Term Evolution (LTE) where in the physical layer UL, the SC-FDMA (Single Carrier-Frequency Division Multiple Access) has been chosen instead of OFDM, owing to the high PAPR of the later. This has prompted to probe for alternate modulation schemes that can replace OFDM in future communication standards.

Existing PAPR schemes of OFDM signals that are popular, include clipping [43], [44], Tone-Injection (TI) [45], Tone-Reservation (TR) [46], Active Constellation Extension (ACE) [47], Partial Transmit Sequence (PTS) [48]-[49], SeLective Mapping (SLM) [50], [51], companding transform [52], [53] and block coding [54]. Comparison of most of these aforesaid schemes can be found in [55] and [56]. In general, the PAPR reduction techniques can be broadly classified into three varieties namely *clip effect transformations (clipping), block coding techniques and probabilistic approaches (SLM, PTS)*.

5.2.3 Different methods of PAPR reduction for OFDM

5.2.3.1 Clipping

The most simplest PAPR reduction technique is clipping. In this method, the peaks of the signal $x(t)$ are clipped down whenever the peak crosses a given threshold, α_o as shown below,

$$x_c(t) = \begin{cases} x(t) & |x(t)| \leq \alpha_o, \\ \alpha_o.e^{j\angle x(t)} & |x(t)| > \alpha_o \end{cases} \tag{5.2}$$

where $\angle x(t)$ is the angle of $x(t)$.

In basic form, clipping is equivalent to the SEL HPA model. With this method, it's evident that no side information is required to transmit to the receiver since this is a straightforward PAPR reduction technique. However, the disadvantage is that there will be significant spectral regrowth especially when the value of α_o is small [57]. Generally, when clipping is used, it is necessary to filter the clipped signal in order to decrease out-of-band spectral regrowth. In addition to this, clipping an OFDM signal induces clipping noise, which in turn augments the error rate. In a sense, one can view the induced clipping noise as approximately independent additive white gaussian noise (AWGN) [58], which can lead to a simple Symbol Error Rate (SER) expression for AWGN channels. Numerous proposals have been made aiming at reducing the spectral regrowth and error rate increase due to clipping. One notable proposition is by presenting an iterative receiver design that try to negate the error rate increase induced by clipping [59].

5.2.3.2 Tone Reservation

This method was introduced by [60]. As the name suggests, some sub-carriers (tones) are reserved to isolate energy used to nullify large peaks. These reserved tones are orthogonal to the data sub-carriers and don't carry any information. The orthogonality eases the data recovery. If X is the information to be transmitted over N sub-carriers by its time-domain

OFDM signal $x(t)$. Then, instead of X, we transmit $\tilde{X}$ such that,

$$\tilde{X}[n] = \begin{cases} X[n] & n \in \Omega^{\perp}, \\ \tilde{C}[n] & n \in \Omega \end{cases} \tag{5.3}$$

where, Ω is the domain of the indices of tones and $\perp$ indicates orthogonal complement function. The reserved $\tilde{C}$ indicates the reserved tones that are chosen by following criterion,

$$\tilde{C}[n] = \underset{C[n]}{\arg} \min_{n \in \Omega} \left[\max \left| IFFT(X[n] + C[n]) \right|^2 \right] \tag{5.4}$$

Actually it is difficult to solve the above equation even though the problem appears to be simple. Nevertheless, it is solvable since it is nothing but a minimization over convex (quadratic) constraints, which was well studied in [61]. In [60], projection onto convex sets (POCS) method was implemented for solving (5.4). POCS is a method to find a point in the intersection of two closed convex sets. This is a simple algorithm and solves the following problem,

`find` $x \in \mathbb{R}^n$ `such that` $x \in A \cap B$, where A and B are closed convex sets.

However, the POCS is sub-optimal. Tellado and Cioffi provided a thorough analysis on solving (5.4) by posing it as linear programming problem that has an exact solution [45, 62] that can be reached with a complexity $\mathcal{O}[N \log N]$. Another sub-optimal method, namely gradient search, has been presented by them, which has a complexity $\mathcal{O}[N]$ [62].

Though impressive, TR is not without shortcomings. Since some tones are reserved for PAPR reduction, there will be loss of data rate. In [41], for TR method, nearly 20% of the total subcarriers could be reserved. TR technique increases the average power of the signal which means that, if more tones are to be reserved, then less power has to be allocated for PAPR reduction, which implies a tradeoff between number of reserved tones and average power increase.

5.2.3.3 Tone Injection

Prompted by data rate loss in TR, Tellado has introduced Tone Injection (TI) [45]. The idea is to enlarge the original constellation by ν times (*for e.g., from a QPSK constellation to 16QAM or 64QAM constellation*). By shifting the copies of the original constellation, the extra constellation points are generated. Assume d_{min} be the minimum distance between two points in the original MQAM constellation, then the constellation copies are separated by distance q in such a way that d_{min} of the enlarged constellation is same as the original d_{min} as below,

$$p \geq d_{min} \log_2 M \tag{5.5}$$

PAPR reduction is possible if the original constellation is arranged properly. The catch in this scheme is that by taking modulo p of the in-phase and quadrature phase components of the received signal, the receiver can recover the original constellation. This means that for TI, there is no need to transmit the Side Information (SI) to the receiver. Like TR, this scheme also involves an increase of average power since it is intuitive that any extension of the constellation will lead to increase in average power.

Arguably, there are two degrees of freedom in TI. One is the choice of tones and the other is the size of enlarged constellation which depends on ν. Searching the right possible combination involves high complexity.

5.2.3.4 Active Constellation Extension

This PAPR reduction technique was first proposed in [63]. Thought both TI and Active Constellation Extension (ACE) involves in extended constellation, the later differs in the manner of the constellation extension. Similar to that of TI, in ACE the minimum distance is not decreased explicitly, however in a peak power constraint system, it does. The original constellation is extended only in the regions of the signal plane where the new extended point should be further from any other points. Same methods used for TR such as POCS or gradient search algorithm, can be employed for the finding of the extension points.

5.2.3.5 Block coding

One of the notable techniques for reducing PAPR is Block coding. In this technique, an input data is encoded to a codeword with low PAPR. For example, in order to reduce the PAPR of OFDM signals with four sub-carriers, three-bit input data can be mapped to a four-bit codeword and a parity is added to the last bit in the frequency domain. Golay complementary sequence as codewords, can also be used to achieve the same, which can ensure that the OFDM signals with any number of sub-carriers, have PAPR of at most 3 dB [64]. A soft Reed-Muller decoding algorithm has been proposed in [65], to make this method more efficient. Another method, by constructing Golay complementary sequences with 64QAM constellation for OFDM signals has also been proposed [66]. Albeit, the usage of Golay complementary sequence can incur significant rate loss due to redundancy. Another disadvantage in coding methods is that they are not downward compatible since the receiver has to be modified (with a decoding algorithm).

5.2.3.6 Partial Transmit Scheme

Partial Transmit Scheme (PTS) was first introduced as PAPR reduction scheme in [67]. In this scheme, the frequency domain symbols with N sub-carriers, X, are partitioned into *V disjoint* sub-blocks, that are zero-padded to be length N as below,

$$X = \sum_{\nu=0}^{V-1} X^{(\nu)} \tag{5.6}$$

The above operation is called *sub-block partitioning*. Three different partitioning strategies have been proposed in [68], [69], and the random partitioning strategy, typically yields the best PAPR reduction performance, for the numerical results. Then, each sub-block is multiplied by an optimized sequence of phase constants $\left\{e^{j\phi^{(\nu)}}\right\}_{\nu=0}^{V-1}$, in such a way that the PAPR is reduced. The phase constants are drawn from a finite set of alphabets, $\mathcal{A}$, where $|\mathcal{A}| = P$. Since IFFT is a linear operation, we can do this multiplication in time domain also,

$$IFFT\left\{\sum_{\nu=0}^{V-1} X^{(\nu)} e^{j\phi^{(\nu)}}\right\} = \sum_{\nu=0}^{V-1} IFFT\left\{X^{(\nu)}\right\} e^{j\phi^{(\nu)}} \tag{5.7}$$

Because of this property, IFFT computation is made only one time, for each partitioned symbols $X^{(\nu)}$. The aim of the PTS is to find $\left\{e^{j\phi^{(\nu)}}\right\}_{\nu=0}^{V-1}$ such that,

$$\left\{\phi^{(\nu)}\right\}_{\nu=0}^{V-1} = \arg\min_{\{\phi^{(\nu)}\}_{\nu=0}^{V-1}} \left[max \left| \sum_{\nu=0}^{V-1} IDFT\left\{X^{(\nu)}\right\} e^{j\phi^{(\nu)}} \right| \right] \tag{5.8}$$

The PAPR reduction capability of PTS depends on the size of V and P. Totally there are P^V possible "mappings" in a PTS scheme at the cost of V IFFT operations. However, these V IFFT operations are mostly on zero sequences, which reduces the complexity from $\mathcal{O}(VN\log N)$ to $\mathcal{O}(VN\log\frac{N}{V})$. Albeit, these mappings are not independent, since every sub-block is multiplied by same phase constant. Therefore, the PAPR of one mapping is correlated with the PAPR of another mapping whenever the mapping is not independent. This is the reason for PTS falling well behind of a scheme like SLM that test P^V $independent$ mappings. In PTS, a side information (SI) that can distinguish P^V different mappings has to be transmitted that needs $V\log_2 P$ bits. PTS and SLM are both generalizations of each other. SLM is a PTS scheme, where only one carrier is present in each sub-block, i.e. each sub-carrier is rotated individually instead of rotation of sub-blocks of sub-carriers.

5.2.3.7 SeLected Mapping

SeLected Mapping (SLM) was introduced in [70] by Bauml, Fischer and Huber, where the term "selected mapping" was coined. However, similar ideas were proposed around that time [71, 72]. SLM takes advantages of the fact that the PAPR of an OFDM signal is heavily dependent on phase shifts in its frequency-domain. The algorithm of a classical SLM scheme is presented below,

Step 1 - Initialization: Firstly, we generate U phase rotation vectors $\boldsymbol{\theta}^{(u)}$ of length N as:

$$\theta_k^{(u)} = e^{j\psi_k} \in \mathbb{C},\ u \in \{1,..U\},\ k \in \{1,..N\},\ \psi_k \in [0, 2\pi) \tag{5.9}$$

where, $\theta_k^{(u)}$ is the k^{th} element of the vector $\boldsymbol{\theta}^{(u)}$ and without loss of generality we choose $\boldsymbol{\theta}^{(1)} = \{1, 1, ..., 1\}(N\ times)$.

Step 2 - Rotation: The frequency-domain input symbols $\mathbf{X}$ with N sub-carriers, are phase rotated by U phase rotations vectors $\boldsymbol{\theta}^{(u)}$, each having a size of N each,

$$\mathbf{X}^{(u)} = \mathbf{X}\ \odot\ \boldsymbol{\theta}^{(u)} \tag{5.10}$$

where $\odot$ implies carrier-wise point to point multiplication.

Step 3 - Selection: By applying IFFT operation on $\mathbf{X}^{(u)}$ we obtain the time-domain signals $\mathbf{x}^{(u)}$. The signal with least PAPR is chosen and the index of respective phase rotation vector is sent to receiver as Side Information (SI),

$$u_{min} = \underset{0\le u<U}{\arg\min}\left[PAPR\{\mathbf{x}^{(u)}\}\right] \tag{5.11}$$

Ideally speaking, a SLM scheme will generate U *independent* mappings of the time-domain signal $\mathbf{x}$. If we assume that all mappings are independent to each other, then CCDF of PAPR in a SLM scheme can written simply as

$$Pr\left[PAPR\{\mathbf{x}^{(u_{min})}\} > \gamma\right] = Pr\left[\bigcap_{u=1}^{U}(PAPR\{\mathbf{x}^{(u)}\} > \gamma)\right] \tag{5.12}$$

$$= Pr\left[(PAPR\{\mathbf{x}\} > \gamma)\right]^U \tag{5.13}$$

In the case of **x** being a non-oversampled OFDM signal [73], (5.13) can be simplified as

$$Pr\left[PAPR\left\{\mathbf{x}^{(u_{min})}\right\} > \gamma\right] = \left[1-(1-e^{-\gamma})^{N}\right]^{U} \tag{5.14}$$

$$= 1 - F_{PAPR}(\gamma) \tag{5.15}$$

where, $F_{PAPR}(\gamma)$ is the cumulative distribution function (CDF) of the PAPR of the discrete-time SLM signal, whose derivative yields the probability density function (PDF) $f_{PAPR}(\gamma)$.

SLM can be viewed as method that searches the "PAPR sample space" in a random manner, where the phase mapping can be considered of as one sampling from that PAPR sample space.

Probabilistic solutions such as PTS and SLM schemes are of relatively low complexity and have no impact on BER performance in the case of perfect SI recovery, making them more captivating.

5.2.4 Recent methods suggested for FBMC systems

Due to the overlapping nature in the signal structure of FBMC, we can't directly utilize the PAPR reduction techniques proposed for OFDM systems as it is. A clipping based scheme with its iterative compensation has been proposed in [74], where an iterative noise cancellation technique, namely the Bussgang Noise Cancellation (BNC) has been employed. Another PAPR reduction technique based on TR with a sliding window has been proposed in [75]. A method named Overlapped SLM (OSLM) was introduced in [76] which takes into account the overlapping nature of the FBMC symbols. A PTS scheme with Multi-block Joint optimization (MBJO) was introduced in [77], where it was shown that FBMC outperforms OFDM when the overlapping nature of FBMC signals are exploited properly. A sub-optimal scheme MBJO-PTS with low complexity was also put forth in the same paper.

5.3 Overview of FBMC system

5.3.1 FBMC signal structure

In a FBMC system we use complex symbols that are modulated based on OQAM and then transmitted [17]. The input symbols at the transmitter can be written as,

$$C_{m,n} = R_m^n + j.I_m^n,\ 0 \le n \le N-1,\ 0 \le m \le M-1 \tag{5.16}$$

where, R_m^n and I_m^n are the real and imaginary parts of the m^{th} symbol on the n^{th} sub-carrier, respectively. The input symbols in mth data block can be grouped as a vector as shown below,

$$\mathbf{C}_m = (C_{m,0}, C_{m,1}, ...C_{m,N-1})^T,\ 0 \le n \le N-1 \tag{5.17}$$

In OQAM the real and imaginary parts of the symbols are time staggered by $T/2$, where T is the symbol period. It is done in such a way that, for every two adjacent sub-carriers, the timing offset of $T/2$ is introduced on the real part of the former symbol whereas it will be on the imaginary part of the latter one. Then, these symbols are passed through a bank of synthesis

filters to get modulated with N sub-carriers where the spacing between every two sub-carriers is $1/T$ [78]. Then a FBMC modulated signal with M symbols can be written as,

$$s(t) = \sum_{n=0}^{N-1} \sum_{m'=0}^{2M-1} a_{m',n} h(t - m'T/2) e^{j\frac{2\pi}{T}nt} e^{j\varphi_{m',n}} \tag{5.18}$$

where $a_{m',n}$ is a real symbol mapped from complex $C_{m,n}$ with m varying from 0 to $M-1$ as follows,

$$a_{m',n} = \begin{cases} (1-\delta).R_m^n + \delta.I_m^n & \text{m' is even} \\ \delta.R_m^n + (1-\delta).I_m^n & \text{m' is odd} \end{cases} \tag{5.19}$$

where $\delta \in \{0, 1\}$ and is defined as n modulo 2.

Also, $h(t)$ is the impulse response of the prototype filter. The mathematical significance of this time-staggering rule appears in [79] that has got a phase term $\varphi_{m',n}$, which is set to be $\frac{\pi}{2}(m'+n) - \pi m'n$ without loss of generality. One possible prototype filter for FBMC system was originally designed by Bellanger [19] and later chosen to be the reference prototype filter of the European project Physical Layer for Dynamic Spectrum Access and Cognitive Radio (PHYDYAS). The design of this filter is based on frequency sampling technique. The analytical parameters involved in this filter design are the number of sub-carriers N, the overlapping factor K, the roll-off α and the length of the filter, $L = KN$ with desired values $F(k/L)$ where $k = 0, 1, ...L-1$.

$$\begin{aligned} &F_0 = 1, F_1 = 0.97196, F_2 = 1/\sqrt{2} \\ &F_3 = \sqrt{1 - F_1^2}, F_k = 0,\ 4 < k < L-1 \end{aligned} \tag{5.20}$$

The impulse response of the PHYDYAS filter is given as [19],

$$h(t) = \begin{cases} \frac{1}{\sqrt{A}}[1 + 2\sum_{k=1}^{K-1}(-1)^k F_k cos(\frac{2\pi kt}{KT})] & t \in [0, KT] \\ 0 & \text{elsewhere} \end{cases} \tag{5.21}$$

where the normalization constant, $A = KT\left[1 + 2\sum_{k=1}^{K-1} F_k^2\right]$.

The analytical PSD of FBMC system with prototype filter is given by [80]

$$\Phi_{FBMC}(f) = \left[\sum_{k=-(K-1)}^{k=K-1} F_k \frac{sin(\pi(f - \frac{k}{NK})NK)}{NKsin(\pi(f - \frac{k}{NK}))}\right]^2 \tag{5.22}$$

In figure 5-1, we can have a glance of the impulse responses for both OFDM which has a rectangular shape and FBMC that uses a PHYDYAS filter. We can notice that unlike the OFDM pulse shape, the impulse response of the PHYDYAS filter has duration that spans over $4T$.

5.3.2 Power profile of FBMC signals

FBMC signal spreads beyond one symbol period. The spreading length depends on the impulse response of the prototype filter (in our case it is $4T$). This is the reason behind the FBMC

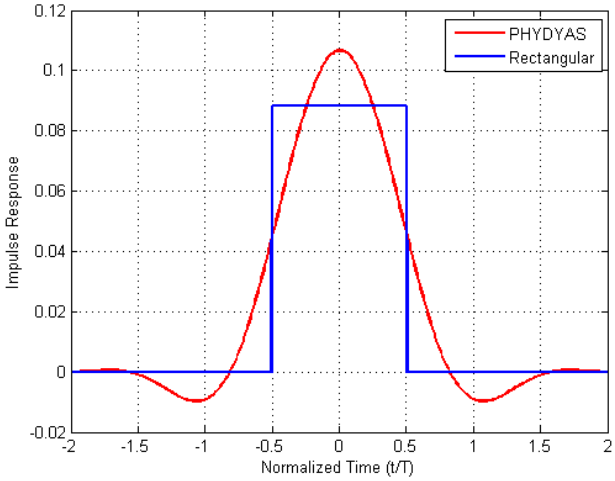


Figure 5-1: Impulse response for PHYDYAS and rectangular filters.

signals of adjacent data blocks getting overlapped each other. The energy of PHYDYAS filter lies mostly in the main lobe thus making symbol-by-symbol optimization unsuitable. The mean-power profile of the FBMC signal is defined as,

$$P_{avg}\Big[s(t)\Big] = \mathbb{E}\left[|s(t)|^2\right] \tag{5.23}$$

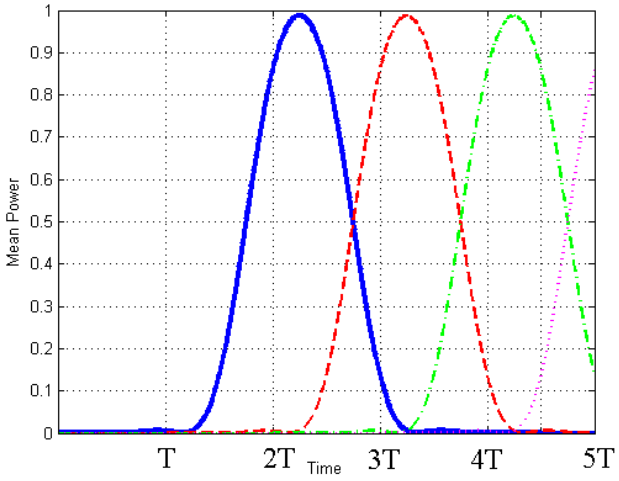


Figure 5-2: Illustration of mean-power overlapping among FBMC symbols.

where $\mathbb{E}[.]$ is the expectation operator. An FBMC signal with 1024 sub-carriers has been simulated over 10^6 symbols and the mean power profile of one symbol is shown in blue color in figure 5-2. In that figure, we can observe that most of the energy of the symbol lies in the succeeding two symbols period intervals in sharp contrast with that of an OFDM symbol.

We can notice that even though the length of prototype filter is $4T$, the time spanning of

each FBMC symbol lasts until $4.5T$ because of the the OQAM modulation, where an additional spread by $\frac{T}{2}$ occurs due to the offset of imaginary part. We can have a more elegant understanding about how FBMC symbols overlap each other by viewing figure 5-2. Since the prototype filter has a time period of $4T$, a given FBMC symbol overlaps over it's next three symbols while it significantly impact on two symbols which are the immediate preceding and succeeding symbols as evident from the same figure.

5.4 Comparison of the signal structures

In OFDM, the signal lasts for one symbol period, T. Adjacent OFDM symbols are independent and do not overlap each other. Therefore, Block-by-block optimization is sufficient.

In FBMC, the signal is spread beyond one symbol period T and depends on the impulse response of prototype filter $h(t)$. The signals of adjacent FBMC symbols overlap each other. Therefore, multi-block optimization is more efficient in the FBMC case.

5.5 Overlapping SLM techniques for FBMC

5.5.1 Classical SLM

In classical SLM scheme for OFDM, each symbol is rotated with different phase rotation vectors that are i.i.d and the optimally rotated symbol is chosen among others based on least PAPR criterion. The input symbol is phase rotated by U vectors, each having a size of N each. These U rotated input symbols possess same information and have identical constellation like the original input symbols. After the modulation, the PAPR is calculated over an OFDM symbol period and the symbol with the least PAPR is chosen which is referred as optimally rotated symbol.

5.5.2 Dispersive SLM

Similar to the classical SLM scheme, each OFDM symbol is rotated with different phase rotation vectors that are i.i.d and the optimally rotated symbol is chosen among others based on least PAPR criterion that has been computed over $[0, 4T)$ instead of $[0, T)$. The reason for not limiting to just $[0, T)$ is that most of the energy of the FBMC symbol lies in the succeeding two symbols period intervals rather than its own. This is also the same reason why classical SLM doesn't suit for effective PAPR reduction for FBMC systems. The proposed Dispersive SLM (DSLM) scheme deals with the time dispersive nature of the FBMC signals and hence termed as dispersive SLM. The algorithm of this scheme involves following steps,

Step 1 - Initialization: Firstly, we generate U phase rotation vectors $\boldsymbol{\theta}^{(u)}$ of length N as:

$$\theta_k^{(u)} = e^{j\psi_k} \in \mathbb{C},\ u \in \{1, ..U\},\ k \in \{1, ..N\},\ \psi_k \in [0, 2\pi) \tag{5.24}$$

where, $\theta_k^{(u)}$ is the k^{th} element of the vector $\boldsymbol{\theta}^{(u)}$ and without loss of generality we choose $\boldsymbol{\theta}^{(1)} = \{1, 1, ..., 1\}(N\ times)$.

Step 2 - Rotation: Each input symbol vector $\mathbf{C}_m$ is phase rotated with U different input

vectors giving $\mathbf{C}_m^{(u)}$, which carry same information and has identical constellation like $\mathbf{C}_m$ is formed. is given by,

$$\mathbf{C}_m^{(u)} = \mathbf{C}_m \odot \boldsymbol{\theta}^{(u)} \tag{5.25}$$

where $\odot$ implies carrier-wise point to point multiplication. Likewise the symbols, $a_{m',n}^{(u)}$ are chosen from $\mathbf{C}_m^{(u)}$ as per (5.19).

Step 3 - Modulation: OFDM modulation of the m^{th} input symbol considering the overlap of previous symbols is written by,

$$\begin{aligned} s^{(u)}(t) = &\sum_{n=0}^{N-1}\sum_{m'=0}^{2m-1} a_{m',n}^{(u_{min})} h(t - m'T/2) e^{j\frac{2\pi}{T}nt} e^{j\varphi_{m',n}} \\ &+ \sum_{n=0}^{N-1}\sum_{m'=2m}^{2m+1} a_{m',n}^{(u)} h(t - m'T/2) e^{j\frac{2\pi}{T}nt} e^{j\varphi_{m',n}} \end{aligned} \tag{5.26}$$

where,

- $s^{(u)}(t) \neq 0$ from $t = [0, (2m+1)\frac{T}{2} + 4T)$,
- $a_{m',n}^{(u_{min})}$ are from previous selected symbols $\mathbf{C}_m^{(u_{min})}$ and,
- u_{min} represents the indices of the phase vectors previously chosen.

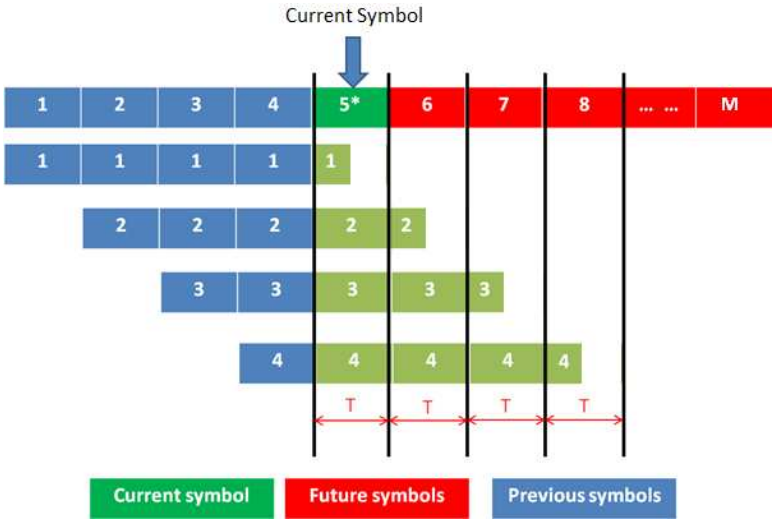


Figure 5-3: Block diagram of DSLM for FBMC systems.

Step 4 - PAPR Calculation: Then we compute the PAPR of $s^{(u)}(t)$ on a certain interval T_o given by,

$$PAPR_{(T_o)}^{(u)} = \frac{\max_{t\in T_o} |s^{(u)}(t)|^2}{\frac{1}{T_o}\int_{T_o} |s^{(u)}(t)|^2 . dt} \tag{5.27}$$

where T_o is any arbitrary interval that includes $[mT,\ mT + 4.5T]$ interval. However we choose $mT + 4T$ instead of $mT + 4.5T$ since almost all of the m^{th} symbol energy lies within the

[mT, mT+4T]$interval$.

Step 5 - Selection : $Among$PAPR$^{(u)}_{T_o}$, the index u is chosen for the signal with least PAPR as per the below criterion,

$$u_{min} = \min_{0 \leq u \leq U-1} PAPR^{(u)}_{(T_o)} \tag{5.28}$$

Step 6 - Updation: We update current overlapping input symbol vector as below,

$$\mathbf{C}^{(u_{min})}_m = \mathbf{C}_m \ . \ \boldsymbol{\theta}^{(u_{min})} \tag{5.29}$$

The input symbol that has been rotated with $\boldsymbol{\theta}^{(u_{min})}$ is considered to be optimally rotated w.r.t DSLM scheme.

The index u_{min} will be stored in a vector $\mathbf{U}_{SI}$ in order to be transmitted as SI for perfect recovery of the signal at the receiver. The vector $\mathbf{U}_{SI}$ which is a null vector initially; will be updated for every new symbol by row concatenation with the newly obtained u_{min}, as follows.

$$\mathbf{U}_{SI} = \begin{bmatrix} \mathbf{U}_{SI} \ u_{min} \end{bmatrix} \tag{5.30}$$

Then go to **Step 2** to repeat the same for next input FBMC symbol $\mathbf{C}_{m+1}$.

We can see the illustration of how the algorithm is implemented for a block of 5 symbols in figure 5-3. When calculating PAPR for the 5^{th} symbol, we consider the overlapping of previous 4 symbols also. In the same figure '*' on the current symbol denotes that it is a rotated symbol.

5.5.2.1 Simulation Results

The objective of the simulations is to understand the impact of duration T_o while calculating PAPR and comparison with OFDM when classical SLM scheme is used. Simulations are done for an FBMC signal that has been generated from 10^5 4QAM symbols with 64 sub-carriers. The PHYDYAS prototype filter was used which spans for $4T$ [19]. The range of the complex phase rotation vector was chosen such as, $\theta^{(u)}_k \in \{1, -1, j, -j\}$. In general most of the PAPR reduction schemes are implemented over discrete-time signals. So, we need to sample the continuous-time FBMC signal $s(t)$, thereby obtaining it's discrete-time signal $s[n]$. In order to well approximate the PAPR, we have over sampled the modulated signal by a factor $L = 4$ and then implemented the DSLM scheme on the discrete-time signal $s[n]$.

Impact of variation of T_o duration When computing the PAPR, the duration T_o seems to make a significant impact in the performance of DSLM scheme as depicted in figure 5-4. By varying the duration over which the PAPR is calculated, we can see how it is affecting the efficiency of the DSLM scheme. 'FBMC 1st', 'FBMC 23rd' and 'FBMC 1234th' in the legend indicate that the duration considered for PAPR calculation of a given OFDM symbol are $[0, T]$, $[T, 3T]$ and $[0, 4T]$ respectively. The phase rotation vector size is fixed for $U = 4$.

We can infer from this figure that when only current symbol period is considered (i.e $[0, T]$ w.r.t the current symbol), then it won't lead to any improvement. It implies that because of the

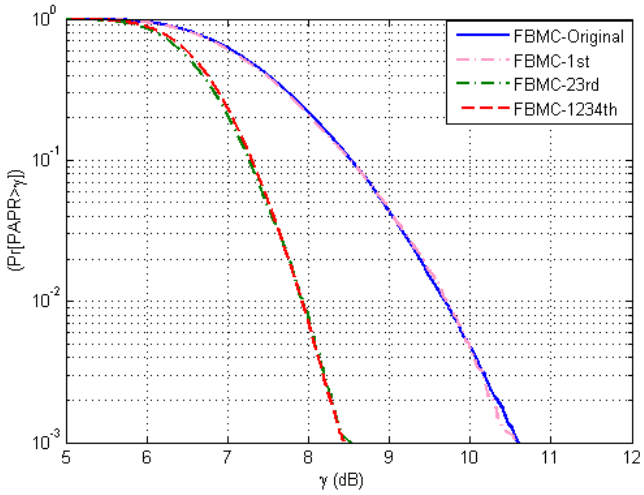


Figure 5-4: CCDF of PAPR plot for 10^5 FBMC symbols with PAPR calculated over $[0, T]$, $[T, 3T]$ and $[0, 4T]$ with $U = 4$ to illustrate the impact of variation of T_o duration on the DSLM scheme.

overlapping nature of FBMC symbols, direct implementation of classical SLM i.e. $T_o = [0, T]$ is ineffective. Looking at Fig. 5-2, it is quite obvious that the contribution of an FBMC symbol emitted at time k has negligible influence between kT and $(k+1)T$. Making the choice of the best rotation vector on such a time span T_o will give very bad performance.

Whereas when 2^{nd} and 3^{rd} symbol periods (i.e $[T, 3T]$ w.r.t the current symbol) and when 1^{st}, 2^{nd}, 3^{rd} and 4^{th} symbol periods (i.e $[0, 4T]$ w.r.t the current symbol) are taken into account then the performance of PAPR reduction with DSLM implementation seems to be trailing very closely that of the OFDM with classical SLM as we can see from figure 5-5. The reason behind this is well understood from the earlier figure 5-2 which shows that for a given FBMC symbol much of it's energy lies in 2^{nd} and 3^{rd} time intervals rather than in it's own interval.

By taking the time dispersion of FBMC symbols in to account, $T_o = [0, T]$ has been varied and we have found out that intervals $[T, 3T], [T, 4T]$ and $[0, 4T]$ offer notable PAPR reduction when compared to the case of $T_o = [0, T]$.

Impact of size of U Like any SLM scheme, the size of phase rotation vector impacts the performance of the PAPR reduction. For an illustration of impact of the size of U, we have considered $T_o = [0, 4T]$. The different sizes considered are $U = \{2, 4, 8\}$. We can see that the CCDF of PAPR for FBMC with DSLM is very closely trailing that of OFDM. It implies that when the overlapping nature of FBMC signals is taken into account, the adaptation of SLM to FBMC is possible with a little penalty compared to OFDM. Another observation is that as phase rotation vector size U is getting increased; we can see the performance gap between CCDF curves of OFDM and FBMC is getting increased.

Both OSLM [76] and DSLM schemes are compared. In the implementation of OSLM [76], oversampling was not done and Isotropic Orthogonal Transform Algorithm (IOTA) filter has been used as a prototype filter. So, as a matter of coherence during comparison, we have

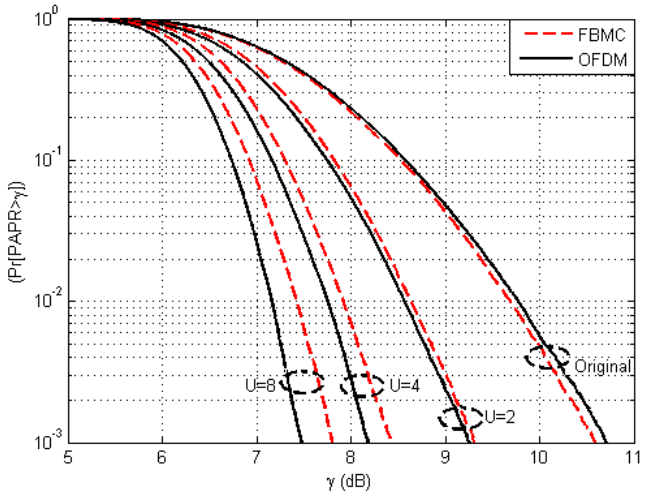


Figure 5-5: CCDF of PAPR plot for 10^5 FBMC symbols with PAPR calculated over $[0, 4T]$ with $U = \{2, 4, 8\}$ to illustrate the impact of size of U on the DSLM scheme in comparison with SLM scheme for OFDM.

implemented the DSLM scheme without oversampling and replacing PHYDYAS filter with the IOTA one. In terms of PAPR reduction, the DSLM with FBMC outperforms the OSLM and difference is in around of $0.26\ dB$, $0.67\ dB$ and $1.46\ dB$ at 10^{-3} value of CCDF of PAPR when $U = 2$, $U = 4$ and $U = 8$ respectively.

Impact of FFT size When the FFT size is increased, then we observe that the original PAPR increases, while the PAPR reduction capability of the DSLM based scheme remains almost same as shown in figure 5-6. We can observe that in comparison with the original PAPR and at 10^{-3} of CCDF, the PAPR reduction is around $2.16\ dB$ and $2.37\ dB$ when N is 64 and 128 respectively.

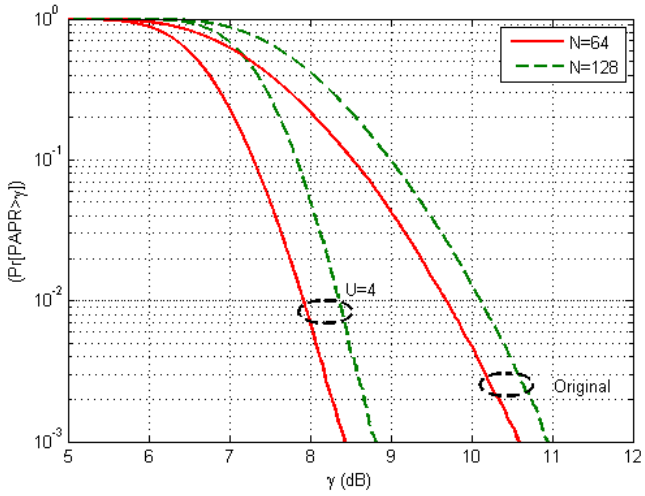


Figure 5-6: CCDF of PAPR plot for 10^5 FBMC symbols with PAPR calculated over $[0, 4T]$ with $U = 4$ and $N = \{64, 128\}$ to illustrate the impact of FFT size on the DSLM scheme.

5.5.2.2 Conclusion

A new SLM based scheme that is suitable for FBMC systems has been presented in this section. It is named as 'Dispersive SLM' since it takes into account the time dispersive nature of the FBMC symbols leading to their mutual overlapping. If PAPR calculation is done in only the current symbol period duration then it won't yield any improvement irrespective of the probabilistic scheme employed as most of the symbol energy lies in the two successive symbol periods. In terms of PAPR reduction, the DSLM with FBMC is very close to the performance of OFDM with classical SLM and difference is in around of $0.05\ dB$, $0.25\ dB$ and $0.32\ dB$ at 10^{-3} value of CCDF of PAPR when $U = 2$, $U = 4$ and $U = 8$ respectively.

5.6 Trellis-based SLM

5.6.1 Need for a Trellis-based method

In the previous section, we have seen that DSLM is closely trailing in performance, to that of OFDM. The reason behind the performance trailing is that the phase rotations of the past symbols are fixed or already chosen. Moreover, DSLM is a symbol-by-symbol optimization scheme. In order to exploit the overlapping nature of FBMC signals, one need to consider all the possible U phase rotations for all M symbols and pick out the best one out of the U^M different combinations. In practical sense, there is no meaning in this exhaustive search, since it adds mammoth complexity to the implementation of any SLM-based scheme.

In any SLM-based scheme, all the input symbols are rotated with U different phase rotation vectors that are i.i.d and they are FBMC modulated, giving U^M different patterns of the modulated signal, since all the input symbols are rotated independently. The partial PAPR that is calculated over a certain interval T_o for all U^M different FBMC signal patterns can be viewed as a '*metric*'. Where as, each symbol can be viewed as a '*node*'; while each phase rotation can be viewed as a '*state*'. The metric based on the PAPR measure of a FBMC signal pattern can be viewed as a '*path metric*' that gives information on the phase rotations of the input symbols.

In symbol-by-symbol approach, whatever improvement in PAPR reduction we may obtain for the current symbol, can be destroyed by the future symbol, which is the main reason for such a scheme like DSLM lagging behind in performance to that of OFDM. In fact, when we implement any SLM-based scheme, the FBMC signal obtained from modulation of M complex input symbols that are rotated with U i.i.d phase rotations, can be viewed as an $overlapping\ Markov\ chain$ (*since the 'states' are finite, i.e. they are countable and 'nodes' are discrete, nevertheless overlapping*). So, the trellis-based schemes which comprises of optimizing more than one symbol, offer naturally a better performance in terms of PAPR reduction than symbol-by-symbol optimization schemes. So, the proposed Trellis-based scheme tries to find the optimal state transition path i.e. set of optimal phase rotation vectors. The whole optimization problem in this regard can be viewed as a continuum of overlapping optimization sub-problems. This is where, the dynamic programming comes into the picture, which can help in reducing substantially, the number of paths one need to pick, in order to choose the optimal phase rotation for the symbols; thereby reducing massively the complexity involved in solving the optimization problem.

5.6.2 Description of the Trellis-based SLM algorithm

The proposed scheme is named as Trellis-based SLM (TSLM) since it involves trellis-based optimization of SLM by viewing FBMC signal as an $overlapping\ Markov\ chain$. Every two symbols are rotated with different phase rotation vectors that are i.i.d and are FBMC modulated.

Definition of state: For the first input FBMC symbol $\mathbf{C}_1$, at time T, we have U states: $\mathbf{C}_1.\theta^{(1)}, \mathbf{C}_1.\theta^{(2)}, ...\mathbf{C}_1.\theta^{(U)}$. For the k^{th} FBMC symbol $\mathbf{C}_k$, at time $k.T$, we have U states: $\mathbf{C}_k.\theta^{(1)}, \mathbf{C}_k.\theta^{(2)}, ...\mathbf{C}_k.\theta^{(U)}$ If we send a stream of M FBMC symbols we have U^M different states. To be precise, each rotated version of FBMC symbol represents a state.

Definition of path: A path between two successive states represents a transition from two states, for example from $\mathbf{C}_p.\theta^{(j)}$ to $\mathbf{C}_{p+1}.\theta^{(\acute{j})}$. Starting from state $\mathbf{C}_p.\theta^{(j)}$ there are U different paths going to $\mathbf{C}_{p+1}.\theta^{(1)}, \mathbf{C}_{p+1}.\theta^{(2)}$,â|,$\mathbf{C}_{p+1}.\theta^{(U)}$. In the same manner, arriving at state $\mathbf{C}_{p+1}.\theta^{(\acute{j})}$ there are U incoming paths coming from $\mathbf{C}_p.\theta^{(1)}, \mathbf{C}_p.\theta^{(2)}$,â|,$\mathbf{C}_p.\theta^{(U)}$. The objective is to find the best combination of multiplicative vectors that gives the lowest PAPR for this string of M emitted FBMC symbols. This is equivalent to find the path within the trellis with the lowest PAPR. In order to do that, we need to assign to each path a path metric.

Definition of path metric: The objective being to minimize the overall PAPR, the path metric must be related to the PAPR of the emitted signal. For example, if we consider the path from $\mathbf{C}_p.\theta^{(j)}$ to $\mathbf{C}_{p+1}.\theta^{(\acute{j})}$, we have to compute the PAPR of the emitted signal when $\theta^{(j)}$ is used as multiplicative vector for FBMC symbol $\mathbf{C}_p$ and $\theta^{(\acute{j})}$ is used as multiplicative vector for FBMC symbol $\mathbf{C}_{p+1}$. The Path Metric (PM) will be a function f of the PAPR: $PM[\mathbf{C}_p.\theta^{(j)}, \mathbf{C}_{p+1}.\theta^{(\acute{j})}] = f$[PAPR(FBMC signal with $\theta^{(j)}$ and $\theta^{(\acute{j})}$ at time $p.T$ and $(p+1).T$ respectively)]. (we will discuss later on function f(.)).

Definition of state metric: At time $p.T$ all the U states $\mathbf{C}_p.\theta^{(1)}, \mathbf{C}_p.\theta^{(2)}.....,\mathbf{C}_p.\theta^{(U)}$ have a state metric. This State Metric (SM) represents, as in classical Viterbi algorithm for convolutional codes, the summation of all path metrics of surviving paths. For example, arriving at state $\mathbf{C}_{p+1}.\theta^{(\acute{j})}$ there are U incoming paths coming from $\mathbf{C}_p.\theta^{(1)}$, $\mathbf{C}_p.\theta^{(2)}.....$, $\mathbf{C}_p.\theta^{(U)}$. The surviving path for state $\mathbf{C}_{p+1}.\theta^{(\acute{j})}$ will be the path that gives the lowest state metric. The final state metric of $\mathbf{C}_{p+1}.\theta^{(\acute{j})} = min_{j=1}^{U}[SM(\mathbf{C}_p.\theta^{(j)}) + PM[\mathbf{C}_p.\theta^{(j)}, \mathbf{C}_{p+1}.\theta^{(\acute{j})}]]$ and the surviving path is the path that reaches the minimum final state metric of $\mathbf{C}_{p+1}.\theta^{(\acute{j})}$.

Each FBMC symbol can be viewed as a node, which has U states. The two optimal '*states*' between the two successive '*nodes*', hereafter termed as *optimal transition*, are chosen among others, based on least PAPR criterion that has been computed over $T_o \in [T, 4T]$. The algorithm of TSLM scheme involves the following steps,

Step 1 - Initialization: Firstly, we generate U phase rotation vectors $\boldsymbol{\theta}^{(u)}$ of length N as:

$$\theta_k^{(u)} = e^{j\psi_k} \in \mathbb{C},\ u \in \{1, ..U\},\ k \in \{1, ..N\},\ \psi_k \in [0, 2\pi) \tag{5.31}$$

where, $\theta_k^{(u)}$ is the k^{th} element of the vector $\boldsymbol{\theta}^{(u)}$ and without loss of generality we choose $\boldsymbol{\theta}^{(1)} = \{1, 1, ..., 1\}$(*N times*).

Secondly, the '*state metrics*' for all states of the first symbol all initialized to zero.

$$SM_{(u,0)} = 0,\ u = 1, 2, ..., U \tag{5.32}$$

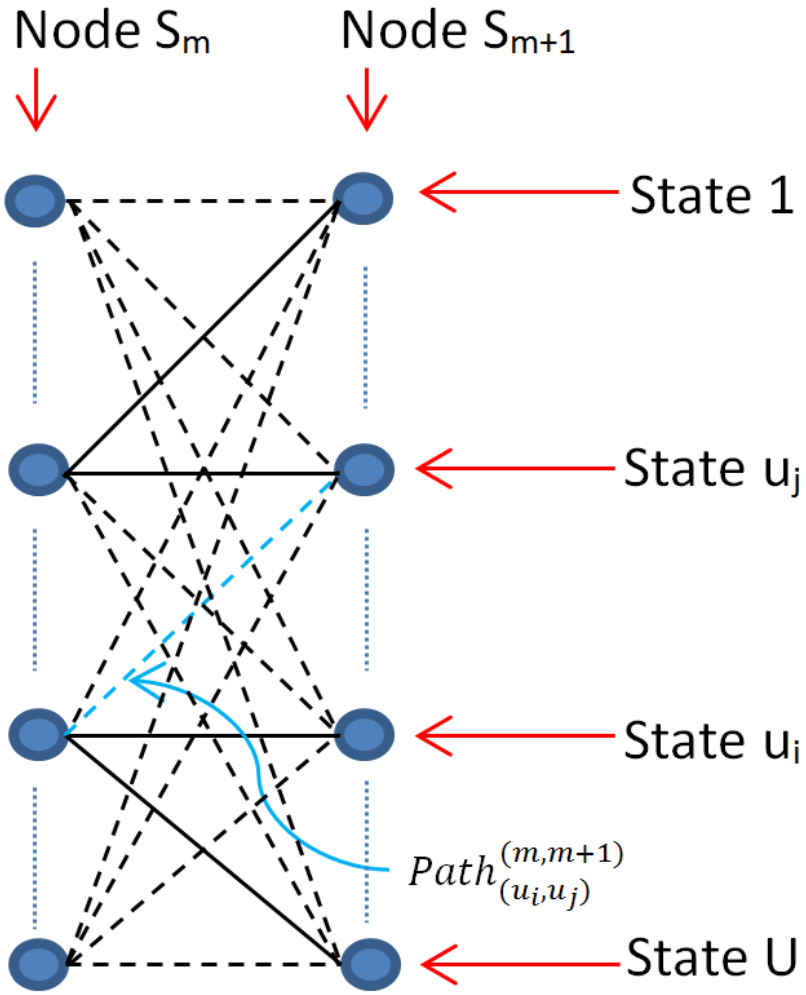


Figure 5-7: Illustration of the trellis diagram between the two '*nodes*' where each '*node*' has U different '*states*'.

Step 2 - Rotation: Two input symbol vectors $\mathbf{C}_m, \mathbf{C}_{m+1}$ are phase rotated with U different input vectors giving $\mathbf{C}_m^{(u)}$ and $\mathbf{C}_{m+1}^{(v)}$ respectively, which carry same information and has identical constellation like $\mathbf{C}_m$ and $\mathbf{C}_{m+1}$ respectively. They are given by,

$$\mathbf{C}_m^{(u)} = \mathbf{C}_m \odot \boldsymbol{\theta}^{(u)}, \ u \in \{1, ..U\} \tag{5.33}$$

$$\mathbf{C}_{m+1}^{(v)} = \mathbf{C}_{m+1} \odot \boldsymbol{\theta}^{(v)}, \ v \in \{1, ..U\} \tag{5.34}$$

where $\odot$ implies carrier-wise point to point multiplication. Likewise, the symbols, $a_{m',n}^{(u)}$ and $a_{m',n}^{(v)}$ are chosen from $\mathbf{C}_m^{(u)}$ and $\mathbf{C}_{m+1}^{(v)}$ respectively, as per (5.19).

Step 3 - Modulation: FBMC modulation of the m^{th} and $(m+1)^{th}$ input symbols, for

$m \in \{0, 1, \ldots M-2\}$, is written by,

$$s_m^{(u)}(t) = \sum_{n=0}^{N-1} \sum_{m'=2m}^{2m+1} a_{m',n}^{(u)} h(t - m'T/2) e^{j\frac{2\pi}{T}nt} e^{j\varphi_{m',n}} \tag{5.35}$$

$$s_{m+1}^{(v)}(t) = \sum_{n=0}^{N-1} \sum_{m'=2m+2}^{2m+3} a_{m',n}^{(v)} h(t - m'T/2) e^{j\frac{2\pi}{T}nt} e^{j\varphi_{m',n}} \tag{5.36}$$

$$s_{m,m+1}^{(u,v)}(t) = s_m^{(u)}(t) + s_{m+1}^{(v)}(t) \tag{5.37}$$

where, $s^{(u)}(t), s^{(v)}(t) \neq 0$ from $t = [0, (2m+1)\frac{T}{2} + 4T]$. From (5.37), it is intuitive that we have U^2 patterns of the modulated FBMC signal $s_{m,m+1}^{(u,v)}(t)$.

Step 4 - Path metric calculation: For each of the U^2 patterns of the modulated FBMC signal $s_{m,m+1}^{(u,v)}(t)$, we compute partial PAPR over duration $T_o \in [T, 4T]$ as given below,

$$PAPR_{(T_o)}^{(u,v)} = \frac{\max_{t \in T_o} |s_{m,m+1}^{(u,v)}(t)|^2}{\frac{1}{T_o} \int_{T_o} |s_{m,m+1}^{(u,v)}(t)|^2 . dt} \tag{5.38}$$

where $T_o \in [mT + T,\ mT + 4T]$ interval since almost all of the energy of the FBMC symbol $s_{m,m+1}^{(u,v)}(t)$, lies within that interval. We can view these partial PAPR values $PAPR_{(T_o)}^{(u,v)}$, as '*path metrics*' between different '*states*'.

The '*path metric*' $PM_{(m \Rightarrow m+1)}^{(u,v)}$, between any two *states* u of *node* s_m and v of node s_{m+1}, can be written as,

$$PM_{(m \Rightarrow m+1)}^{(u,v)} = f(PAPR_{(T_o)}^{(u,v)}) \tag{5.39}$$

where $f(.)$ is any convex function. The reason for the choice of the T_o can be clearly understood from figure 5-8.

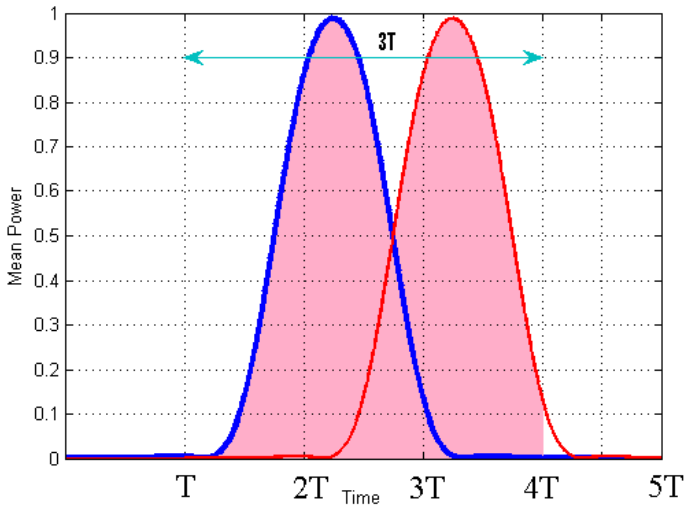


Figure 5-8: Power Profile of two FBMC symbols in the duration of $[T, 4T]$ w.r.t the current symbol.

Step 5 - Survivor path identification: The states for *nodes* s_m that are related to the '*survivor paths*' leading to node s_{m+1}, are stored in a '*State Matrix*' $\lambda(v,m)$ as given below,

$$\lambda(v,m) = \min_{u\in[1,U]}\left[SM_{(u,m)} + PM^{(u,v)}_{(m\Rightarrow m+1)}\right],\ v = 1,2,...,U \tag{5.40}$$

Step 6 - State metric updation: The '*state metric*' $SM_{(u,m+1)}$, for the *node* s_{m+1}, can be updated as follows,

$$SM_{(v,m+1)} = SM_{(\lambda(v,m),m)} + PM^{(\lambda(v,m),v)}_{(m\Rightarrow m+1)},\ v = 1,2,...,U \tag{5.41}$$

Step 7 - Traceback: Once the *state metric* updating is done for all the *nodes*, then finding the unique *survivor path* from the first *node* to the last one can be done by tracing back. This survivor path which is to be transmitted to the receiver as *Side Information* hereby denoted as SI, can be traced back as below,

Initial condition:

$$SI(M-1) = \min_{u\in[1,U]}\left[SM_{(u,M-1)}\right] \tag{5.42}$$

Backward Computation:

$$SI(x) = \lambda(SI(x+1),x),\ x = M-2, M-3, ..., 1, 0 \tag{5.43}$$

5.6.3 Simulation results

The objective of the simulations is to analyze the performance of TSLM scheme in comparison with OFDM when classical SLM scheme is used. Simulations are done for an FBMC signal that has been generated from 10^5 4QAM symbols with 64 subcarriers. The PHYDYAS prototype filter was used which spans for $4T$ [19]. Like any SLM scheme, the size of phase rotation vector impacts the performance of the PAPR reduction. For an illustration of impact of the size of U, we have considered $T_o = [T, 4T]$. The different sizes considered are $U = \{2, 4, 8\}$. We can see from figure 5-9, that the CCDF of PAPR for FBMC with TSLM has superseded that of OFDM by around $0.3\ dB$ and $0.15\ dB$ at 10^{-3} value of CCDF of PAPR when $U = 2$ and $U = 4$ respectively.
By looking to this superior performance of TSLM, one can conclude that when the overlapping nature of the FBMC signal is well exploited then it can significantly impact the PAPR reduction. Another observation is that as phase rotation vector size U is getting increased; we can see the lead gap between CCDF curves of OFDM and FBMC is getting narrowed which we can observe that at 10^{-3} value of CCDF of PAPR when $U = 8$, its performance starts trailing to that of OFDM by $-0.04\ dB$.

We can see from figure 5-10, a clear comparison of the two schemes TSLM and DSLM for FBMC systems.

5.6.4 Impact of variation of T_o duration

When computing the PAPR, the duration T_o seems to make a significant impact in the performance of TSLM scheme as depicted in figure 5-4. By varying the duration over which the PAPR is calculated, we can see how it is affecting the efficiency of the DSLM scheme. In the legend, '[0,T]', '[0,2T]', '[T,2T]', '[T,3T]', '[T,4T]', '[2T,3T]', '[2T,4T]', '[0,6T]' indicate the

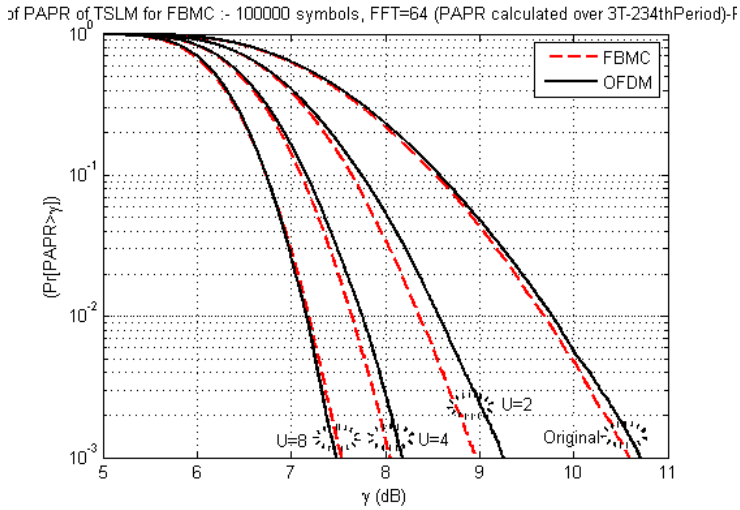


Figure 5-9: CCDF of PAPR plot for 10^5 FBMC symbols with PAPR calculated over $[T, 4T)$ with $U = 2, 4, 8$ to illustrate the impact of size of U on the TSLM scheme in comparison with SLM scheme for OFDM.

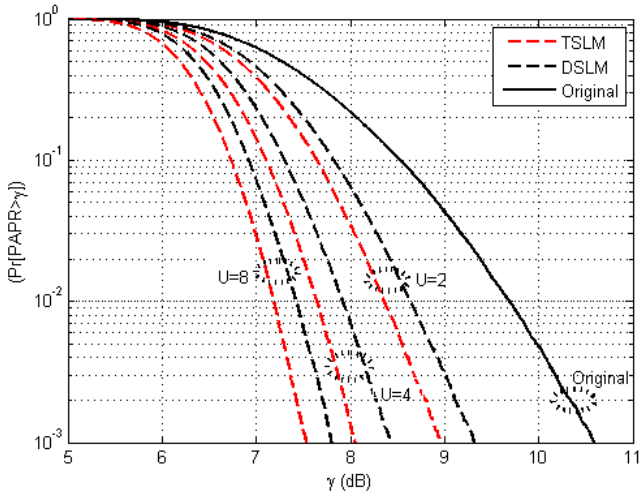


Figure 5-10: CCDF of PAPR plot for 10^5 FBMC symbols with PAPR calculated over $[T, 4T)$ with $U = 2, 4, 8$ to illustrate the comparison of the TSLM scheme with the earlier proposed DSLM scheme.

duration T_o considered for PAPR calculation of a given OFDM symbol in the case of TSLM, where phase rotation vector size is fixed for $U = 2$. Where as 'OFDM-Orig', 'OFDM-U=2' are related to OFDM, which indicate the original PAPR and PAPR with SLM when U=2.

5.7 PAPR characteristics and reduction in FC-FB based transmitters

The Fast-Convolution Filter Bank (FC-FB) structure presented in EMPhAtiC (Enhanced Multi-carrier Techniques for Professional Ad-Hoc and Cell-Based Communications) Deliverable D2.1 can be used for processing FBMC, FMT, and single-carrier (FB-SC) waveforms. Different wave-

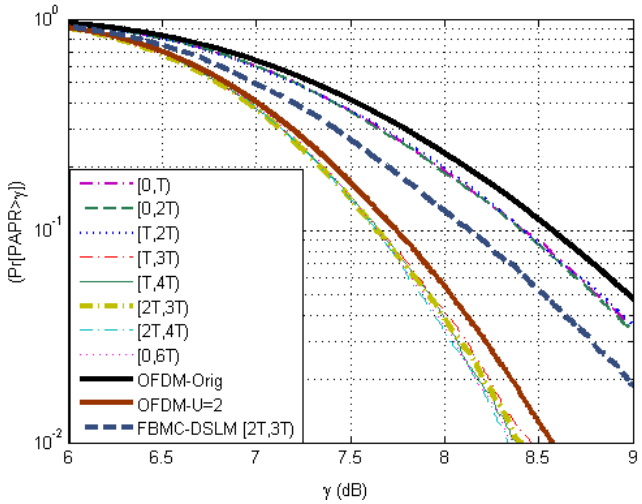


Figure 5-11: CCDF of PAPR plot for 5000 FBMC symbols with PAPR calculated over different T_o with $U = 2$ to illustrate the impact of variation of T_o duration on the DSLM scheme.

forms can be processed even simultaneously in different parts of the spectrum covered by the filter bank. The waveforms can be parameterized in a very flexible manner concerning center frequencies, bandwidths, and roll-offs of subchannels or subchannel multiplexes. Nyquist pulse shaping is used with root-raised cosine type of frequency responses. In this section we focus on the PAPR characteristics and mitigation of FBMC and SC waveforms in the FC-FB context. In case studies, we use the 1.4 MHz LTE-like parametrization selected for the EMPhAtiC demonstrator: 128 subcarriers, out of which 72 may be active, subcarrier spacing of 15 kHz, and 1.92 MHz sampling rate. The FC-FB uses long transform length of 1024 and short transform length of 16. The subcarrier frequency response in case of FBMC waveform with 15 kHz subcarrier spacing is defined by 16 weight coefficients, one for each IFFT bin.

5.7.1 PAPR characteristics of SC waveforms with very small roll-off

The basic subchannel filter design can be extended to wider bandwidths by using the same weight coefficients: The pass-band is extended by adding bins with value 1 and the stop-bands are extended by adding the same number of 0-valued weights (see figure 5-12 for an example). With this modification, the pulse-shaping filtering maintains the Nyquist characteristics and the root-raised cosine nature of frequency response.

With this approach, the extended subchannels use 2x oversampling in the transmitter and receiver. While the transition bandwidth is constant, the roll-off factor is reduced when the bandwidth is extended. In the basic design, the roll-off is 1. In general, when the bandwidth is increased by the factor of K, a block of K single carrier symbols is transmitted within one FBMC symbol, and the roll-off becomes 1/K. In case of multiuser FDMA operation (e.g., cellular uplink or ad-hoc operation), a single unused subcarrier is enough as a guard band.

In numerical studies, we consider SC-signal bandwidths of 1, 2, 6, 12, 24, and 72 subcarriers. The corresponding values of roll-offs are 1, 0.5, 0.167, 0.0833, 0.0417, 0.0139. The resulting PAPR characteristics are shown in figure 5-13. The PAPR is based on the peak values within each FBMC transmission block. For reliable estimation of the peak values, the sampling rate is increased by the factor of 4 by using length 4096 IFFT, and the CCDF is obtained by simulating 10^6 SC symbol blocks. The nature of the CCDF curves in the one subchannel cases is due to

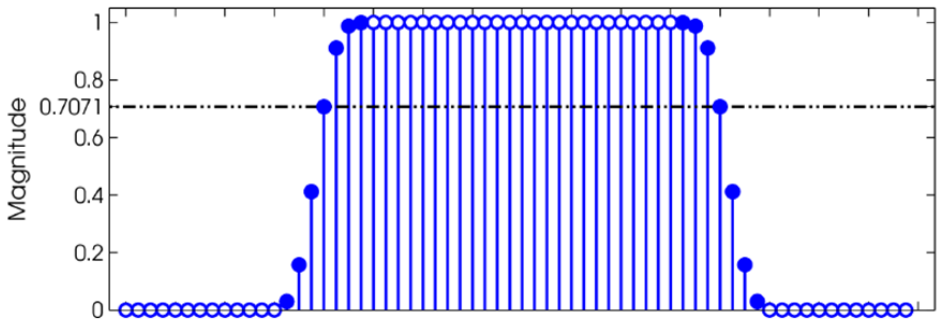


Figure 5-12: Example of an extended channel filter weight mask.

the use of QPSK and 64QAM modulations. The single-subcarrier case of OFDM has 0 dB PAPR with QPSK modulation. It can be seen that for low number of subcarriers, the PAPR of FB-SC is somewhat lower than that of OFDM based SC-FDMA, which is used in the LTE uplink. This is due to the higher roll-off in the narrowband cases of FB-SC. With increasing number of subcarriers, the CCDF of SC-FB approaches that of OFDM based SC.

It can be seen that the PAPR grows with reducing roll-off, as expected. However, the PAPR values are significantly smaller than for FBMC waveform with the same number of subcarriers.

5.7.2 Feasibility of PAPR reduction methods in FC-FB based transmitters

The FC-FB implementation structure has limitations from the PAPR mitigation point of view as it introduces additional difficulties with certain PAPR mitigation algorithms, notably the SLM and PTS methods. This is partly due to the overlapping nature of the FBMC symbols, as discussed in the previous sections. Furthermore, FC-FB generates multiple FBMC symbols in a single processing block, e.g., 5 symbols with the demonstrator parameters. The combination of these properties makes symbol-by-symbol based PAPR mitigation quite difficult to implement. One obvious possibility to avoid these difficulties is to employ polyphase FB based transmitter with FC-FB based receiver. In cellular uplink, this would be a natural choice, as in a mobile device, there is not so much need for multi-mode operation or the other advantageous features of the FC-FB structure as on the base station side. Anyway, maintaining the spectral containment of FBMC waveforms with practical HPAs is challenging also on the base station side, and there is clear interest to consider PAPR mitigation methods also in FC-FB implementations.

The PAPR methods which are based on adding a PAPR-controlling signal element to the generated FBMC waveform are more easy to handle in a FC-FB based transmitter than the SLM or PTS methods. Such methods include TI and TR [45]. We consider here the TR model, where the idea is to reserve a set of subcarriers for PAPR control only, i.e., no data is transmitted on those subcarriers (cf. subsection 5.2.3.2). We consider the specific case where one subcarrier out of each LTE Resource Block (RB) of 12 contiguous subcarriers is reserved for PAPR mitigation. The procedure can be formulated as follows:

1. Generate an FBMC transmission frame with zero-valued symbols in the reserved subcarriers.

2. Optimize the PAPR control values in a symbol-by-symbol manner over the processing frame, taking into account the overlap of previous symbol pulses with the current one.

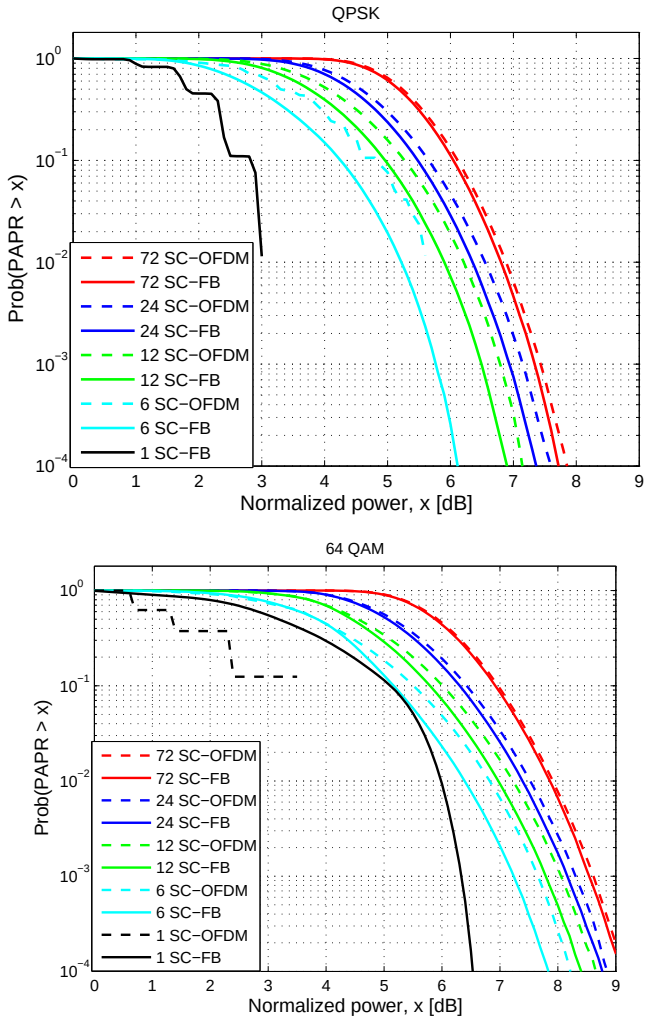


Figure 5-13: PAPR characteristics of OFDM based and FB based SC-waveforms with different bandwidths and roll-off factors. Upper: QPSK modulation. Lower: 64QAM modulation.

3. Generate the time-domain waveform corresponding to the optimized tones and add it to the waveform generated in Step 1.

The essential difference is that here only the PAPR control symbols need to be processed on symbol-by-symbol basis, while in SLM and PTS, alternative weighted combinations subcarrier symbol waveforms are tested and the combination with lowest peak value is selected. This cannot be done effectively with the FC-FB structure.

Figure 5-14 shows the effect of TR on the CCDF of PAPR in an example scenario with 1.4 MHz LTE like parameters. This is a non-contiguous (NC) FBMC case where the second one of the six RBs is silent, as the corresponding frequency band is reserved for narrow band transmissions. Six subcarriers (0, 12, 24, 36, 48, 60) are reserved for PAPR mitigation. Simplistic exhaustive search based algorithm (with rather high complexity) was used for optimizing the PAPR control values, in order to test the performance of the method. In case of TR, we define the PAPR as the ratio of the peak power with TR and the average power of the signal without any PAPR mitigation applied. In this way, the real benefit of the TR method is seen. In the considered case, the insertion of the PAPR control increases the average power by about 0.8

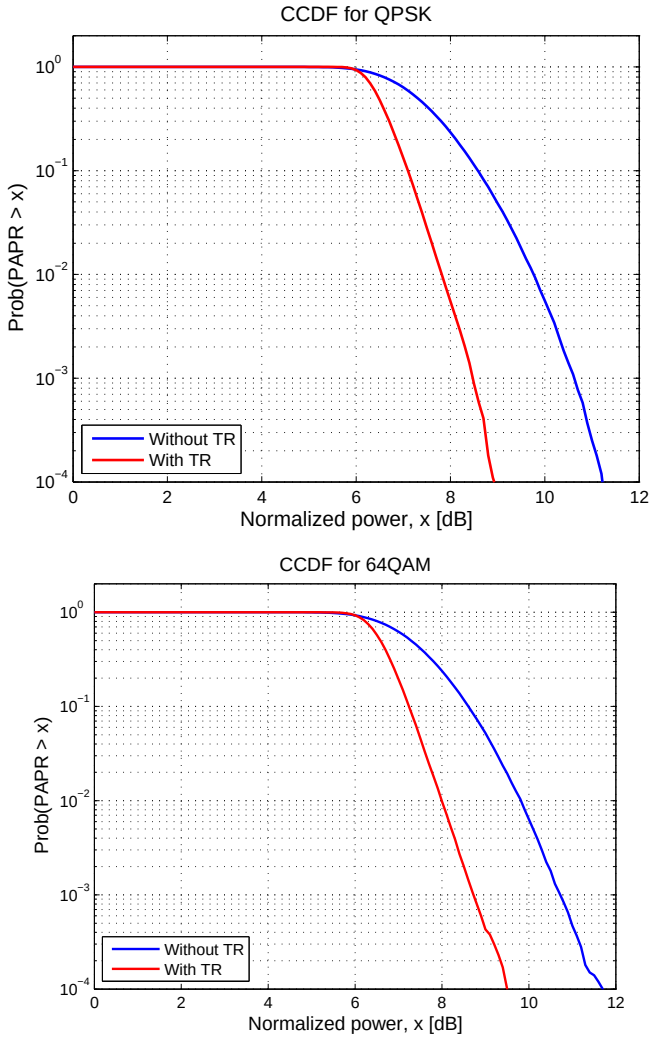


Figure 5-14: PAPR distribution with and without tone reservation in a FBMC case with 1.4 MHz LTE-like parameters for QPSK and 64QAM modulations.

dB with QPSK and 0.3 dB with 64QAM. With this definition of PAPR we can see about 2.1 dB improvement for QPSK and 2.0 dB improvement for 64QAM in PAPR at the probability level of 10^{-3}.

5.8 Conclusion

Since a FBMC signal is a overlapped Markov chain, the trellis-based schemes which comprises of optimizing more than one symbol, offer naturally a better performance in terms of PAPR reduction than symbol-by-symbol optimization schemes. So, a new SLM based scheme combined with Trellis based approach for joint block optimization, named as Trellis-based SLM (TSLM) has been proposed. In symbol-by-symbol approach, whatever improvement in PAPR reduction we may obtain for the current symbol, can be destroyed by the future symbol, which is the main reason for such a scheme like DSLM lagging behind in performance to that of OFDM. The PAPR duration also plays a vital role and it is found that $To \in [T, 4T]$ yields good results. In terms of PAPR reduction, the TSLM with FBMC is outperforming the performance of OFDM

with classical SLM.

FC-FB can be used for efficient implementation of single-carrier waveforms with very small roll-off factors and effective frequency-domain equalization on the receiver side. The PAPR characteristics of these FB-SC waveforms are similar (but slightly better) than those of the OFDM based SC-FDMA.

Methods like SLM and PTS are not well-suited for FC-FB based implementations of FBMC waveforms due to the difficulties in symbol-by-symbol processing. Nevertheless, TR techniques can be applied for FC-FB based MCM. When using a reserved tone for every 12 active tones (i.e., for 11 data subcarriers), significant PAPR reduction can be achieved (about 2 dB improvement in PAPR at the probability level of 10^{-3}, with an increase of the average power by about 0.8 dB for QPSK and 0.3 dB for 64QAM.

6. NL compensation and HPA linearization

6.1 State of the art of linearization techniques

HPA are NL devices with NL AM/AM and AM/PM conversions. As we have said in the introduction of this document, it is necessary to linearize these devices in order to improve power efficiency. Various techniques exist in literature for PA linearization [81]. These methods can be classified in two groups:

1. Linearization methods using modified HPA architectures. With these methods, a special architecture of the amplification device is used in order to reach an overall linear amplification function.

2. Linearization methods using a classical NL HPA with additional corrections of the NL impairments. With these methods the HPA is used as it is and additional functions are added for getting a linear transfer function.

6.1.1 Linearization methods using modified HPA architectures

Within the possible architectures of the first group we can point out the following methods:

- Linear Amplification using NL Components (LINC) [81]. The basis of the LINC architecture relies on the fact that it is possible to convert the input signal with non constant envelope and phase into two signals with constant envelopes. The two constant envelope signals are then amplified with two high power efficiency HPAs and added. The main difficulty in the LINC architecture is to guarantee that the two amplified signals are added without any phase error.

- Envelope Elimination and Restoration (EER) [81]. In the EER architecture, the non constant envelope/phase input signal is amplified by a controlled HPA. The HPA must have an output power that is function of a command signal. The input signal is clipped and the obtained constant envelope and non constant phase signal is amplified by a high power efficiency HPA. The envelope of the input signal is used for changing the HPA output power (generally, HPA DC power is changed for changing the HPA output power).

- Envelope Tracking (ET) [81]. The ET architecture is similar to the EER one. The envelope of the input signal is used for changing the HPA output power. The input signal is not clipped as in EER and is directly fed to the HPA input.

All the above methods need a very strong temporal synchronization within the different signals. Furthermore, the bandwidth of the envelope variation must be low (tens of MHz) in order to be able to command the HPA output power. Excepting the ET technique, all the above mentioned methods will not be considered in the following.

6.1.2 Linearization methods using classical HPA architectures

With these methods, classical amplifier architectures are used. Additional electronic functions are added around the NL HPA in order to linearize it. Within these methods we can point out:

- Feedback techniques [81]. In this technique a feedback loop is implemented between the HPA output signal and the input signal. In the Cartesian Feedback loop, for example, two loops on I and Q signal are used. Here also, a tight temporal synchronization is necessary within the different signals of the direct and feedback loop.

- Feed-forward techniques [81]. This is an open loop technique. The amplified signal, at the output of the HPA is compared to the input signal and an error is computed between the HPA output and the desired output. This error signal is further amplified and added to the HPA output in order to reach a linear transfer function. As for the preceding method, synchronization is a major problem of the feed-forward technique.

- Predistortion techniques [81]. The idea of the predistortion is very simple. It consists in adding, before the HPA a NL function that will compensate the NL AM/AM and AM/PM curves of the HPA. We will develop, in the following the predistortion technique.

6.1.3 Predistortion of NL HPA

This predistortion technique is illustrated in figure 6-1:

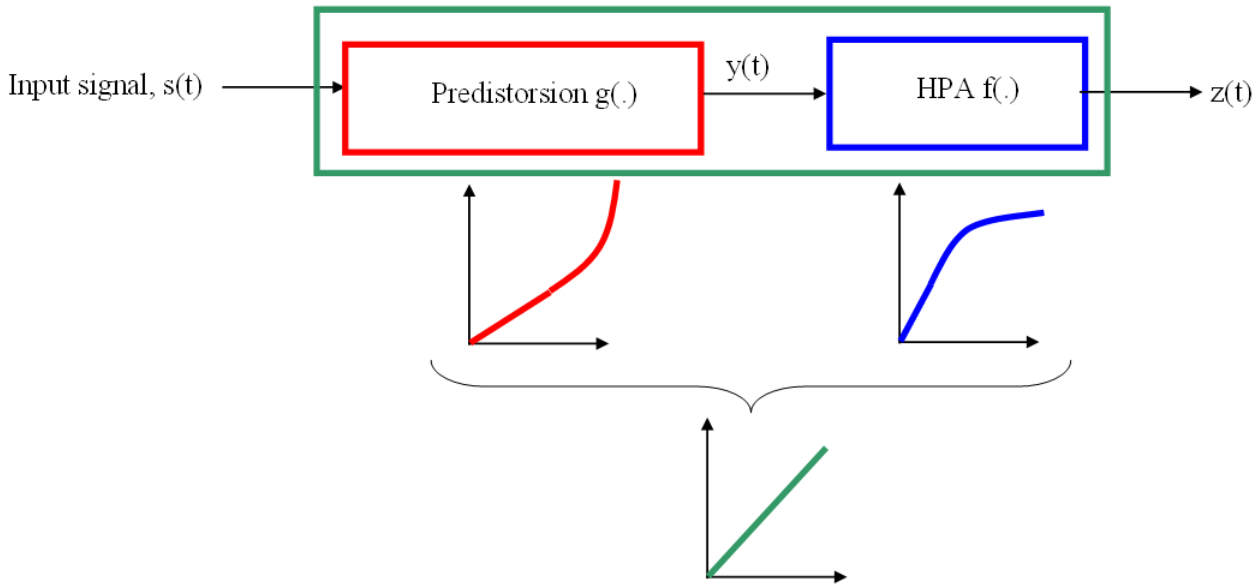


Figure 6-1: Principle of the predistorsion of a HPA.

We have:

$$z(t) = f(y(t)) = f(g(s(t))) \tag{6.1}$$

It's obvious that $z(t) = \alpha s(t)$ if and only if $f(g(.))$ is the identity function.

It must be noted that the linearization of the HPA cannot be realized for any input power from 0 to ∞. As we have seen in chapter 2, the output power of the HPA is limited to a saturation power P_{sat}. Thus, the best predistortion system will give a transfer function as in figure 6-2. The overall chain predistorter plus HPA will be linear in a certain area from 0 to P_{max} and will suffer saturation for input powers higher than P_{max}.

This behaviour is called a Soft Envelope Limiter (SEL (see section 2.3.1)). The overall transfer characteristic of a perfect predistorter plus HPA will be:

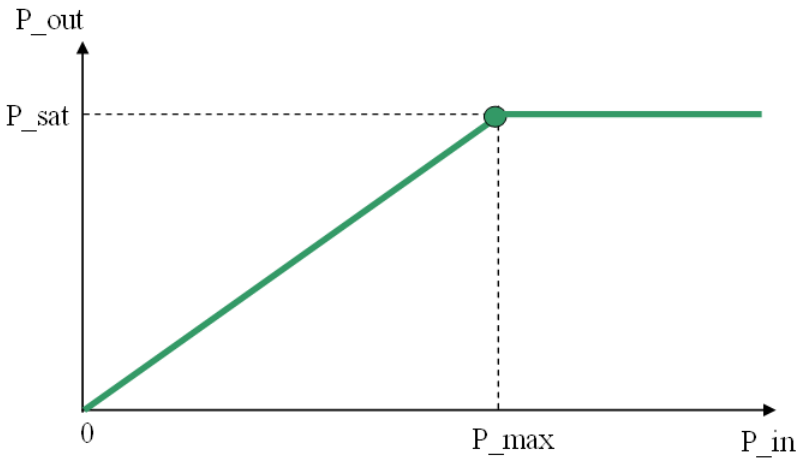


Figure 6-2: Ideal predistorsion result.

$$s(t) = re^{j\phi} \tag{6.2}$$

where $r = |s(t)|$ and $\phi = arg(s(t))$.

$$z(t) = \begin{cases} \alpha s(t) & \text{if } r < P_{max} \\ \sqrt{P_{max}} e^{j\phi} & \text{if } r > P_{max} \end{cases}$$

Realization of the predistortion function $g(.)$ can be done in baseband or in high frequency and in analog or digital form. Predistortion can be invariant or adaptive when the HPA characteristics are time varying. In the following we will concentrate on predistortion techniques in digital form, working in baseband and adaptive.

Among predistorsion techniques we can point out:

1. Look Up Tables (LUT) [82]. In this technique, for each input signal $s(t)$ a table gives the modulus and phase of the output predistorter signal (modulus and phase of signal $y(t)$ in figure 6-1. LUT can be adaptive.

2. Computed predistortion function $g(.)$. In this approach, the predistortion function $g(.)$ (see figure 6-1) is generated using a NL system. Function $g(.)$ can be invariant or adaptive. There exist several ways to implement the predistorter function (Volterra series, neural networks, polynomial functions, etc.).

In the following we will describe the second technique where function $g(.)$ is implemented using a NL system.

6.1.4 Predistortion of NL HPA using a NL system

The architecture of such predistorters is shown on figure 6-3. A fraction of the output HPA signal is captured via a coupler and demodulated. The demodulated signals $Id(t)$ and $Qd(t)$ are compared to the input signals $I(t)$ and $Q(t)$ and the predistortion function $g(.)$ is adapted in order to minimize the error between $Id(t)/I(t)$ and $Qd(t)/Q(t)$.

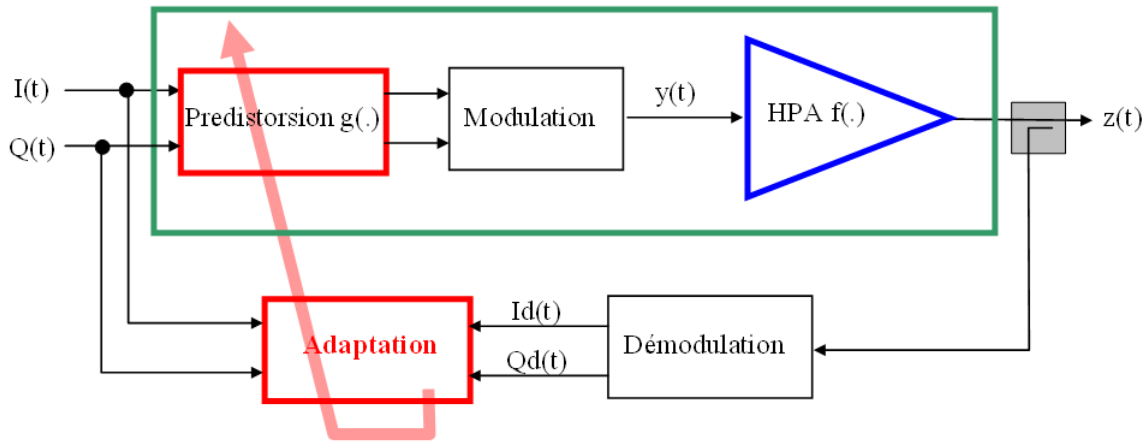


Figure 6-3: Architecture of a predistortion working in baseband.

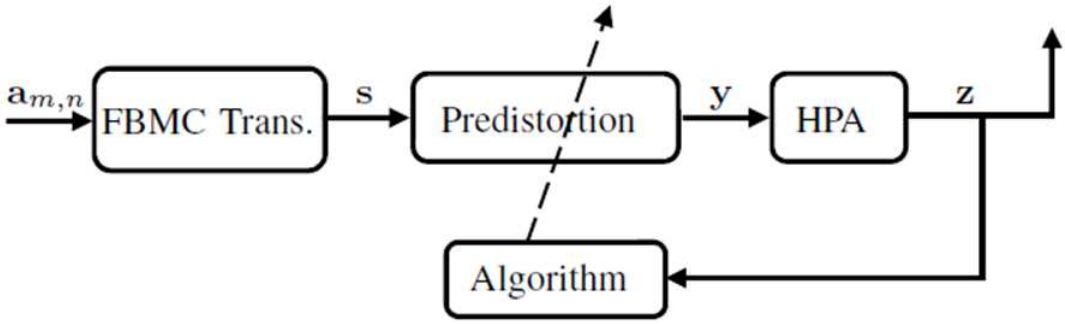


Figure 6-4: Principle of a baseband predistorsion.

In baseband the predistortion can be viewed as in figure 6-4:
In order to compute NL function $g(.)$ two approaches are possible:

1. Direct computation of $g(.)$ [83]. In this technique, the NL function $g(.)$ is adapted directly as seen on figure 6-5. The output signal $z(t)$ is compared to the input signal s(t) and the predistortion function is adapted in order to minimize the error.

2. Indirect computation of $g(.)$ [83]. Using indirect computation, the inverse of HPA NL function $f^{-1}(.)$ is preliminary computed. This is done by comparing the input of the HPA $(y(t))$ and the output of the inverse of the HPA transfer function $(yd(t))$. When the HPA transfer function computation has been done, this function is used for the predistorter as shown in figure 6-6.

6.2 Predistortion of FBMC signals using neural Networks

In order to realize the NL functions $f^{-1}(.)$ and $g(.)$, various NL systems can be used. Among them we have pointed out Voterra series, polynomial functions and Neural Networks (NN). All these systems are able to implement a NL function and adjusting the NL function is done by modifying the internal coefficients (coefficients of polynomial or Volterra functions and weights for the NN).

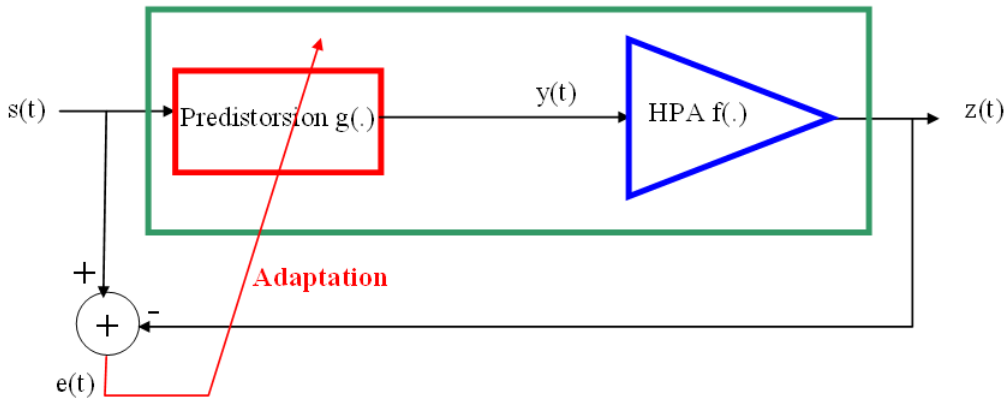


Figure 6-5: Direct adaptation of the predistorsion function $g(.)$.

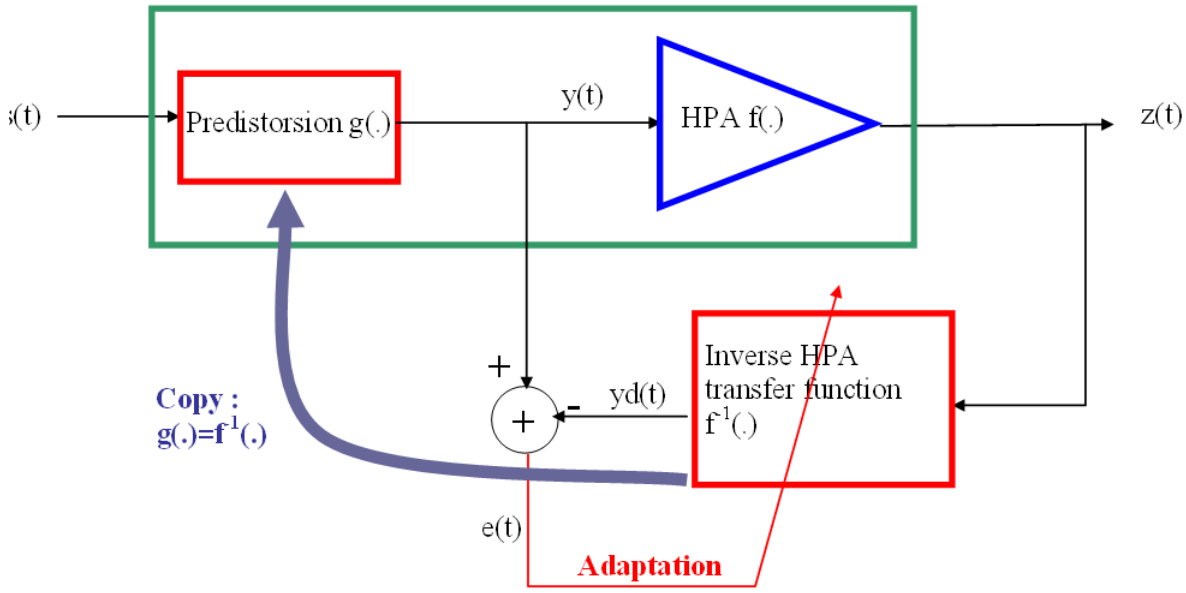


Figure 6-6: Indirect adaptation of the predistorsion function $g(.)$.

In the following we will present a predistortion for FBMC signals based on NN. Nevertheless, it has to be noted that other NL devices (Volterra, etc.) could be used based on the same methodology and architecture for the predistorter.

6.2.1 Basis of neural network predistortion

Neural networks are able (with sufficiently neurons and sufficiently hidden layers) to implement any kind of NL function. This property is known as "universal approximation theorem" [84, 85]. It is thus possible with NN to implement function $g(.)$ for predistortion.

Various NN architectures exist: Multi Layer Perceptron (MLP), Radial Basis Function (RBF) Kohonen Maps, etc. For our predistorter we will use an MLP based NN. These NN have shown their ability in predistorting high PAPR signals [6, 86].

The MLP architecture is given by figure 6-7 (a) and 6-7 (b). In the first figure, a single neuron is presented with N inputs $[x_1, x_2, \cdots x_N]$ and one output y. b is an additive bias and

$\Psi(.)$ is an activation NL function. This activation function is generally a sigmoid or hyperbolic tangent function with a "S" curve. Sigmoid function is given by : $\Psi(x) = \frac{1}{1+e^{-x}}$. Weights W_1 to W_N and bias b are adapted in order to reach the desired NL function.

The MLP is an association of neurons as shown on figure 6-7 (b) with a input layer of size p, two hidden layers and an output layer of size N.

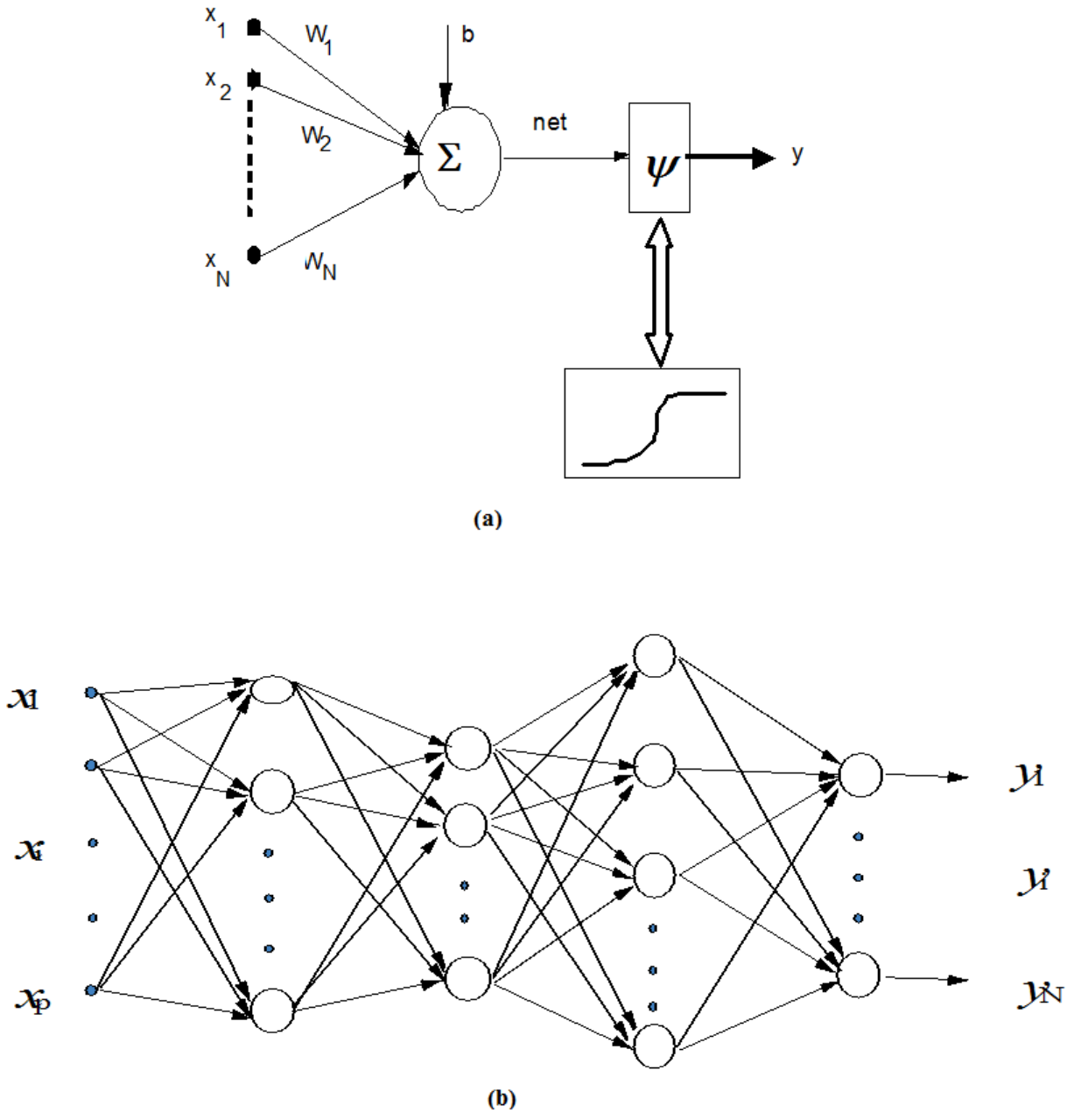


Figure 6-7: (a) Single Neuron, (b) Multi Layer Perceptron.

Generally, for complex I/Q signals, the input layer has a size equal to two (I and Q components) and the output layer is also with size equal to two (Id and Qd output signals after predistortion. Even if the "universal approximation theorem" is based on an infinite number

of hidden layers and neurons, simulations have shown that a reasonable number of neurons had to be used in order to have good predistrotion results [6]. A single hidden layer with tens of neurons is generally sufficient to generate the right predistortion function $g(.)$.

Using the indirect adaptation method (see figure 6-6), figure 6-8 gives the architecture of the MLP for predistortion purposes. HPA signal $z(t)$ is fed into the NN and the output of the NN-MLP is compared to the input signal, $y(t)$, of the HPA. An adaptation algorithm is then used for minimizing the mean square error of $e(t)$.

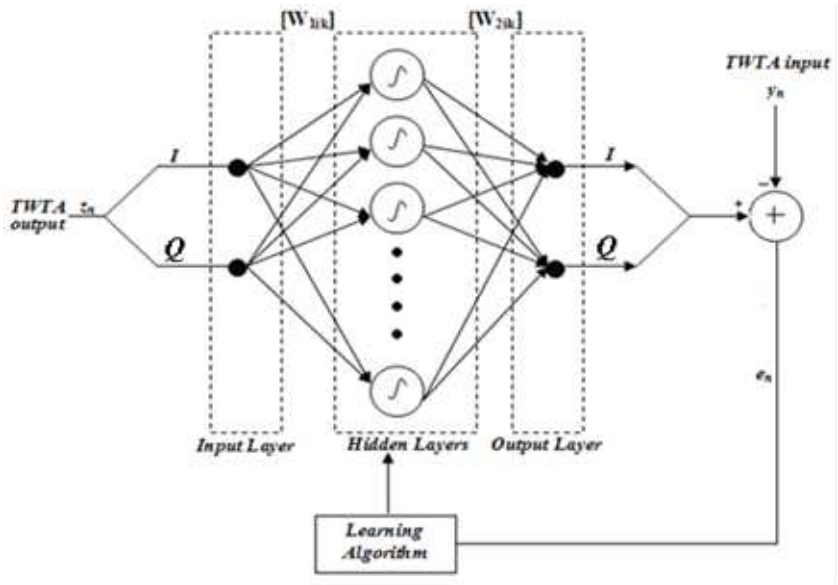


Figure 6-8: Multi Layer Perceptron for predistorsion.

Various training/adaptation algorithms are available in literature. Among them we can list: Gradient Descent backpropagation (GD), Gradient Descent backpropagation with the momentum (GDm), Conjugate Gradient BP (CGF), Quasi Newton (BFG) and Levenberg Marquardt (LM). A more detailed description of these algorithms is available in [6]. For OFDM predistortion, LM algorithm has been proved to be superior to the other ones for convergence speed and for the same computation complexity.

In the following, we will implement predistortion with NN-MLP with two real inputs (I and Q signals) and two real outputs and one hidden layer. The activation function will be a sigmoid and the LM algorithm will be used for adaptation of the weights and biases of the neurons. Computation of NL function $g(.)$ is done using the inverse adaptation method of figure 6-6.

6.2.2 Neural network MLP predistortion for FBMC

For building the predistortion function we have used two architectures. The first one is directly derived from the OFDM case. This architecture is given on figure 6-6. The HPA output complex signal is divided in real $(I(t))$ and imaginary part $(Q(t))$ that are fed to a NN-MLP as in figure 6-8. The two output signals $Id(t)$ and $Qd(t)$ are combined to form $yd(t)$. $yd(t)$ is compared to $y(t)$ and the weights and biases of the NN are adjusted in order to minimize the mean square error. As we will see on simulation results, this architecture presents a penalty when an FBMC signal is used instead of an OFDM one.

The difference between OFDM and FBMC relies on the fact that a phase error in the predistortion function $g(.)$ has a greater influence on FBMC compared to OFDM [87]. For

FBMC signals it is thus very important to have a predistortion function as close as possible to the one of a SEL. In order to guarantee that the phase of the output NN-MLP signal will be compatible with a SEL we have implemented a second architecture that is shown on figure 6-9. A NN-MLP with two real inputs and two real outputs is in charge of generating the inverse AM/AM transfer function $(F_a(.))$ and an other one is in charge of the AM/PM inverse function $(F_p(.))$. Even if the modulus of the input signal is higher than $\sqrt{P_{sat}}$ the phase will be correctly corrected.

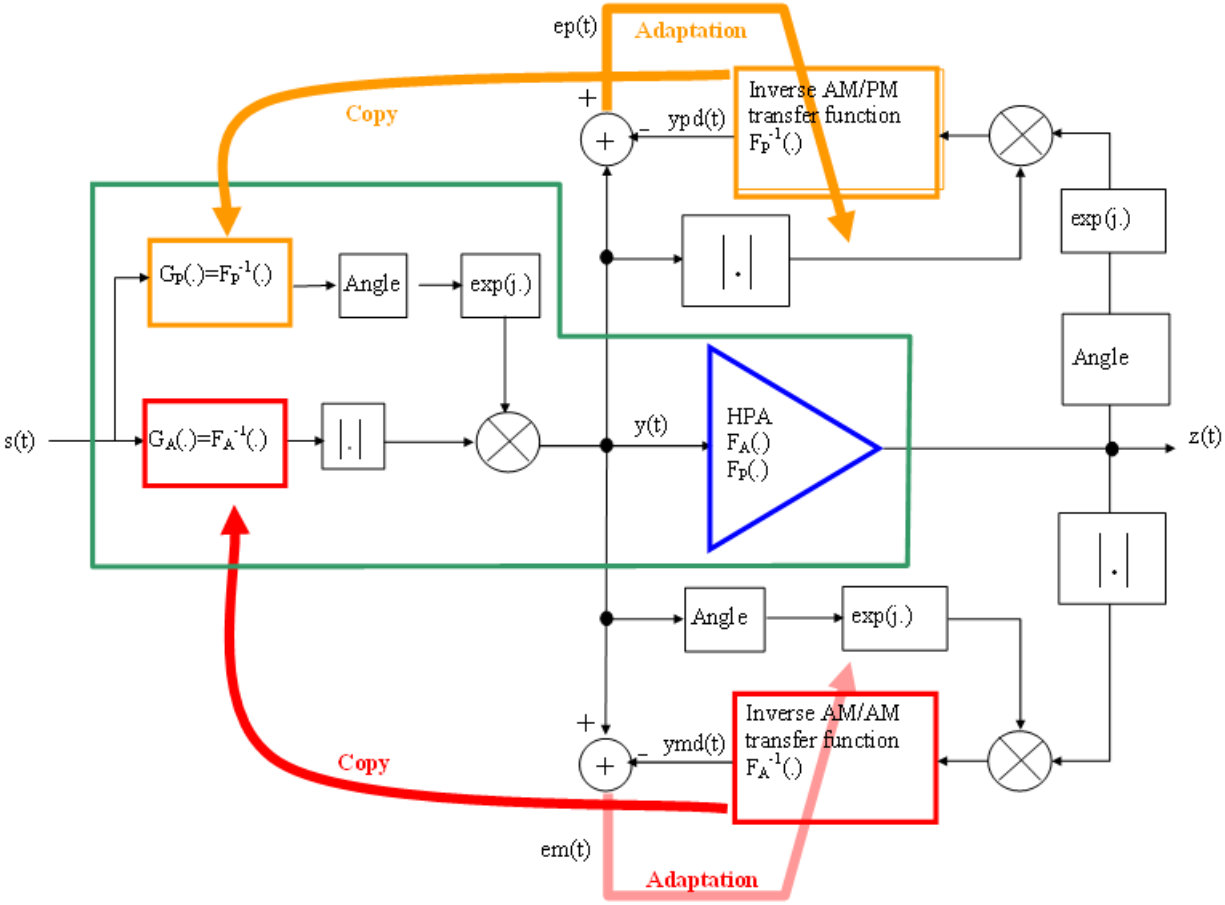


Figure 6-9: Modified NN-MLP architecture for FBMC predistorsion.

Simulations of predistortion have been realized. A complex baseband FBMC and OFDM signals with $N = 64$ subcarriers using 10^6 randomly generated symbols has been considered. An Additive White Gaussian Noise channel model (AWGN) has been used to clearly observe the effect of nonlinearity and performance improvement by the considered $NN - MLP$ of figure 6-9. For the FBMC system, we recall that we use the PHYDYAS prototype filter with an overlapping factor of 4 [87]. For the NL HPA model, we have considered a Saleh's model [4] with AM/AM and AM/PM conversions. The AM/AM and AM/PM conversions of this HPA model are given by equation 2.9. The values for parameters are assumed to be: $\alpha_a = 2$, $\beta_a = 1$, $\alpha_p = 4$ and $\beta_p = 9$.

We have presented the performance of the two NN-MLP architectures in figure 6-10 and 6-11 in terms of BER. In figure 6-10, the performances of the two modulations (OFDM and FBMC) are plotted without predistortion. It has to be noted that, because of the AM/PM

phase rotation, FBMC suffers more than OFDM. When a single NN-MLP is used (figure 6-10) FBMC performance is still worse than the OFDM one. In figure 6-11, the performances of the two modulations (OFDM and FBMC) are plotted with a predistortion system based on two NN-MLP as in figure 6-9. Using this architecture, FBMC and OFDM reach exactly the same performance.

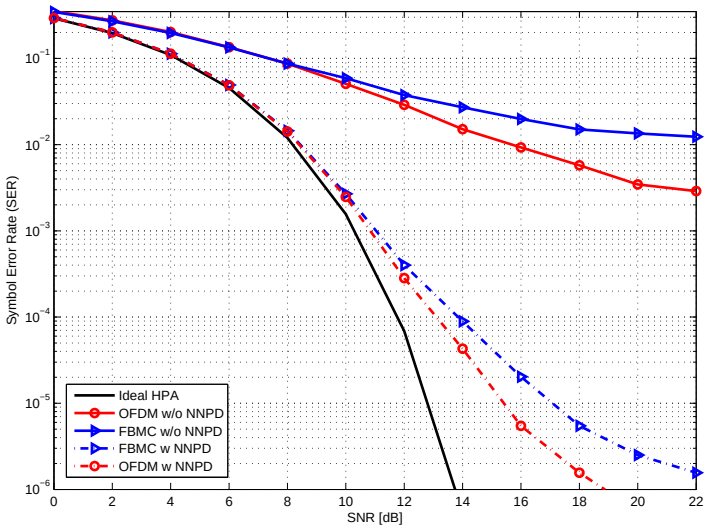


Figure 6-10: Performance of the first architecture based one a single NN-MLP.

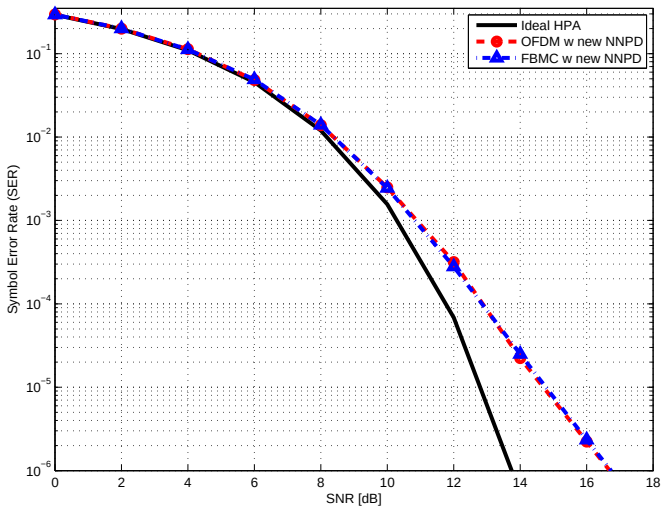


Figure 6-11: Performance of the second architecture based on two NN-MLPs for modulus and phase.

6.3 Linearized HPA performance limits

Digital predistortion is a widely studied method for linearizing power amplifiers, along with envelope tracking based highly linear HPAs. Any linearized power amplifier has anyway a saturation level for the output power. Therefore, the SEL model may be considered as a model for an ideally linearized HPA. With SEL model (or limiter model), we mean a linear transfer characteristic up to the saturation level (see subsection 2.3.1). Another commonly used basic HPA model, with AM/AM conversion only, is the Rapp model (see subsection 2.3.2). The commonly chosen value $p = 2.25$ will used in the following.

Here we consider the HPA effects, in terms of spectral regrowth, for the FB-SC waveform discussed in subsection 5.7.1 and the FBMC waveform with or without the tone reservation based PAPR mitigation method of subsection 5.7.2. The PSD plots of this subsection are obtained using the pwelch function of Matlab. Figure 6-12 shows the PSDs for different FB-SC roll-off factors with the two HPA models considered (SEL and Rapp with $A_{Sat} = 1$ and $p = 2.25$). It can be seen that the SEL model gives clearly lower spectral regrowth. For each SC bandwidth, the IBO value has been chosen in such a way that the spectral regrowth with clipping model is small, no more than 3 dB, and close to the same in all the cases.

Then figure 6-13 and figure 6-14 show the spectral regrowth for the FBMC scenario explained in section 5.7.2, for SEL model and Rapp HPA model, respectively, and with or without TR based PAPR mitigation. Targeting at keeping the spectral regrowth in the spectral gap in the order of 2-3 dB, we can conclude from these results that:

- With the SEL HPA model, 8 dB IBO is needed when the TR based PAPR mitigation is applied and about 10 dB IBO is needed without PAPR mitigation.
- With the Rapp HPA model, about 14 dB back-off is needed; the PAPR mitigation provides hardly any benefit in this case from the spectral regrowth point of view.
- Comparing FBMC without PAPR mitigation with FB-SC in the case of 72 subcarriers, we can see about 3.5 dB benefit for FB-SC in the needed back-off in the QPSK case and over 2 dB benefit in the 64QAM case, when well-linearized HPA is used. When comparing FBMC with TR based PAPR mitigation with FB-SC in the same scenario, there is still a benefit of about 1.5 dB for FB-SC with QPSK, but in the 64QAM case the difference becomes small.

6.4 Envelope tracking based HPA linearization

In section 4.3, we provided simulation-based comparative evaluation of several multi-carrier formats with the conventional OFDM under presence HPA modeled by the Rapp output-to-input relationship [3]. The comparison criterion was the attainable spectral efficiency while still fitting the 1.4 MHz LTE, UL PSD mask. In this section, the power efficiency will be accounted for through the recently actualized signal envelope controlled HPA supply voltage, the so-called envelope tracking amplifier [88]. Within the latter, the ability of the various multi-carrier waveforms to exploit such a mechanism under the limitation of supportable bandwidth of the available DC-to-DC converter technology will be emulated by additional filtering of the signal envelope.

In this Section we assume that the voltage saturation level (A_{sat}) of the NL HPA is controlled by normalized signal envelope as shown in figure 6-15. The consequence of

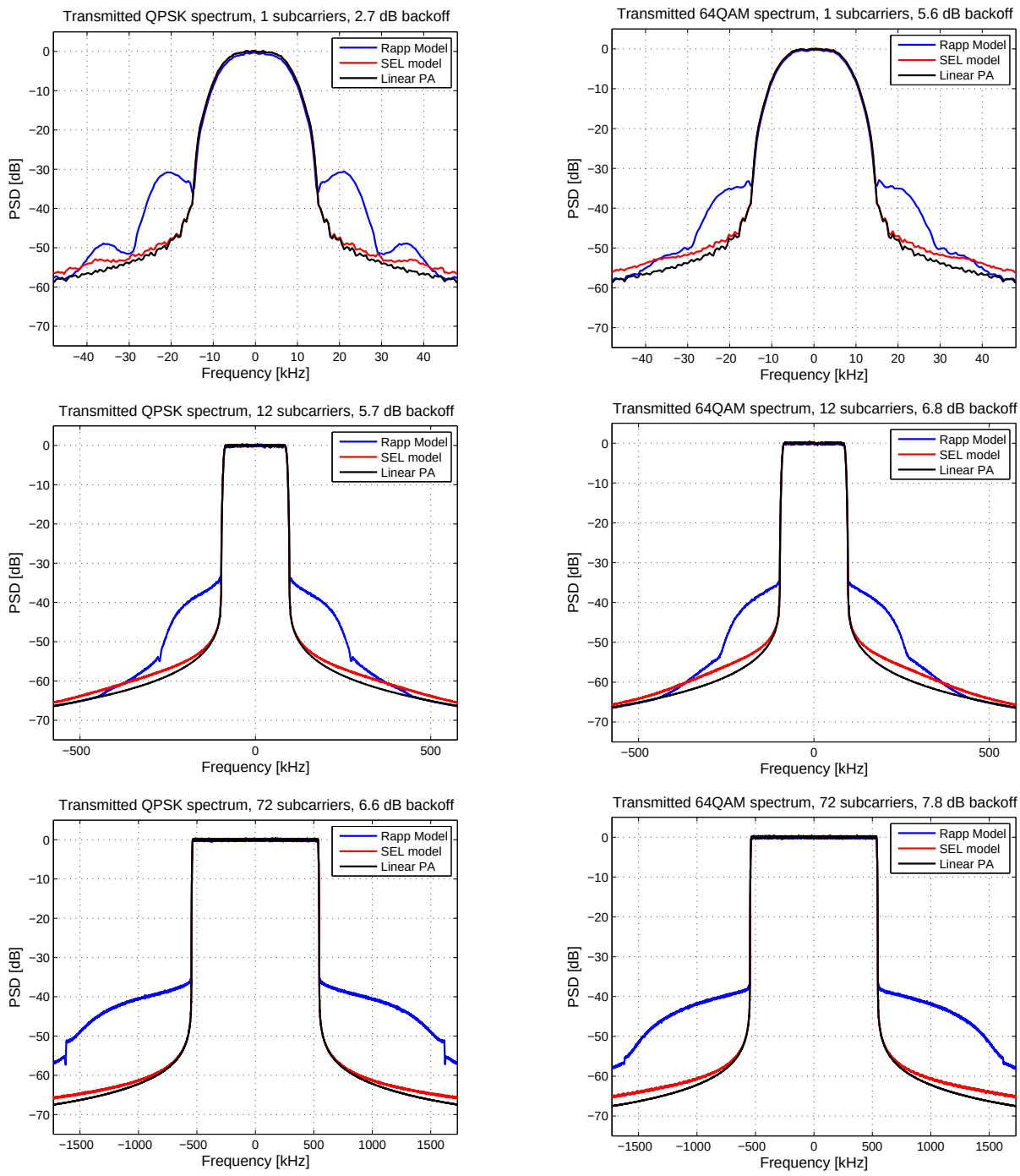


Figure 6-12: Spectral regrowth for FB-SC waveform with QPSK and 64QAM modulations, different bandwidths and roll-off factors using Rapp (p=2.25) and SEL models for HPA.

this modification was adaptive NL distortion to input signal level. It should be noted that the change of A_{sat} in the Rapp model impacts the linear amplification as well.

Figure 6-16 shows the PSDs for the adaptive HPA model from figure 6-15, for uniform and non-uniform configurations from the section 4.3.

The PSD variation in the pass-band region is related to non-symmetry of the sub-channels spectra for the Nu-TLO case. As it can be seen from figure 6-16, for the both uniform

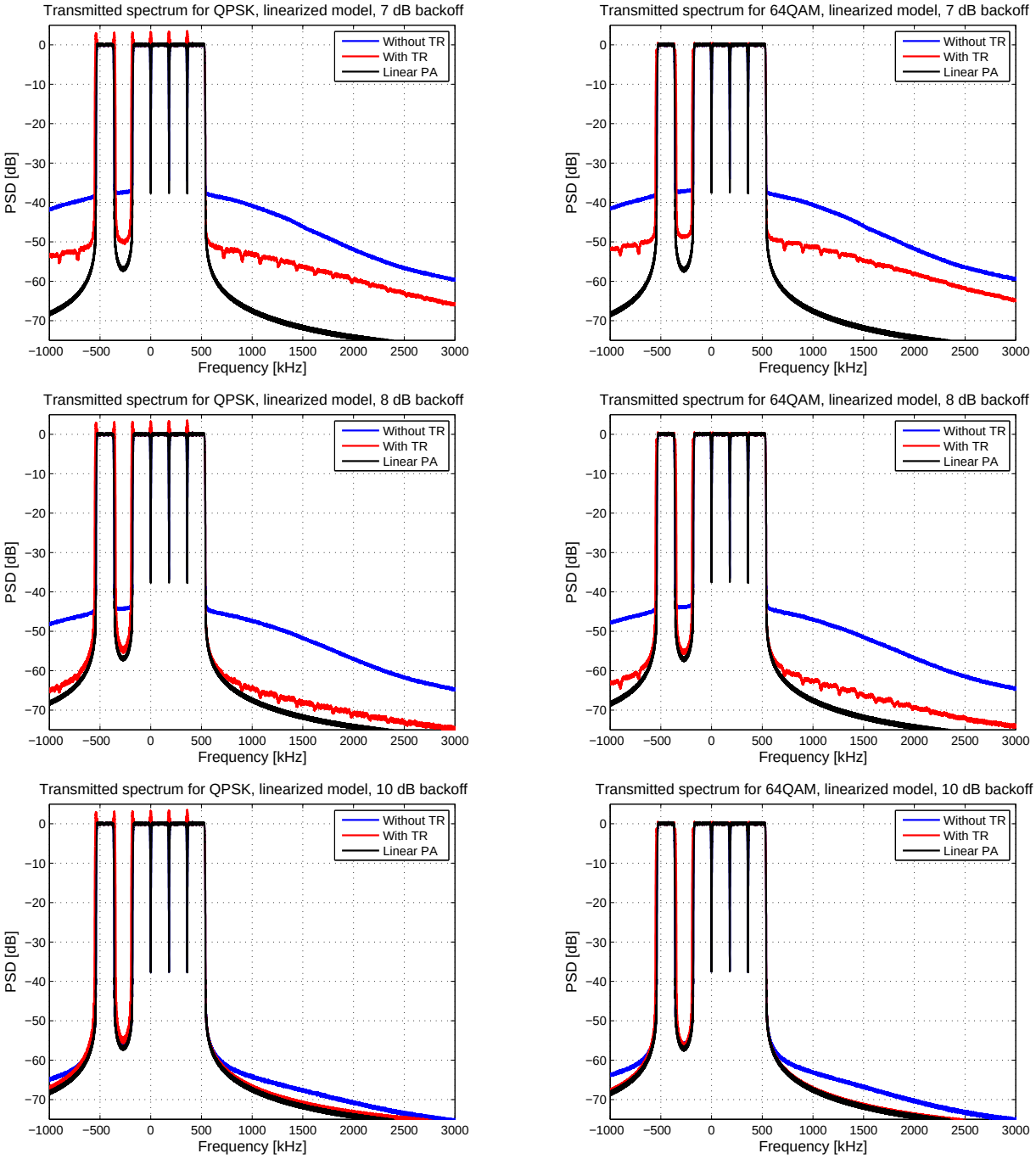


Figure 6-13: Spectral regrowth with 1.4 MHz LTE-like FBMC waveform with QPSK and 64QAM modulations and different back-off values using SEL HPA model with or without TR based PAPR mitigation.

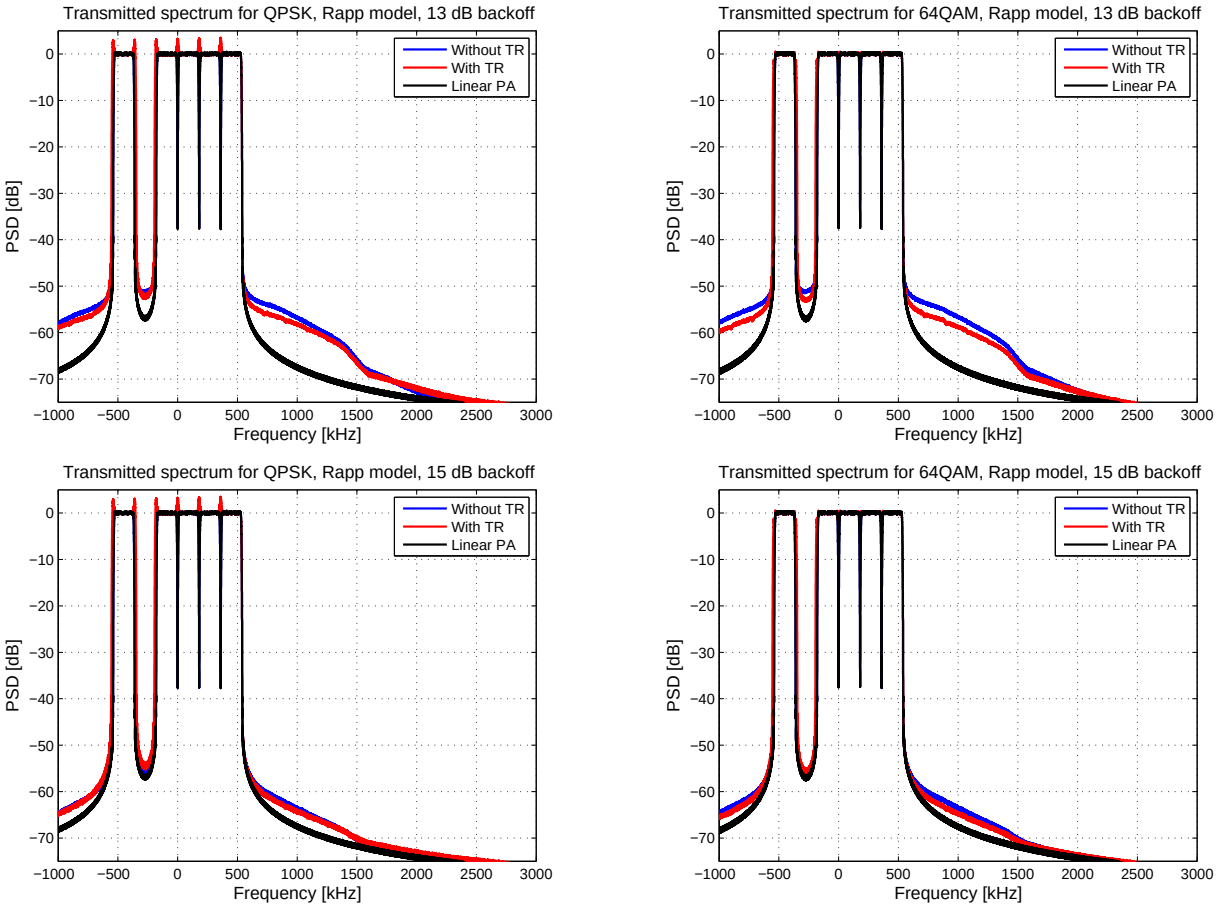


Figure 6-14: Spectral regrowth with 1.4 MHz LTE-like FBMC waveform with QPSK and 64QAM modulations and different back-off values using Rapp HPA model (p=2.25) with or without TR based PAPR mitigation.

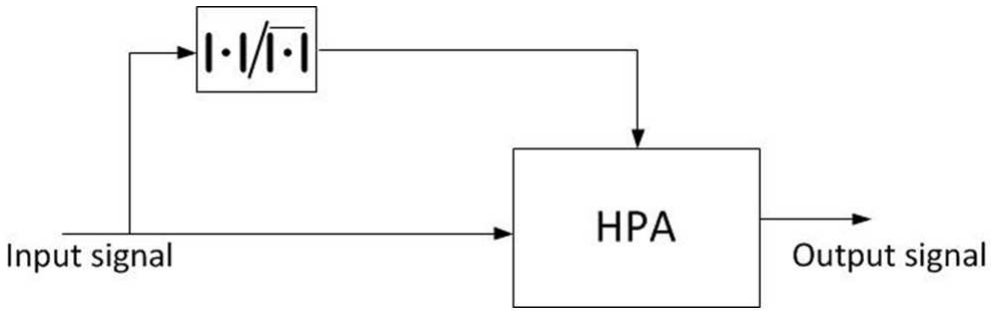


Figure 6-15: The NL HPA model controlled by normalized signal envelope.

and non-uniform configurations, impact of the NL distortions is significantly suppressed: the PSDs of amplified i.e. distorted signals are slightly raised in comparison with PSDs of undistorted signals.

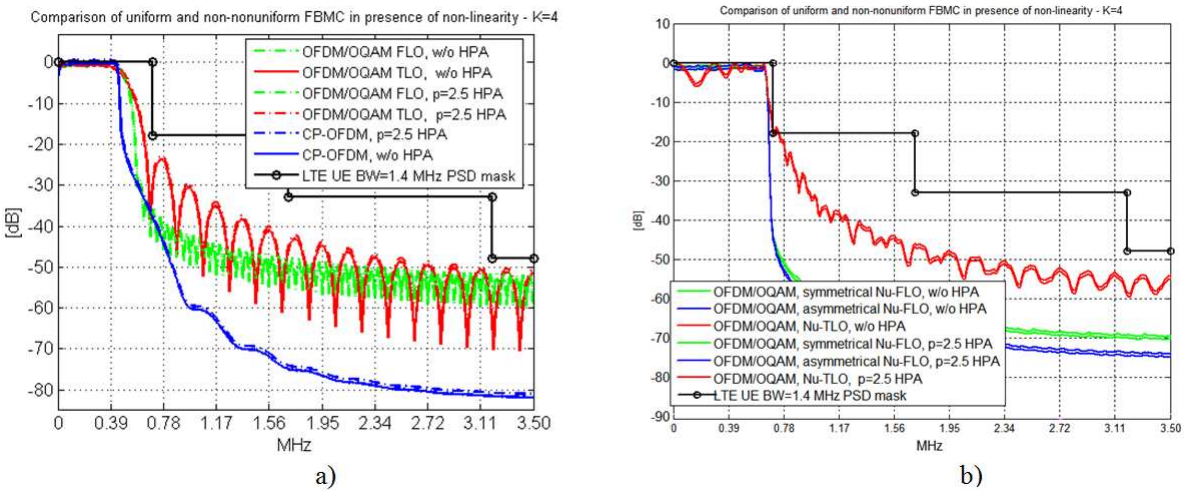


Figure 6-16: Performance comparison for HPA controlled by signal envelope: (a) CP-OFDM, uniform-FLO/TLO FBMC configurations, and (b) symmetrical Nu-FLO FBMC, asymmetrical Nu-FLO FBMC and Nu-TLO FBMC configurations for the maximum fitting of the PSD mask.

6.4.1 Sensitivity to bandwidth limitations of DC-to-DC converter technology

In order to emulate bandwidth limitations the control of NL amplifier is done by filtering envelope of input signal according to block diagram depicted in figure 6-17.

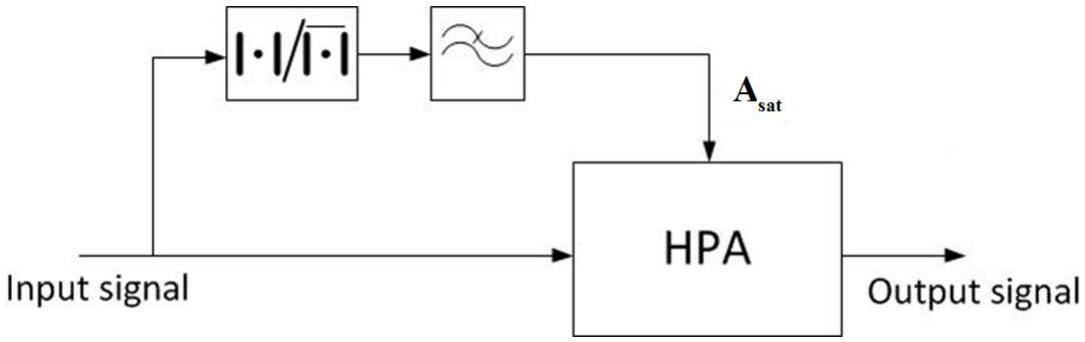


Figure 6-17: The NL HPA model controlled by filtered normalized signal envelope.

The only difference to figure 6-15 is the insertion of the low-pass filter which is used to pass 1/2, 1/4 or 1/8 of the signal bandwidth. The PSDs of filtered envelope signals are shown in figure 6-18-a) and figure 6-18-b) for the cases of uniform and Nu FBMC arrangements, respectively.

In figures 6-19-a), 6-19-b) and 6-19-c) are shown the PSDs for the case HPA model shown in the figure 6-17 for uniform configurations for three different values of filter cutoff frequency: 1/2, 1/4, and 1/8 of signal envelope bandwidth.

In figure 6-20 are shown the power spectral densities for the case of HPA model shown in figure 6-17 for non-uniform configurations for three different values of cutoff. (1/2, 1/4, 1/8).

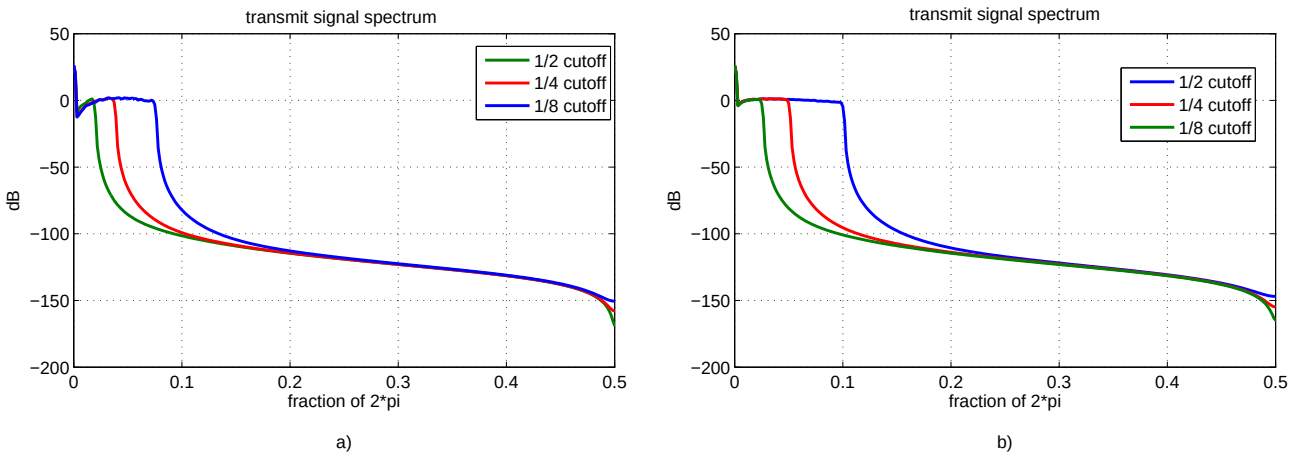


Figure 6-18: Transmit signal spectrum cutoff for uniform configuration (a), and non-uniform configuration (b) with oversampling factor 5:1.

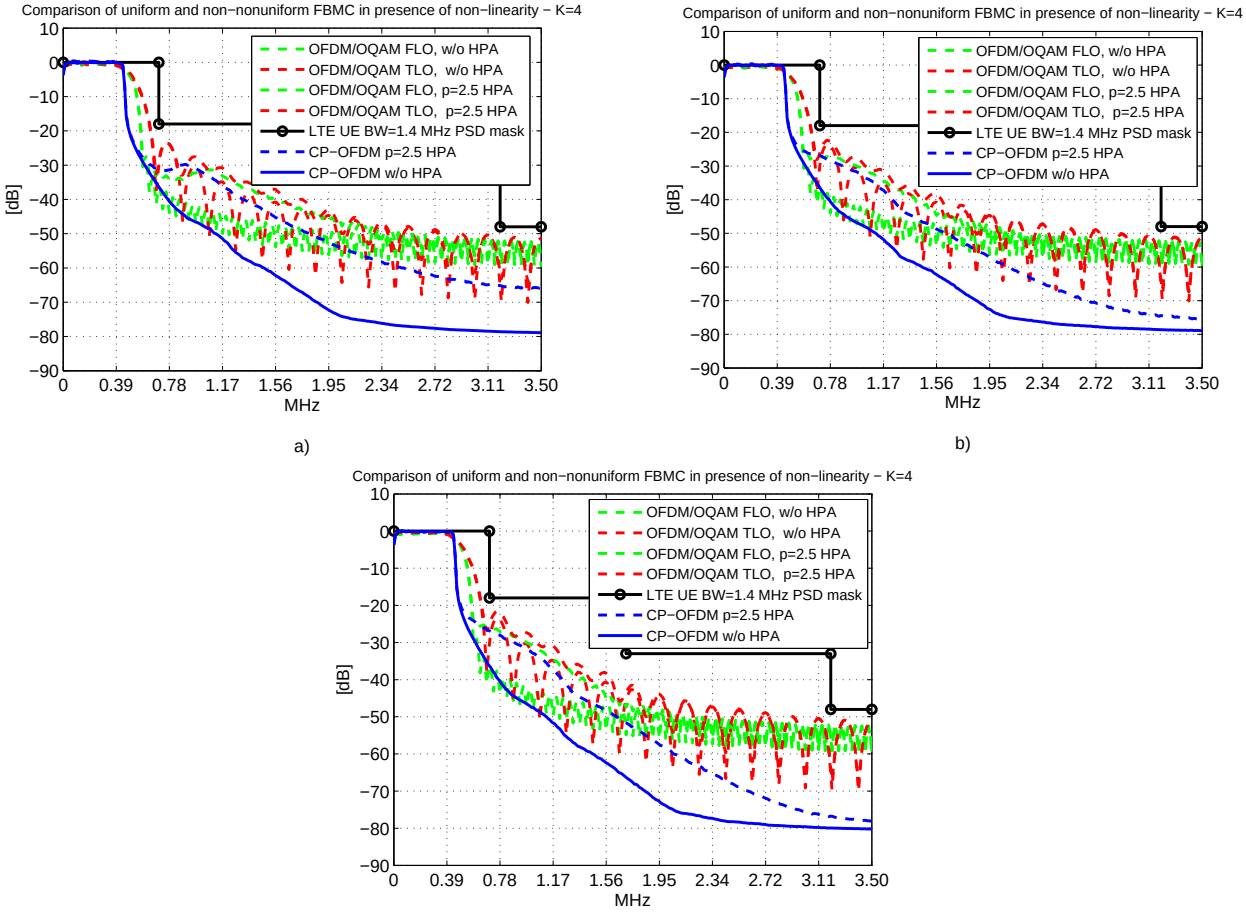


Figure 6-19: Comparison of uniform FLO FBMC, TLO FBMC and CP-OFDM in context of HPA and mask fitting with transmit signal spectrum cutoff; a) 1/2 spectrum cutoff, b) 1/4 spectrum cutoff c) 1/8 spectrum cutoff, with oversampling factor = 5.

It can be noticed from figure 6-19 and figure 6-20 that the more we "cut" signal envelope spectrum, level of side lobes is increased.

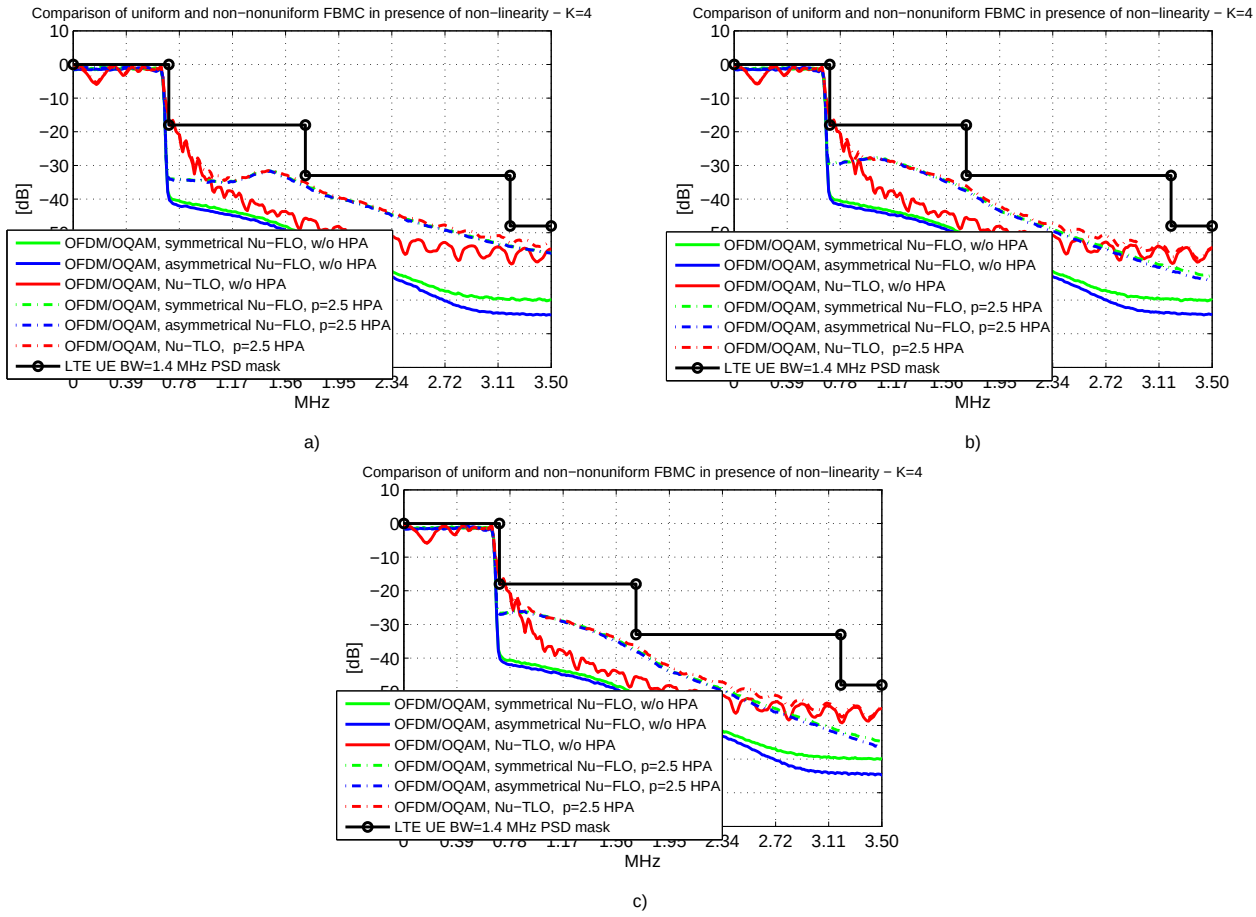


Figure 6-20: Comparison of non-uniform FLO FBMC, TLO FBMC and CP-OFDM in context of HPA and mask fitting with transmit signal spectrum cutoff; a) 1/2 spectrum cutoff, b) 1/4 spectrum cutoff c) 1/8 spectrum cutoff.

6.4.2 Conclusion

The conducted evaluation of spectral efficiency of various multi-carrier waveforms, carried in section 4.3, has demonstrated the advantage of non-uniform over uniform FBMC formats and over the OFDM. This is contingent on the correctness of the selected HPA model jointly with the practical aspect of HPA implementation. In this section the evaluation was applied for the method of HPA "linearization", whereby in the conducted evaluation the variation of output saturation level has influenced the amplification factor. This has to be avoided or at least reduced, depending on the HPA implementation aspects (the accompanying class changes, etc.), since the impact should be the more relevant, the larger discrepancy between the filtered and non-filtered envelope exists.

6.5 Measurements and performances on real HPA hardware

6.5.1 Introduction

Of course, the spectrum containment enhancements and optimizations brought by the multicarrier filtering approach is self evident (from a spectral point of view). This is still

valid whatever the considered filter bank modulation scheme (FBMC, FMT, $\cdots$). As we have described in previous deliverables and chapters, the use of filter bank modulation schemes provide far higher adjacent power rejection close to the edge subcarriers compared to OFDM. Of course, we have also seen that linearization shall apply in order to be able to take benefit of this advantage. One could imagine in the digital world to specify and achieve quite huge spectral rejections. This could lead to over specifications as the RF analog part will limit the final performances for the whole system. In this section, we propose to apprehend the spectral regrowth that a real HPA will cause. We will use several waveform patterns (with different levels of spectral purity) in order to highlight the HPA HW limitations (of course, HPA linearization algorithms will be running in order to improve the overall performances).

6.5.2 Considered FMT scheme

We consider the FMT scheme and parameters described in the dedicated paragraph in document D2.1, related to FMT approach. Please refer to this deliverable, and more particularly to the FMT approach dedicated chapter for detailed description of the considered waveform. For practical implementation, we have used the temporal representation of the filter. Classical OFDM modulation is performed, including IFFT processing, and then, at the very final modulation processing stage, the pulse shaping filter is added. The filter length is chosen to be a multiple of the OFDM symbols (and so a multiple of $N+CP$ samples $= L(N+CP)$). As a consequence, the temporal filter shape is applied to those buffered OFDM symbols, with overlapping and add processing for successive OFDM symbols. The impulse response of the prototype filter used in the FMT scheme is given by

$$g(t) = \begin{cases} 1-\alpha+4\frac{\alpha}{\pi} & \textit{if } t=0 \\ \frac{\alpha}{\sqrt{2}}\left[(1+\frac{2}{\pi})\sin(\frac{\pi}{4\alpha})+(1-\frac{2}{\pi})\cos(\frac{\pi}{4\alpha})\right] & \textit{if } t=\pm\frac{T}{4\alpha} \\ \frac{\sin[\pi\frac{t}{T}(1-\alpha)]+4\alpha\frac{t}{T}\cos[\pi\frac{t}{T}(1+\alpha)]}{\pi\frac{t}{T}[1-(\frac{4\alpha t}{T})^2]} & \textit{elsewhere} \end{cases} . \quad (6.3)$$

where α is the roll-off factor, which determines the width of the transmission band at a given symbol rate.

The rejection performances depend on the shape of the filter used. A filter with a high number of coefficients brings better precisions, rejection and nice spectrum windowing. However, the high number of samples necessary for obtaining such a result at the filtering output generates huge time delays. In that way, the latency added by the user of such a filtered LTE signal has to be taken into account in the design of the pulse-shaping function. The goal will be to limit the additional delay, and thus, we will have to achieve the best possible performances, with the shortest filter in terms of number of coefficients. To remind, we derived parameters from 3GPP LTE standard, and we added 2 additional parameters (temporal pulse shaping filter support and roll-off factor) as depicted in table 6-1.

As described in details in document D2.1, the pulse shaping filter used in this FMT scheme is a classical square root raised cosine filter applied in the frequency domain. In addition, the frame structure and frame formatting used in order to perform the analysis

Configuration parameters	FMT derived from LTE
Basic modulation access mode (LTE)	OFDMA (downlink mode)
Carrier frequency (PMR case)	450 MHz
Bandwidth (LTE)	1.4 MHz
FFT size (LTE)	128
Sampling Frequency (LTE)	1.92 MHz
Sub-carrier spacing (LTE)	15 kHz
CP (LTE)	$N \times 512/2048 = 1/4$
Symbol duration (LTE)	160 samples: $N + CP$
Number of used sub-carriers (LTE)	72 (6 RBs)
Pulse shaping filter size in samples (FMT)	$L \times (N + CP))$ with L = 12
Roll-off factor (FMT)	$\alpha = 0.25$

Table 6-1: Specified parameters

corresponds exactly to the 3GPP LTE standard release 8 features. The various physical channels and pilots (Reference Signals) configurations implemented in the simulation are compliant with the standard.

6.5.3 Waveform descriptions

As described previously, we will use the FMT waveform as defined in the deliverable D2.3. We will also vary the pulse shaping filter length in order to generate FMT waveform with different spectrum rejection results in order to visualize the HPA final effects from a spectral point of view. We are considering RB blanking (blocks of 12 sub-carriers are totally blanked: RS included). Several waveforms are generated with the following characteristics:

- Fs = 7.68 Msamples/s.
- No Crest Factor reduction is applied (as a consequence, PAPR is roughly 12dB).
- Modulation : 64QAM.
- BW = 1.4MHz (6 RBs).
- Two RBs are blanked.
- **First waveform** with L = 6, roll-off = 0.25 (this corresponds to ACP rejection around 40dB).
- **Second waveform** with L = 12, roll-off = 0.25 (this corresponds to ACP rejection around 60dB). This is nearly the waveform retained after D2.1 study.
- **Third waveform** with L = 24, roll-off = 0.25 (this corresponds to ACP rejection around 70dB). This waveform has been used just to validate that we were not limited by our test bench setup.

Nota: while up-sampling to $7.68\ Msamples/s$, a channel filtering is also applied to clean the spectrum outside the $1.4\ MHz$ channel bandwidth.

6.5.4 Test bench

In order to clearly highlight the HPA equipment performances, the waveforms considered are then converted into two formats: the one needed for the Base Station (BS) baseband unit, and the other format to feed an $R\&S\ SMU200$ vector signal generator. Given those two formats, we will be able to measure the real performances achievable with the digital waveform using the SMU200 test bench as a reference, and then superimpose real life performances at the output of the HPA under test (at maximum power output value $= +48$dBm $\approx$ 60W). We will then see degradations brought by the HPA at spectral output of the whole BS RF chain.

6.5.5 Theoretical spectrums

As a result, we theoretically have the spectrum given by figure 6-21. In this figure, we have :

- In black : the Classical OFDM case,
- In red : the first waveform,
- In blue : the second waveform.

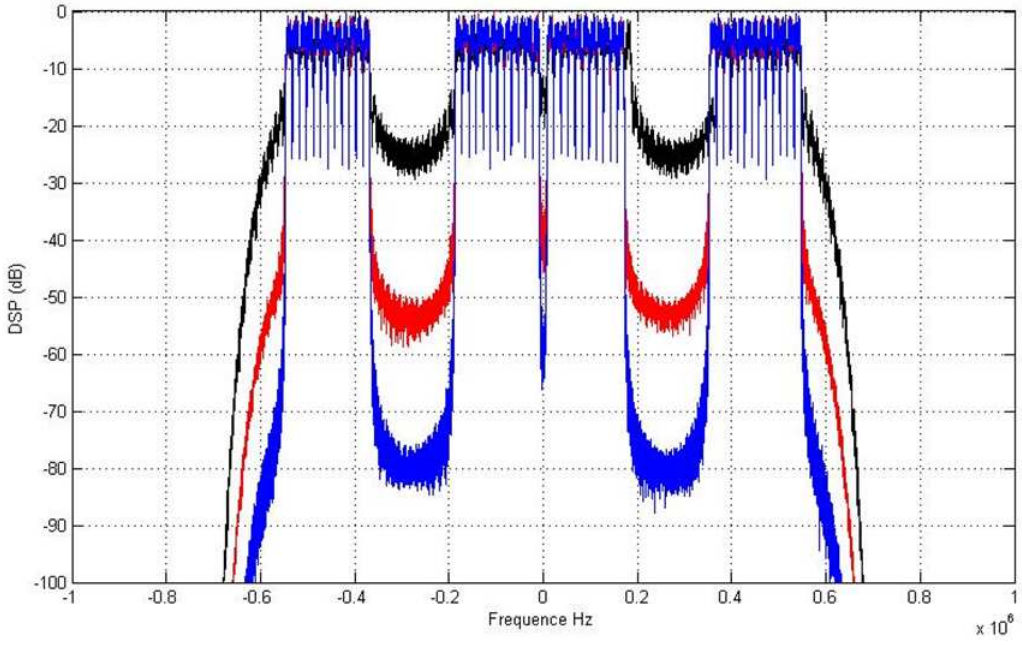


Figure 6-21: Theoretical PSDs of the three considered waveforms. OFDM in black, first FMT waveform in red and second FMT waveform in blue.

6.5.6 Measurements results

By using the hardware test bench, we have the plots shown in figure 6-22, 6-23 and 6-24 for the three considered waveforma. In these figures :

- The blue curve is the one measured at HPA base station output,
- The black curve is the one measured at $R\&S\ SMU200$ output (reference measurement).

6.5.6.1 First waveform

Using those pulse shaping parameters allows us to greatly improve adjacent subcarrier rejection (around $40dB$ approximately), and both curves (SMU200 and HPA) are similar in the blanked RBs. As a consequence, with implemented HPA linearization algorithms, we fully benefit from the pulse shaping enhancements.

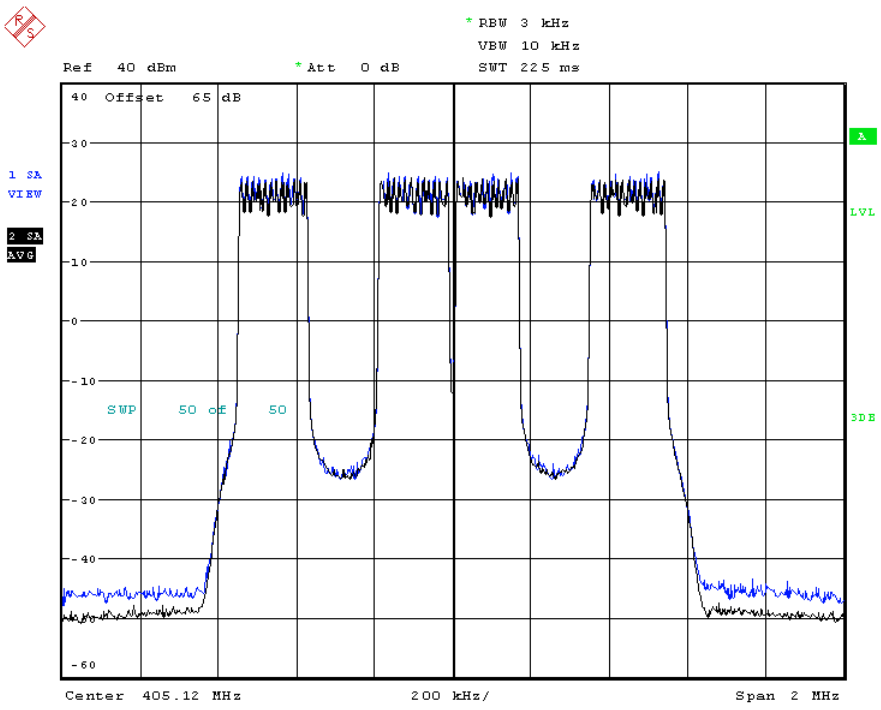


Figure 6-22: First waveform measured PSDs. At HPA base station output in blue and at $R\&S\ SMU200$ output in black.

6.5.6.2 Second waveform

On the contrary, in this case, the linearization algorithm and RF chain characteristics do not allow us to benefit form the complete rejection dynamic of the pulse shaping enhancements, but we are relatively close to the SMU200 reference curve. This shows us the limit of the considered base station hardware. We do not need to specify stringent and additional constraints from a digital point of view, because it will not improve the performances at the end.

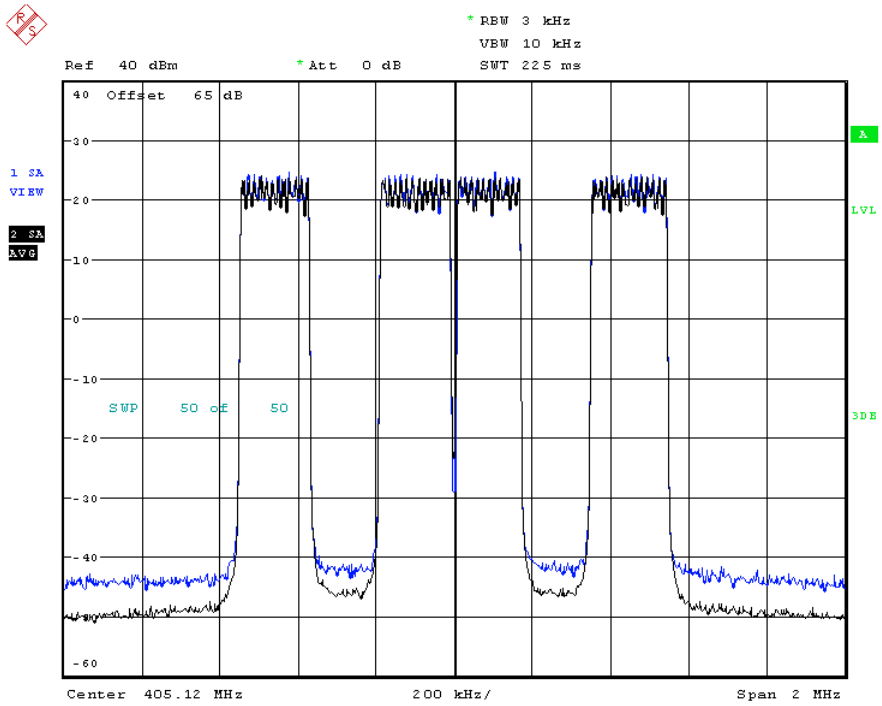


Figure 6-23: Second waveform measured PSDs. At HPA base station output in blue and at $R\&S\ SMU200$ output in black.

6.5.6.3 Third waveform

Using this third waveform, we can see that this time, we are reaching our test bench limitations. We are not able to benefit from the whole $70dB$ of rejection with $R\&S$ SMU200 reference vector signal generator either. We could see that the spectrum is still improved at the very base of the carriers compared to the previous case, but the floor remains identical.

6.5.6.4 Conclusion

As a first estimate, we clearly see that BS HPA equipment is able to output FMT waveform (using pulse shaping modulation) with blanked RBs with nearly $60dB$ of rejection. This is a first result, and of course, the same study should also be performed with mobiles and UEs. The goal was not to dimension the whole system (including BS and UEs), but only to reassure ourselves by testing the considered waveforms on real HW. We could see that our hypotheses are confirmed in the way that the desired and considered rejection shall be applicable in the real life.

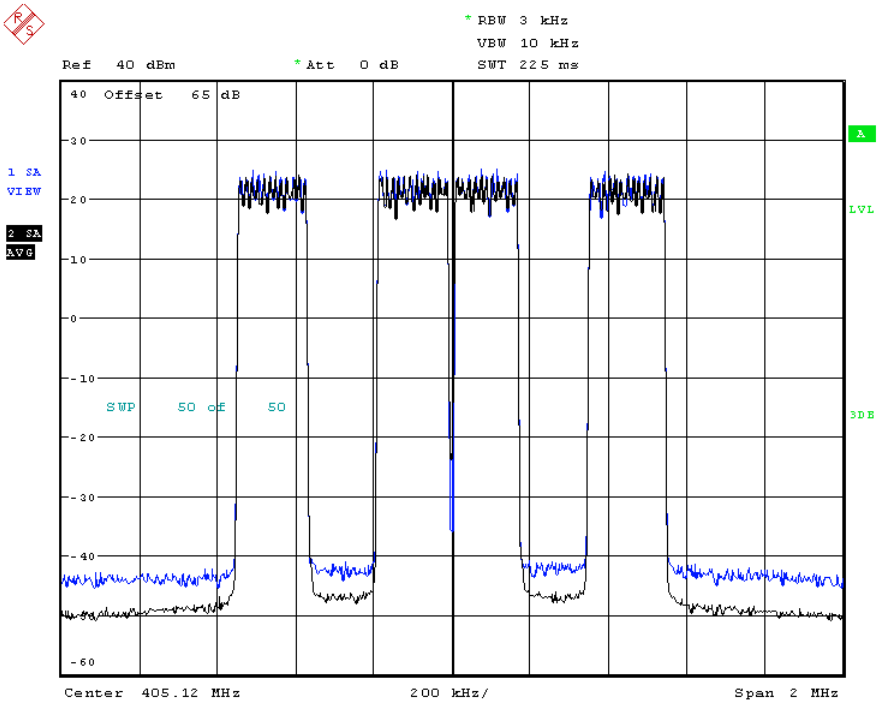


Figure 6-24: Third waveform measured PSDs. At HPA base station output in blue and at $R\&S$ $SMU200$ output in black.

7. Conclusion

A theoretical approach was developed to evaluate the effect of NL HPA induced in-band distortion on the BER performance of OFDM and FBMC systems. The in-band distortion is modeled by a complex gain and uncorrelated additive Gaussian noise, given by Bussgang's theorem. The parameters of the model are obtained from the HPA model through polynomial approximation. The approach is expandable to HPA models with memory. With memoryless HPA models, the developed theoretical model was found to agree well with simulations, and FBMC showed quite similar performance with OFDM in terms of BER.

Polynomial models were also used to characterize the spectral regrowth in the transmitted FBMC signals introduced by NL HPAs with different back-off values. For the prediction of the PSD, a generalized moments based formalism called cumulants was used. With cumulants, we can compute the auto-covariance function of the amplified signal, the Fourier transform of which leads to the PSD. Also the spectral efficiency of various multicarrier waveforms was evaluated, taking into account the spectral regrowth effects on the adjacent channel interference between the up-link transmissions. This evaluation demonstrated advantage of FBMC formats over conventional OFDM, as well as potential benefits for non-uniform over uniform FBMC formats.

Regarding PAPR mitigation for FBMC waveforms, a new SLM based scheme combined with trellis based approach for joint block optimization was proposed. With this TSLM scheme, FBMC outperforms OFDM with classical SLM in terms of PAPR reduction. While considering fast-convolution filter bank (FC-FB) based implementations of FBMC waveforms, it was found out that methods like SLM and PTS are not feasible. Nevertheless, tone reservation techniques were found to be applicable in FC-FB based implementations. FC-FB can be used for efficient implementation of single-carrier waveforms with very small roll-off factors and effective frequency-domain equalization on the receiver side. The PAPR characteristics of these FB-SC waveforms were found to be similar (but slightly better) than those of the OFDM based SC-FDMA.

Base band predistortion can be applied for FBMC signals. It has to be noted that the predistorter architecture must take into account the specific interference of this waveform compared to classical OFDM. For that purpose, a specific predistorter architecture has been used. This architecture consists of one predistorter bloc for AM/AM correction and another one for AM/PM correction.

The back-off requirements for FB-SC and FBMC waveforms were evaluated in the 1.4 MHz LTE-like scenario selected for the EMPhAtiC demonstrator development, while targeting at low level of spectral regrowth and about -60 dB out-of-band PSD level in adjacent non-active resource blocks. The soft envelope limiter model was used as a model for ideally linearized HPA. Compared with a basic solid-state HPA model (Rapp model with p=2.25), HPA linearization allows to reduce the IBO requirement for FBMC from about 14 dB to 10 dB when PAPR mitigation is not included or to about 8 dB with a basic PAPR mitigation scheme. When using the Rapp HPA model, PAPR mitigation brings hardly any benefit. In the full-band case with high-order constellations and well-linearized HPA, FB-SC has similar back-off requirement compared to FBMC with PAPR mitigation. With QPSK modulation, FB-SC has significant (about 1.5 dB) benefit.

The possibility of reaching about -60 dB PSD level in adjacent blanked RBs was also

demonstrated by real-life measurements, for FMT waveform with LTE-like parametrization, when using a HPA hardware meant for base-station use. One major challenge for future work is to reach the same with practical HPAs of mobiles and hand-held devices.

8. References

[1] P. Colantonio, F. Giannini, and E. Limiti. *High efficiency* RF *and microwave solid state power amplifiers*. J. Wiley, UK, 2009.

[2] H.E. Rowe. Memoryless nonlinearity with gaussian inputs: Elementary results. *The BELL system technical Journal*, 61(7), January 1982.

[3] C. Rapp. Effects of HPA nonlinearity on 4-DPSK-OFDM signal for digital sound broadcasting systems. In *Second European Conf. on Sat. Comm.*, October 1991.

[4] A.A. Saleh. Frequency-independent and frequency-dependent nonlinear models of TWT amplifiers. *IEEE Transactions on Communications*, 29(11):1715–1720, November 1981.

[5] G. Santella and F. Mazzenga. A hybrid analytical-simulation procedure for performance evaluation in M-QAM-OFDM schemes in presence of nonlinear distortions. *IEEE Transactions on Vehicular Technology*, 47:142–151, February 1998.

[6] R. Zayani, R. Bouallegue, and D. Roviras. Adaptive predistortions based on neural networks associated with levenberg-marquardt algorithm for satellite down links. *EURASIP Journal on Wireless Communications and Networking*, ID 132729:15 pages, 2008.

[7] G.T. Zhou. Predicting spectral regrowth of nonlinear power amplifiers. *IEEE Transaction on Communications*, 50:718–722, May 2002.

[8] R. Raich, H. Qian, and G.T. Zhou. Orthogonal polynomials for power amplifier modeling and predistorter design. *IEEE transactions on Vehicular Technologies*, 53:1468–1479, September 2004.

[9] P. Kenington. *High-Linearity* RF *Amplifier Design*. Artech House, Boston, 2000.

[10] M.I. Abdullah, M. Z. Mahmud, M.S. Hossain, and M.N. Islam. Comparative study of PAPR reduction techniques in OFDM. *ARPN Journal of systems and software*, 1:263–269, November 2011.

[11] Z. Kolar and P. Horvath. Physical layer consideration for radio cognitive: Modulation technique. In *IEEE VTC Spring*, May 2011.

[12] A. Skrzypczak, P. Siohan, and J. Javaudin. Analysis of the peak-to-average power ratio for OFDM/OQAM. In *IEEE SPAWC*, July 2006.

[13] D. Dardari, V. Tralli, and A. Vaccari. A theoretical characterization of nonlinear distortion effects in OFDM systems. *IEEE transactions on Communications*, 48(10):1755–1764, October 2000.

[14] J. Qi and S. Aissa. On the effect of power amplifier nonlinearity on MIMO transmit diversity systems. In *IEEE ICC*, pages 2891–2895, June 2009.

[15] J. Qi and S. Aissa. Analysis and compensation of power amplifier nonlinearity in MIMO transmit diversity systems. *IEEE Transaction on Vehicular technology*, 59:2921–2931, July 2010.

[16] B. Imre and V. Van. Central limit theorems for gaussian polytopess. *Annals of Probability*, 35:1593–1621, 2007.

[17] P. Siohan, C. Siclet, and N. Lacaille. Analysis and design of OFDM/OQAM systems based on filter bank theory. *IEEE Transactions on Signal Processing*, 50:1170–1183, May 2002.

[18] H. Bolcskei. Orthogonal frequency division multiplexing based on offset QAM. *Advances in Gabor Analysis*, pages 321–352, 2003.

[19] M.G. Bellanger. Spicification and design of prototype filter for filter bank based multicarrier transmission. In *IEEE International Confrence on Acoustic, Speech and Signal Processing*, pages 2417–2420, May 2001.

[20] A. Papoulis. *Probability, Random Variables and Stochastic Process*. 3rd ed. New York Polytechnic institute, New York, 1991.

[21] J.J. Bussgang. *Crosscorrelation functions of amplitude-distorted gaussian signals*. Research laboratory of electronics, Massachusetts Institute of Technology, Cambridge, 1952.

[22] S.C. Cripps. RF *power amplifier for wireless communications*. Artech House, MA, 1999.

[23] J.G. Proakis. *Digital Communications*. 5th ed. McGrawHill, New York, 2001.

[24] H. Bouhadda, H. Shaiek, D. Roviras, R. Zayani, Y. Medjahdi, and R. Bouallegue. Theoretical analysis of BER performance of nonlinearly amplified $\mathrm{FBMC/OQAM}$ and OFDM signals. *EURASIP Journal on Advances in Signal Processing*, doi:10.1186/1687-6180-2014-60 2014.

[25] A. Leon-Garcia. *Probability and Random Processes for Electrical Engineering*. Addison-Welsey, Cambridge, 1994.

[26] B.F. Boroujeny. OFDM versus filter bank multicarrier. *IEEE Signal Processing Magazine*, pages 92–112, May 2011.

[27] T. Ihalainen, T.H. Stitz, and M. Renforse. Channel equalization in filter bank based multicarrier modulation for wireless communications. *EURASIP Journal on Advances in Signal Processing*, 2007.

[28] C.L. Nikias and A.P. Petropulu. *Higher-Order Spectra Analysis*. Prentice-Hall, Englewood Cliffs, NJ, 1993.

[29] J. de Barbeyrac J. Stern and R. Pogg. *Methodes pratiques d'étude des fonctions aléatoires*. Editions Dunod, Paris, 1967.

[30] S. Salla, H. Shaiek, D. Roviras, and Y.Medjahdi. Analysis of the nonlinear spectral re-growth in FBMC systems for cognitive radio context. In *IEEE ISWCS*, pages 1–5, August 2013.

[31] G.T. Zhou and R. Raich. Spectral analysis of polynomial nonlinearity with applications to RF power amplifiers. *EURASIP Journal on Applied Signal Processing*, 12:1931–1840, 2004.

[32] H. Cramer. *Mathematical Methods of Statistics*. Princeton University Press, UK, 1946.

[33] R.A. Fisher and J.J. Wishart. The derivation of the pattern formulae of two-way partitions from those of simpler patterns. In *Proceedings of the London Mathematical Society*, 1932.

[34] F.F. Di Bruno. Sullo sviluppo delle funzioni. *Annali di Scienze Matematiche e Fisiche (in Italian)*, 6:479–780, 1855.

[35] S. Benedetto and E. Biglieri. *Principles of Digital Transmission with Wireless Applications*. Kluwer Academic/Plenum, New York, 1999.

[36] G.T. Zhou, H. Qian, L. Ding, and R. Raich. On baseband representation of a bandpass nonlinearity. *IEEE Transactions on Signal Processing*, 53(8):2953–2957, 2005.

[37] S. Josilo et al. Non-uniform FBMC - a pragmatic approach. In *IEEE ISWCS*, August 2013.

[38] ETSI TS 136 101 LTE. Evolved universal terrestrial radio access (E-UTRA); user equipment (UE) radio transmission and reception. *3GPP TS 36.101*, version 11.8.0(Release 11), 2010.

[39] K.L. Du and M.N. Swamy. *Wireless Communication Systems: From RF Subsystems to 4G Enabling Technologies*. Cambridge University Press, New York, 2010.

[40] H. Ochiai and H. Imai. On the distribution of the peak-to-average power ratio in OFDM signals. *IEEE Transactions on Communication*, 49(2):282 – 289, February 2001.

[41] J. Tellado. *Peak to Average Ratio Reduction for Multicarrier Modulation*. PhD Disertation, Stanford University, 1999.

[42] M.R. Schroeder. *Number Theory in Science and Communication*. Springer Series, Berlin, Germany, 1997.

[43] H. G. Ryu, B. I. Jin, and I. B. Jin. Papr reduction using soft clipping and ACI rejection in OFDM system. *IEEE Transactions on Consumer Electronics*, 48(1):17–22, August 2002.

[44] Y. Chen, J. Zhang, and A.D. Jayalath. Estimation and compensation of clipping noise in OFDMA systems. *IEEE Transactions on Wireless Communications*, 9(2):523–527, February 2010.

[45] J. Tellado. *Multicarrier Modulation with Low PAR: Applications to DSL and Wirelesss*. Kluwer Academic Publishers, Norwell, MA, US, 2000.

[46] L. Q. Wang and C. Tellambura. Analysis of clipping noise and tone reservation algorithms for peak reduction in OFDM systems. *IEEE Transactions on Vehicular Technology*, 57(3):1675–1680, May 2008.

[47] Z. X. Yang, H. D. Fang, and C. Y. Pan. ACE with frame interleaving scheme to reduce peak-to-average power ratio in OFDM systems. *IEEE Transactions on Broadcasting*, 51(4):571–575, March 2005.

[48] S. G. Kang, J. G. Kim, and E. K. Joo. A novel subblock partition scheme for partial transmit sequence OFDM. *IEEE Transactions on Broadcasting*, 45(3):333–338, September 1999.

[49] T.T. Nguyen and L. Lampe. On partial transmit sequences for PAR reduction in OFDM systems. *IEEE Transactions on Wireless Communications*, 7(2):746–755, February 2008.

[50] L. J. Ciminia and N. R. Sollenberger. Peak-to-average power ratio reduction of an OFDM signal using partial transmit sequence. *IEEE Communications Letters*, 4(3):86–88, March 2000.

[51] C. Wang and O. Yuan. Low-complexity selected mapping schemes for peak-to-average power ratio reduction in OFDM systems. *IEEE Transactions on Signal Processing*, 53(12):4652–466, November 2005.

[52] X. Huang, J.H. Lu, J.L. Zheng, K.B. Letaief, and J.Gu. Companding transform for reduction in peak-to-average power ratio of OFDM signals. *IEEE Transactions on Wireless Communications*, 3(6):2030–2039, November 2004.

[53] T. Jiang, W.D. Xiang, P.C. Richardson, D.M. Qu, and G.X. Zhu. On the nonlinear companding transform for reduction in PAPR of MCM signals. *IEEE Transactions on Wireless Communications*, 6(6):2017–2021, June 2007.

[54] T.A. Wilkinson and A.E. Jones. Minimisation of the peak-to-mean envelope power ratio of multicarrier transmission schemes by block coding. In *45th IEEE Vehicular Technology Conference*, pages 925–829, June 1995.

[55] H.S. Hee and L.J. Hong. An overview of peak-to-average power ratio reduction techniques for multicarrier transmission. *IEEE Transactions on Wireless Communications*, 12(2):56–65, April 2005.

[56] T. Jiang and Y. Wu. An overview: Peak-to-average power ratio of OFDM signals. *IEEE Transactions on Broadcasting*, 54(2):257–268, June 2008.

[57] R. OŃeil and L.B. Lopes. Envelope variations and spectral splatter in clipped multicarrier signals. In *IEEE PIMRC*, pages 71–75, September 1995.

[58] H. Ochiai and H. Imai. Performance analysis of deliberately clipped OFDM signals. *IEEE Transactions on Communication*, 50:89–101, January 2002.

[59] D. Kim and G.L. Stuber. Clipping noise mitigation for OFDM by decision-aided reconstruction. *IEEE Communication Letters*, 3:1–4, 2008.

[60] A. Gatherer and M. Polley. Controlling clipping probability in DMT transmission. *Asilomar Conference record*, 1:578–584, November 1997.

[61] M.H. Hayes. *Statistical Digital Signal Processing and Modeling*. John Wiley and Sons, New York, 1996.

[62] T. Tellado and J.M. Cioffi. Efficient algorithms for PAR redcution in multicarrier systems. In *IEEE Symposium on Information Theory*, pages 538–542, August 1998.

[63] B.S. Krongold and D.L. Jone. PAPR redcution in OFDM via active constellation extension. *IEEE Transactions on Broadcasting*, pages 258–268, September 2003.

[64] J.A. Davis and J. Jedwab. Peak-to-mean power control in OFDM, golay complementary sequences, and reed-muller codes. *IEEE Transactions on Information Theory*, 45(7):2397–2417, November 1999.

[65] Y. Louet and A. Le Glaunec. Peak-factor reduction in OFDM by reed-muller channel coding a new soft decision decoding algorithm. In *IEEE MELECON*, pages 872–875, May 2000.

[66] H. Lee and S.W. Golomb. A new construction of 64-QAM golay complementary sequences. *IEEE Transactions on Information Theory*, 52(4):1663–1670, April 2006.

[67] S.H. Muller and J.B. Huber. OFDM with reduced peak to average power ratio by optimum combination of partial transmit sequences. *IEE Electronics Letters*, 33(5):368–369, February 1997.

[68] S.H. Muller. A novel peak power reduction scheme for OFDM. In *IEEE PIMRC*, pages 1090–1094, September 1997.

[69] S. H. Muller. *OFDM for Wireless Communications: Nyquist Windowing, Peak-Power Reduction, and Synchronization*. Shaker Verlag, Germany, 2000.

[70] R.W. Bauml, R.F. Fischer, and J.B. Huber. Reducing the peak-to-average power ratio of multicarrier modulation by selected mapping. *IEE Electronics Letters*, 32(22):2056–2057, October 1996.

[71] P. Eevelt, M. Wade, and M. Tomlinson. Peak to average power reduction for OFDM schemes by selective scrambling. *IEE Electronics Letters*, 32(22):1963–1964, October 1996.

[72] D. Mesdagh and P. Spruyt. A method to reduce the probability of clipping in DMT-based transceivers. *IEEE Transactions on Communications*, 44:1234–1238, October 1996.

[73] R. J. Baxley and G. T. Zhou. Assessing peak-to-average power ratios for communications applications. In *IEEE MELECON*, pages 181–185, November 2004.

[74] Z. Kollar and P. Horvathr. Assessing peak-to-average power ratios for communications applications. *Journal of Computer Networks and Communications*, 2012, May 2012.

[75] S. Lu, D. Qu, and Y. He. Sliding window tone reservation technique for the peak-to-average power ratio reduction of FBMC-OQAM signals. *IEEE Transactions on Wireless Communications*, 1(4):267–271, August 2012.

[76] A. Skrzypczak, P. Siohan, and J. P. Javaudin. Reduction of the peak-to-average power ratio for OFDM-OQAM modulation. In *63rd IEEE Vehicular Technology Conference*, pages 2018–2022, May 2006.

[77] D. Qu, S. Lu, and T. Jiang. Multi-block joint optimization for the peak-to-average power ratio reduction of FBMC-OQAM signal. *IEEE Transactions on Signal Processing*, 61(7):1605–1613, April 2013.

[78] B. Le Floch, M. Alard, and C. Berrou. Coded orthogonal frequancy division multiplex. *Proceeding of the IEEE*, 83(6):982–996, June 1995.

[79] R.W. Chang. Synthesis of band-limited orthogonal signals for multichannel data transmissionl. *Bell System Technical Journal*, 45:1775–1796, December 1966.

[80] D. Le Ruyet H. Zhang and M. Terré. Spectral efficiency analysis in ofdm and OFDM/OQAM based cognitive radio networks. In *69th IEEE Vehicular Technology Conference*, April 2009.

[81] O. Abel Gouba. *Approche conjointe de la reduction du facteur de crete et de la linearisation dans le contexte* OFDM. PhD dissertation, Supelec, 2013.

[82] Bo. Ai, Z. Yang, C. Pan, T. Zhang, H. Yang, and Y. Wang. HPA pre-distortion based on an improved LUT technique. In *Wireless Conference 2006*, April 2006.

[83] R. Zayani. *Predistorsion adaptative des non-linearites* HPA *dans un systÃ¨me* OFDM *Ã lâaide des reseaux de neurones*. PhD dissertation, ENIT, 2008.

[84] G. Cybenko. Approximations by superpositions of sigmoidal functions. *Mathematics of Control, Signals, and Systems*, 2(4):303–314, 1989.

[85] K. Hornik. Approximation capabilities of multilayer feedforward networks. *Neural Networks*, 4(2):251 – 257, 1991.

[86] H. Abdulkader, F. Langlet, D. Roviras, and F. Castanie. Natural gradient algorithm for neural network applied to non-linear high power amplifiers. *International Journal on Adaptive Control and Signal Processing*, 16:557 – 576, 2002.

[87] R. Zayani, Y. Medjahdi, H. Bouhadda, H. Shaiek, D. Roviras, and R. Bouallegue. Adaptive predistortion techniques for non-linearly amplified FBMC-OQAM signals. In *IEEE VTC2014-Spring*, 2014.

[88] F. Wang et al. Design of wide-band envelope-tracking power amplifiers for OFDM applications. *IEEE Transactions On Microwave Theory and Techniques*, 53:1244–1255, April 2005.

Glossary and Definitions

Acronym	Meaning
$3GPP$	3^{rd} Generation Partnership Project
$4G$	4^{th} Generation
$5G$	5^{th} Generation
AM/AM	Amplitude Modulation/Amplitude Modulation
AM/PM	Amplitude Modulation/Phase Modulation
ACE	Active Constellation Extension
AFB	Analysis Filter Bank
AWGN	Additive White Gaussian Noise
BER	Bit Error Rate
BS	Base Station
CCDF	Complementary Cumulative Distribution Function
CP	Cyclic Prefix
DSLM	Dispersive SLM
DL	Down-Link
EB-SC	Filter Bank Single-Carrier
EER	Envelope Elimination and Restoration
EMPhAtiC	Enhanced Multicarrier techniques for Professional Ad-Hoc and cell-based Communications
ET	Envelope Tracking
FBMC/OQAM	Filter Bank Multi-Carrier based on OQAM
FC-FB	Fast-Convolution Filter Bank
FDMA	Frequency Division Multiple Access
FT	Fourier Transform
FFT	Fast Fourier Transform
FIR	Finite Impulse Response
FLO	Frequency-Limited Orthogonal
FMT	Filtered Multi-Tone
IBO	Input Back-Off
IOTA	Isotropic Orthogonal Transform Algorithm
HPA	High Power Amplifier
IFFT	Inverse Fast Fourier Transform
IOTA	Isotropic Orthogonal Transform Algorithm
LINC	Linear Amplification using Nonlinear Components
LM	Levenberg Marquardt
LTE	Long Term Evolution
LUT	Look Up Tables

Acronym	**Meaning**
MBJO	Multi-Block Joint Optimization
MGF	Moment Generating Function
MIMO	Multiple-Input Multiple-Output
MLP	Multi Layer Perceptron
NC	Non-Contiguous
NL	Nonlinear
NLD	Nonlinear Distortion
NN	Neural Networks
Nu	Non uniform
OBO	Output Back-Off
OFDM	Orthogonal Frequency Division Multiplexing
OQAM	Offset Quadrature Amplitude Modulation
OSLM	Overlapped SLM
PAPR	Peak-to-Average Power Ratio
pdf	probability density function
PHYDYAS	Physical Layer for DYnamic Spectrum access and cognitive radio
PM	Path Metric
PMR	Professional Mobile Radio
PSD	Power Spectral Density
PTS	Partial Transmit Sequences
QAM	Quadrature Amplitude Modulation
QPSK	Quadrature Phase-Shift Keying
RAT	Radio Access Technology
RB	Resource Block
RF	Radio frequency
SEL	Soft Envelope Limiter
(SER)	Symbol Error Rate
SNR	Signal-to-Noise Ratio
SSPA	Solid State Power Amplifiers
SC	Single-Carrier
SFB	Synthesis Filter Bank
SI	Side Information
SIR	Signal-to-Interference Ratio
SLM	Selected Mapping
SM	State Metric
SNR	Signal-to-Noise Ratio

Acronym	**Meaning**
TI	Tone Injection
TLO	Time-Limited Orthogonal
TSLM	Trellis-based SLM
TR	Tone Reservation
TWTA	Travelling Wave Tube Amplifiers
UE	User Equipment
UL	Up-Link